Title

Overcoming cisplatin resistance in head and neck squamous cell carcinoma: micro- and nanotechnology-based drug delivery as novel therapeutic strategies

Author

Li, Xiyao

Publication Date

2024

Peer reviewed|Thesis/dissertation

UNIVERSITY OF CALIFORNIA

Los Angeles

Overcoming cisplatin resistance in head and neck squamous cell carcinoma: micro- and nanotechnology-based drug delivery as novel therapeutic strategies

A dissertation submitted in partial satisfaction of the requirements

for the degree Doctor of Philosophy

in Bioengineering

by

Xiyao Li

2024

ABSTRACT OF THE DISSERTATION

Overcoming cisplatin resistance in head and neck squamous cell carcinoma:
micro- and nanotechnology-based drug delivery
as novel therapeutic strategies

by

Xiyao Li
Doctor of Philosophy in Bioengineering
University of California, Los Angeles, 2024
Professor Song Li, Chair

Head and neck squamous cell carcinoma (HNSCC) is the sixth most prevalent cancer worldwide. For most HNSCC patients with locally advanced disease, platinum-based drugs, especially cisplatin, remain the gold standard to reduce the risk of recurrence and improve survival rate. Drug resistance, however, is the main issue obstructing the optimum cisplatin therapeutic efficiency. In this dissertation research, two auxiliary systems were designed to overcome the cisplatin resistance in HNSCC. The first system loaded a small molecule drug with high therapeutic efficacy into polymer microparticles. Upon the intratumoral injection through microneedle, a local and sustained release was achieved, leading to suppressed proliferation, inhibited migration, and promoted apoptosis of cancer cells. The second system involves the design of a novel enzyme delivery system to target tumor microenvironment, which not only

reduces cancer cell viability, migration, and invasion, but also activates immune response. The strategies described in this dissertation research can be extended to other small molecule drugs or therapeutic proteins for cancer therapies beyond cisplatin-resistant HNSCC, providing a platform for more effective cancer therapy.

The dissertation of Xiyao Li is approved.

Cun Yu Wang

Yunfeng Lu

Alireza Moshaverinia

Jing Wen

Song Li, Committee Chair

University of California, Los Angeles

2024

Table of contents

List of Tables

List of Figures

Vita

2014-2018 B.A. in Biomedical Engineering, Shanghai Jiaotong University

2018-2019 M.Eng in Biomedical Engineering, Cornell University

2020-2021 M.S. in Bioengineering, University of California, Los Angeles

Publications

- Lin, L.; Liu, Z.; **Li, X.**; Gu, H.; Ye, J., Quantifying the reflective index of nanometer-thick molecular layers on nanoparticles. *Nanoscale* **9**, 2213-2218 (2019)
- Lin, L.; Zhang, Q.; **Li, X.**; Qiu, M.; Jiang, X.; Jin, W.; Gu, H.; Lei, D. Y.; Ye, J., Electron Transport Across Plasmonic Molecular Nanogaps Interrogated with Surface-Enhanced Raman Scattering, *ACS Nano* **12**, 6492-6503 (2018)
- Li, F.; **Li, X.**; Li, Z.; Ji, W.; Lu, S.; Xia, W., βKlotho is identified as a target for theranostics in non-small cell lung cancer, *Theranostics* **9**, 7474 (2019)
- Stowell, C.; **Li, X.**; Matsunaga, M.; Cockreham, C.; Kelly, K.; Cheetham, J.; Tzeng, E.; Wang. Y., Resorbable vascular grafts show rapid cellularization and degradation in the ovine carotid, *Journal of Tissue Engineering and Regenerative Medicine* **14**, 1673-1684 (2020)
- **Li, X.**; Tat, T.; Chen, J., Triboelectric nanogenerators for self-powered drug delivery. *Trends in Chemistry* **3**, 765-778 (2021)
- Xiao, X.; Xiao, X.; Nashalian, A.; Libanori, A.; Fang, Y.; **Li, X.**; Chen, J., Triboelectric nanogenerators for self‐powered wound healing, *Advanced Healthcare Materials* **10**, 2100975 (2021)

- Deng, P., Chang, I., Wang, J., Badreldin, A.A., **Li, X.**, Yu, B. and Wang, C.Y., Loss of KDM4B impairs osteogenic differentiation of OMSCs and promotes oral bone aging. *International Journal of Oral Science* **14**, 24 (2022)
- Liu, W., Cao, H., Wang, J., Elmusrati, A., Han, B., Chen, W., Zhou, P., **Li, X.**, Keysar, S., Jimeno, A. and Wang, C.Y., Histone-methyltransferase KMT2D deficiency impairs the Fanconi anemia/BRCA pathway upon glycolytic inhibition in squamous cell carcinoma. *Nature Communications* **15**, 6755 (2024)

Chapter 1: Head and neck squamous cell cancer overview.

1.1 Epidemiology and current treatment of HNSCC.

Cancer is a major public health problem worldwide and is the second leading cause of death in the United States[1]. Developed from the mucosal epithelium in the oral cavity, pharynx, and larynx, head and neck squamous cell carcinoma (HNSCC) is the most common malignancies that arise in the head and neck area[2,3]. HNSCC ranks the sixth most prevalent cancer globally, with estimated 890,000 new cases and 450,000 deaths reported each year[4,5]. In 2023, HNSCC had 54,540 new cases, and led to 11,580 deaths in the United States[1]. The incidence is expected to increase by 30%, potentially reaching 1.08 million new cases per year by 2030, according to data from the Global Cancer Observatory (GLOBOCAN)[4,5]. The burden of HNSCC varies across countries/regions, and it has generally been correlated with exposure to specific products containing carcinogens, excessive alcohol consumption, or human papillomavirus (HPV) - associated oropharyngeal infections[6–8].

With the recognition of high-risk HPV infection, particularly type 16, as a significant risk factor and important prognostic indicator for HNSCC, currently there is growing interest in categorizing HNSCC into two distinct types: HPV-positive and HPV-negative. Table 1-1 shows the distinct biology and molecular phenotype of HPV-positive HNSCCs when compared with HPV-negative HNSCCs[9–12]. Generally, HPV-negative HNSCC displays late diagnosis age, lower male-female patient ratio, higher dependence on smoking and alcohol, later diagnosis stage, and poorer prognosis. This differentiation of HPV-positive and HPV-negative HNSCC enhanced the understanding of the unique biology, mutational profiles, treatment response predictors, and

survival outcomes associated with each type, driving targeted research and treatment strategies for HPV-positive and HPV-negative HNSCC[13].

Variable	HPV-positive	HPV-negative
Age (y)	40-60	>60
M:F	8:1	3:1
Smoking/alcohol dependence	Never or minimal	Significant
Marijuana use	Strong association	Unknown
Early sexual experience	Strong association	Unknown
Multiple sexual partners	Strong association	Unknown
Tumor (T) stage	Early T stage	More advanced T stage
Distant metastasis		
DCR (%)	70-90	70-90
Second primary rate (%)	11	4.6
Overall response to treatment		
2-Year OS (%)	94 (95% CI, 87-100)	58 (95% CI, 49-74)
2-Year PFS (%)	85 (95% CI, 74-99)	53 (95% CI, 36-67)

Table 1-1. Comparison between HPV-positive and HPV-negative HNSCC. M: male; F: female; DCR: distant metastases control rate; OS: overall survival; PFS: progression-free survival; CI: confidence interval.

Over the past three decades, survival rates for HNSCC have seen modest improvement, with 5-year survival rates increasing from 55% (1992–1996) to 66% (2002–2006) across all age groups and tumor locations[14]. However, instead of the development of novel therapeutic methods, the improved outcomes are partially attributed to the rise of HPV-positive HNSCC, which typically

carries a more favorable prognosis than HPV-negative HNSCC. Increased survival rates are observed in HPV-positive cases but not in HPV-negative cases[15]. Beyond the direct mortality from HNSCC, the survivors experience significant psychological distress and a diminished quality of life, leading to a suicide rate of 63.4 per 100,000 individuals. This rate is second only to pancreatic cancer survivors (86.4 per 100,000) and markedly higher than the rate among survivors of other cancers (23.6 per 100,000)[16].

Although natural history is different for HPV-positive and HPV-negative HNSCC, it does not lead to absolute differences in how patients should be managed. The treatment approach to every individual patient is guided by anatomical subsite, stage, disease characteristics, functional considerations, and patient wishes. Surgery, radiation, and chemotherapy in various combinations are utilized as the major clinic management of HNSCC, depending on the TNM stage and primary site[3,17]. In approximately 40% of patients who had limited or early-stage disease (stage I and II), single modality intervention including surgery or radiation alone can achieve a cure rate of over 80%[18]. Surgery is commonly used for oral cavity cancers where clear margins can be achieved and function is preserved. Classic open surgery may result in cosmetic deformity and functional impairment and is less favored by patients. Advances in minimally invasive surgical techniques, such as transoral robotic surgery[19,20], laser resection[21], and larynx-preserving partial laryngectomy[22], along with enhanced reconstructive methods, have broadened the use of primary surgical treatment in managing head and neck cancers. Radiation Therapy is usually employed for the treatment of locally advanced diseases, and it's more commonly employed for pharyngeal and laryngeal cancers. The main side effect of radiation is long-term toxicity, leading to xerostomia, dysphagia, percutaneous endoscopic gastrostomy tube dependence, chronic aspiration, and hypothyroidism[23]. Recent advances have been made to overcome these disadvantages, including

substituting standard radiation therapy with a moderately hypofractionated radiation schedule[24,25], and intensity-modulated radiotherapy[26]. For most HNSCC patients with locally advanced disease (stage III and IVA/B), platinum-based chemoradiation remains the gold standard to reduce the risk of recurrence and improve survival rate[27,28].

1.2 Cisplatin resistance.

Platinum-based drugs are employed for the treatment of a wide array of solid tumors including HNSCC[29]. First described by Italian chemists as early as 1845, cis-diamminedichloroplatinum(II) (CDDP, best known as cisplatin) is one of the most well-known platinum-based compounds that exert clinical activity[30,31]. Although it was first approved by the Food and Drug Administration (FDA) only for the treatment of testicular and bladder cancer in 1978[32], during the past decades cisplatin has become the most used chemotherapeutic drug worldwide against a wide spectrum of solid tumors, including testicular, bladder, ovarian, colorectal, lung, and head and neck cancers[33,34]. For example, the current standard chemotherapy regimen of HNSCC is single-agent cisplatin given intravenously as short-term infusion in physiological saline at a dosage of 100 mg/m^2 every 3 weeks. However, the 3-year survival in a predominantly HPV-negative population is only 37%[35].

The main issue with obtaining the optimum cisplatin cancer treatment is the toxicity and resistance[36]. The cytotoxicity of cisplatin including mild-to-moderate nephrotoxic, neurotoxic, cardiotoxic, and ototoxic, affecting multiple organs not limited to kidneys, peripheral nerves, and hearts[37–40]. Cisplatin resistance constitutes the most prominent obstacle against the use of cisplatin. The resistance generally occurs in two main forms: intrinsic resistance, where tumor cells are inherently unresponsive to cisplatin before any treatment, and acquired resistance, where cells that were initially sensitive become resistant after drug exposure. Acquired resistance is now

understood as a complex, multifactorial process involving various host factors, genetic and epigenetic changes, and multiple molecular pathways[41,42]. Key mechanisms contributing to resistance include reduced drug accumulation, changes in intracellular drug distribution, weakened drug-target interactions, enhanced detoxification processes, disruptions in cell-cycle regulation, more effective DNA repair of drug-induced damage, and diminished apoptosis[43].

Numerous studies have investigated second-generation platinum compounds with the specific aim of reducing the side effects of cisplatin while retaining its anticancer properties. Cis-diammine (cyclobutane-1,1-dicarboxylate-O, O') platinum (II) (carboplatin) was developed in 1985 and approved by FDA in 1989 for treating ovarian cancer. This compound reduces nephrotoxicity and neurotoxicity, but forms the same DNA adducts as cisplatin[44]. This realization spurred further drug development, culminating in the 2002 introduction of oxaliplatin (1R,2R)-cyclohexane-1,2-diamine platinum(II)), which offers distinct pharmacological benefits, especially for treating colorectal cancer and lung cancer[45,46]. Recently, other platinum-based drugs, such as picoplatin (ammine dichloro (2-methylpyridine) platinum) and satraplatin (OC-6-43-bis (acetato) ammine dichloro (cyclohexylamine) platinum), have been investigated in clinical trials. However, neither drug has demonstrated substantial advantages over established agents like cisplatin, carboplatin, or oxaliplatin[47,48]. In fact, carboplatin and oxaliplatin also have lower therapeutic potential compared with cisplatin. In certain clinical situations, cisplatin remains the leading, and often the only, viable treatment option for specific cancers[49].

What's worse, since carboplatin shares the active form with cisplatin, many tumors resistant to cisplatin also show resistance to carboplatin. Although oxaliplatin is generally effective against cancers resistant to cisplatin, some studies indicate partial cross-resistance of oxaliplatin

and cisplatin[50]. Thus, the high incidence of chemoresistance, especially against cisplatin, remains the main limitation to the clinical usefulness of cisplatin as an anticancer drug.

Chapter 2: Enhancing head and neck squamous cell cancer treatment through microneedle-based drug delivery system.

2.1 Introduction.

2.1.1 BET inhibitor for cancer treatment.

Cancer originates from gene mutations and involves abnormal epigenetic regulation of chromatin. Chromatin consists of DNA, nucleosomes, and transcription factors and can be either active or inactive depending on epigenetic changes to histone proteins. Acetylation of histone tails is one of those changes. The extra negative charges formed during the acetylation process can decrease the interaction between the positively charged histone N-termini with the negatively charged phosphate groups of DNA, thus relaxing chromatin structure and making it accessible for transcription. Meanwhile, the regulation of gene expression also relies on chromatin decoding. Both the encoding and decoding of chromatin are accomplished through the action of so-called chromatin “readers”, “writers”, and “erasers”, and cancer can occur through abnormalities of any one or more of these factors[51]. Histone acetyltransferases (HATs) work as chromatin writers to add acetyl groups, while histone deacetylases (HDACs) remove them as chromatin erasers. Bromodomains recognize and read the acetyl-histone marks in active chromatin. They are present within a large number of proteins, including HATs.

Bromodomain and extraterminal domain (BET) proteins are characterized by the presence of two tandem bromodomains (BD1 and BD2), an extraterminal domain (ET), and a C-terminal domain (CTD)[52]. BET family proteins include BRD2, BRD3, BRD4, and the testis-restricted

BRDT. They mainly recognize acetylated lysine of histone 4[52,53]. Through a bromodomain-independent manner, BET proteins also recognize acetylated nonhistone proteins, including different transcription factors[54]. BET proteins also have kinase activity, a function not yet fully understood[55].

Evidence coming from preclinical studies indicates the role of BET proteins in human cancer and has provided the rationale for targeting BET proteins as a strategy for the development of new anticancer drugs[56]. The first description to achieve antitumor activity by inhibiting the binding between acetylated histone and bromodomain-containing proteins was done by Yoshitomi Pharmaceuticals (patent PCT/JP2008/073864). Many following publications described novel BET inhibitors, demonstrating that pharmacologic BET inhibition has clear preclinical antitumor activity in a variety of solid tumors, including HNSCC[57,58]. Several compounds have also entered clinical development in phase I or II studies for patients with solid tumors and hematologic malignancies **(Table 2-1)**.

Drug (administration)	Phase	Tumor type
GSK525762 (oral)	I	Solid tumors, NUT carcinoma, hematologic malignancies
OTX015/MK-8628 (oral)	I	Solid tumors, glioblastoma, hematologic malignancies
CPI-0610 (oral)	I	Non-Hodgkin lymphomas, multiple myeloma
RO6870810/TEN-010 (subcutaneous injection)	I	Solid tumors,myelodysplastic syndrome, leukemia, lymphomas
BAY1238097 (oral)	I	Solid tumors, non-Hodgkin lymphomas
GS-5829 (oral)	I/II	Solid tumors, lymphomas
ABBV-075 (oral)	I	Solid tumors
INCB054329 (oral)	I/II	Solid tumors, non-Hodgkin lymphomas, acute leukemia, chronic myeloid leukemia, multiple myeloma
BMS-986158 (oral)	I/II	Solid tumors
BI 894999 (oral)	I	Solid tumors, non-Hodgkin lymphomas
PLX51107 (oral)	I	Solid tumors, hematologic malignancies
GSK2820151 (oral)	I	Solid tumors
ZEN-3694 (oral)	I	Prostate cancer
INCB057643 (oral)	I/II	Solid tumors, hematologic malignancies
ODM-207 (oral)	I/II	Solid tumors

Table 2-1. BET inhibitors in clinical trials. Data from ClinicalTrials.gov.

QCA570 was recently reported as an extremely potent and highly efficacious BET degrader[59]. The design of QCA570 was based on the proteolysis targeting chimera (PROTAC) concept proposed in 2001[60]. Like other PROTAC degrader molecules, QCA570 contains a ligand for the target BET proteins, a second ligand capable of binding to and recruiting an E3 ligase complex to degrade the target protein, and a linker between the two ligands. Capable of degrading BET proteins at low picomolar (pM) concentrations, QCA570 is the most efficacious BET degrader reported to date[59]. Although its antitumor activity has been proved with several types of

cancers, including leukemia, non-small cell lung cancer, and bladder cancer[59,61,62], QCA570 has not been studied in HNSCC.

2.1.2 Microneedles as a drug delivery system for cancer treatment.

Although advances have been made in the prevention, early detection, and effective treatments, cancer remains one of the most frighting and traumatizing diseases and the leading cause of death worldwide, accounting for approximately 18 million cases and causing 10 million deaths every year[63]. With most research studies on cancer emphasizing the biology of cancer and drug discoveries, novel drug delivery methods emerged to be a potential route to increase the treatment efficacy of existing drugs and improve patients' quality of life.

Currently, cancer drugs are mostly delivered orally or via the parenteral route. Nevertheless, at advanced cancer stages, these routes may not be a feasible way to administer the drugs due to patients' condition. They may also lead to unnecessary adverse effects due to the systematic delivery of drugs. As a result, great attention has been paid to the development of personalized and precision-based methods for drug delivery[64–66].

After the first proposal in 1976, scientists began decades of research on microneedles to improve the efficiency of drug delivery in a painless manner[67,68]. Microneedle technology utilizes a patch embedded with tiny, micron-sized needles capable of delivering vaccines, drug molecules, proteins, genes, antibodies, microparticles, and nanoparticles[69]. This technology enables self-administration, allowing patients to painlessly deliver drugs, and it is widely used in minimally invasive biochemical detection methods, vaccination, and cancer treatment[70,71]. Microneedles also offer a more precise and personalized treatment option for cancer patients, as they can be applied directly or near the tumor site with enhanced drug delivery accuracy. Compared to traditional methods like hypodermic injections or oral drug delivery, microneedles provide a more

comfortable, convenient, and acceptable option to patients with superior targeting and efficiency in delivering treatments to tumor cells[72].

Based on the different mechanisms of action after application, microneedles can be categorized into five main types: solid, hollow, coated, dissolving, and hydrogel-forming[73]. Solid microneedles are mostly used in a two-step "poke and patch" method for drug delivery. First, a microneedle array is applied to create microscopic pores as the conduit channels in the skin, and then a drug formulation in various forms, (e.g., cream, gel, solution, or patch) is applied after the microneedles are removed[72]. Hollow microneedles feature an empty core and a pore at the tip, allowing drugs to be delivered or fluids to be extracted in a "poke and flow" process. Coated microneedles follow a "coat and poke" method. The drug is loaded in the coating on microneedles and can be released quickly as the coating dissolves. Newly developed dissolving and hydrogel-based microneedles are made from polymers. Dissolving microneedles release drugs as they dissolve, while hydrogel microneedles swell upon insertion, enabling drug delivery[71]. The differences in types and mechanisms of action also cause a variety of advantages and limitations, and thus they could serve different functions in cancer therapy **(Table 2-2)**[74].

Types	Advantages	Limitations
Solid	•Mechanical strength •Physical stability •Reasonable drug loading	•Poor dose accuracy •Requirements of rapid healing •Potential for infections due to reuse •Poor biocompatibility
Hollow	•Dose accuracy •Reasonable drug loading •Constant flow rate	•Clogging •Requirement of prefilled syringe •Poor mechanical strength •Potential for infection due to reuse •Poor biocompatibility
Coated	•Mechanical strength	•Peeling during insertion •Poor biocompatibility •Dose limitation •Formulation migration during manufacturing and storage
Dissolving	•Low cost manufacturing •Ease of manufacturing •Controlled drug release profile •One-step application	•Poor mechanical strength •Dose limitation
Hydrogel forming	•No residual excipients in the skin after removal •Easy to manufacture •Controlled drug release profile	•Poor mechanical strength and physical stability •Dose limitation

Table 2-2. Advantages and limitations of different types of microneedles (solid, hollow, coated, dissolving, and hydrogel-forming) for use in cancer therapy.

2.1.3 Microneedles for HNSCC treatment.

Surgery, radiation, and chemotherapy remain to be the primary treatments for HNSCC[75]. Early-stage cancer is mainly treated with surgery, while advanced or inoperable cases are typically managed with radiation therapy and chemotherapy. These therapies are often combined to slow cancer progression, where radiation and chemotherapy are frequently used as adjuvant treatments to support surgical intervention[76]. However, those three treatments all have their limitations. Surgical resection can result in permanent damage to patients by causing significant aesthetic

concerns and affecting basic oral functions like chewing, swallowing, and speaking[77]. Despite the effectiveness of radiotherapy and chemotherapy, they also lead to side effects such as nausea, vomiting, diarrhea, and skin reactions, which severely impact patients' quality of life[78]. Moreover, the prognosis for most oral cancer patients remains poor, and the disease continues to threaten countless lives.

Therefore, various new treatments for HNSCC have emerged based on precise drug delivery, which is the key strategy to minimize side effects[79]. Traditionally, drugs are administered through various routes, including oral, topical, parenteral, rectal, inhalation, and ophthalmic, depending on the target site and type of disease[80]. However, those conventional drug delivery methods have multiple limitations when it comes to HNSCC. For example, oral administration, though simple and convenient, often results in reduced drug bioavailability due to poor drug solubility, stability, and absorption in the gastrointestinal tract. Those systematical delivery methods increase side effects and limit local anticancer efficacy, because they will damage healthy tissues as well[81]. As a result, maximizing drug concentration in tumor cells while minimizing it in normal tissues is essential for improving treatment effciency[82]. Transdermal administration via the skin and mucous membranes offers better bioavailability and more consistent pharmacokinetics, making it a better option for localized tumor treatment. And microneedles, as a type of transdermal patch, appear to be one of the most promising novel treatments for HNSCC. Their ability to penetrate the mucosal membranes of the oral cavity and deliver drugs efficiently has been proved in several research studies on HNSCC[83–85].

Considering these advances in HNSCC treatment, we developed a dissolvable microneedle patch, providing potential novel and painless options for HNSCC treatment, even including cisplatin-resistant cases. Briefly, therapeutic agent QCA570 was loaded into microparticles, and

then locally delivered to tumor sites by microneedles. The microneedle patches presented sustained release of QCA570 and significantly inhibited HNSCC progression both in vitro and in vivo. To our knowledge, this study is the first to utilize microneedles to deliver small-molecule drugs for HNSCC treatment.

2.2 Materials and methods.

2.2.1 Materials.

All chemicals were purchased from Sigma-Aldrich (St. Louis, MO) unless otherwise noted and were used as received.

2.2.2 Instruments.

Images of cells, microneedles, and tissue sections with immunohistochemistry staining were obtained with an IX73 inverted microscope (Olympus Life Science). The flow cytometry analysis was performed on Attune NxT flow cytometer (Thermo Fisher Scientific). Microparticles were synthesized using the homogenizer PowerGen 500 (Thermo Fisher Scientific). A low-force mechanical testing system (5943 MicroTester, Instron) was used to test the mechanical strength. UV/vis absorbance was measured by NanoDrop One spectrophotometer (Thermo Fisher Scientific). The absorbance was measured with an iMark Microplate Absorbance Reader (Bio-Rad Laboratories). Cell numbers were acquired by manual counting with trypan blue dye exclusion under the microscope.

2.2.3 Cell culture.

Human HNSCC cell lines SCC1 and SCC23 were from the University of Michigan and were maintained in DMEM containing 10% FBS and 1% penicillin-streptomycin. The mouse MOC1 cell line was kindly provided by Dr. Gutkind at The University of California, San Diego,

and maintained in DMEM containing 10% FBS and 1% penicillin-streptomycin. The cisplatin-resistant MOC1R, SCC1R, and SCC23R cells were established by chronic culture in the gradually increased concentration of cisplatin, presenting a much higher tolerance to high concentration cisplatin treatment **(Fig. 2-1)**. For example, SCC1R has a cisplatin IC_{50} of 81.10 μM, while the cisplatin IC_{50} of the original SCC1 is only 6.60 μM. SCC23R has a cisplatin IC_{50} of 76.30 μM, compared with the 5.998 μM cisplatin IC_{50} of the original SCC23. MOC1R, SCC1R, and SCC23R cells were maintained in the same medium with the addition of 5 μg/ml cisplatin[58,86]. All these cells were maintained at 37 °C in 5% CO2 atmosphere.

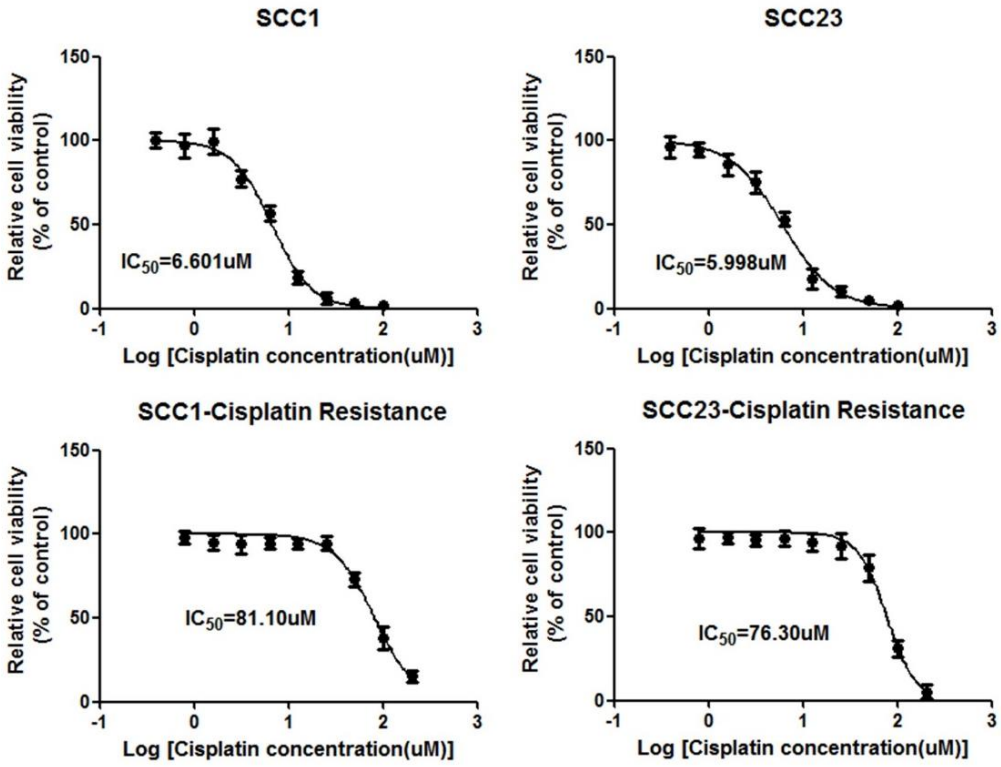

Fig. 2-1. Cell viability after cisplatin treatment with different concentrations.

2.2.4 Western blot analysis.

Cells were lysed, collected, and extracted using whole cell lysis buffer with 1:100 volume of protease inhibitor cocktail on ice. The protein concentration was measured colorimetrically using Bio-Rad reagents. For each sample, 20 μg of total proteins were resolved, separated on 10% SDS-PAGE, and then transferred onto a polyvinylidene difluoride (PVDF) membrane using a Bio-Rad semidry transfer system. After the transfer, membranes were blocked with 5% dry-milk in TBS/Tween20 (TBST) buffer at room temperature (RT) for 1 hour and incubated with primary antibodies diluted in TBST buffer with 5% dry-milk at 4 °C overnight. After washing three times with TBST, secondary antibodies diluted in TBST with 5% dry-milk were introduced for 2 h at RT (Anti-rabbit-HRP: 1:7500 or Anti-mouse-HRP: 1:5000, Promega) and detected using enhanced chemiluminescence (ECL) reagents (Pierce) and ChemiDoc MP system (Bio-Rad Laboratories). Primary antibodies used in this study are BRD2 (Abcam, ab243865), BRD3 (Bethyl Laboratories, A302-468A), BRD4 (Abcam, ab128874), c-Myc (Cell Signaling Technology, 5650), and α-tubulin (Sigma-Aldrich, T5168).

2.2.5 Cell proliferation.

The Cell Counting Kit-8 (CCK8) assay (ApexBio, K1018) was used to assess cell viability and proliferation following the product manual. Briefly, cells were seeded in 96-well plates at an appropriate density (2000 cells/well for MOC1 and MOC1R, 3000 cells/well for SCC1, SCC1R, SCC23, and SCC23R) and allowed to adhere overnight. The following day, various QCA570 concentrations were applied to the cells. CCK8 reagent was diluted 10 times with complete culture media. 100 μL diluted CCK-8 reagent was added to each well after the designated incubation period. The plate is returned to the incubator for an additional 2 hours, allowing the water-soluble tetrazolium salt (WST-8) to be reduced by dehydrogenases in metabolically active cells and

produce a water-soluble formazan dye. After incubation, the absorbance of each well is measured at 450 nm using a microplate reader. Since the amount of formazan produced is directly proportional to the number of viable cells, higher absorbance values indicate higher cell viability. The results were then analyzed to determine the effects of treatments on cell proliferation.

2.2.6 Cell invasion.

The transwell assay was used to assess cell invasion. BioCoat Matrigel® Invasion Chambers (Corning, 354480) were used following the product manual. Those chambers were pre-coated with an extracellular matrix (ECM) mimic layer consisting of Corning Matrigel® matrix, fibronectin, collagen, and laminin. Briefly, cells are first treated with different concentrations of QCA570 for 6 hours. Then 1×10^5 cells in the culture medium without serum were placed in the upper chamber of each transwell insert. The lower chamber contains 15% serum to stimulate cell movement. After incubation, cells that have invaded through the membrane are fixed with 70% ethanol for 30 minutes, stained with 2% crystal violet for 15 minutes, washed with DI water 3 times, dried overnight, and counted under the optical microscope.

2.2.7 Cell apoptosis.

The Annexin V/PI assay (BD Pharmingen, 556547) was used to detect apoptotic cells following the user manual. Briefly, cells treated with varying concentrations of QCA570 for 24 hours or 48 hours were harvested and washed with PBS. They were then resuspended in 1× binding buffer at a concentration of 1×10^6 cells/mL. Next, 100 µL of cell suspension was mixed with 5 µL of Annexin V-FITC and 5 µL of Propidium Iodide (PI) and incubated for 15 minutes in the dark. After incubation, 400 µL of binding buffer was added, and the cells were analyzed by flow

cytometry. Data was analyzed using FlowJo Software (10.10.0). Annexin V stained early apoptotic cells, while PI stained late apoptotic cells.

2.2.8 RNA isolation and RNA-seq.

RNA sequencing (RNA-seq) is a powerful technique to provide a comprehensive snapshot of RNA expression levels by converting RNA into complementary DNA (cDNA), followed by high-throughput sequencing. RNA-seq enables the identification of gene expression changes, splicing variants, novel transcripts, and non-coding RNAs. It is widely used in biological research, disease studies, and drug development to better understand gene regulation and cellular functions.[87]

SCC1 and SCC1R cells were treated with 10 μM QCA570 for 6 hours. Total RNA was extracted using TRIzol reagents. cDNA was generated using the reverse transcription reaction with 1 μg RNA per sample, Random Hexamers, dNTP mix, and M-MuLV Reverse Transcriptase. RNA quality control, library construction, and sequencing were all performed by the Technology Center for Genomics & Bioinformatics (TCGB) core at UCLA, and libraries were sequenced on Illumina HiSeq 3000. Analysis of RNA-seq data was done as described before.[88,89] Briefly, RNA-seq FASTQ sequences were mapped to the human genome hg38 (GRCh38) by Hisat2 (v2.2.0). For the uniquely mapped reads, FeatureCounts from Subread2 (v2.0.3) were utilized to count the reads mapped to each gene. The differentially expressed genes (DEGs) were identified by Deseq2 (v1.32.0). Gene ontology (GO) term and gene set enrichment analysis (GSEA) were used to find enriched functional annotations for differentially expressed genes. GO term analysis was carried out for gene transcripts both upregulated and downregulated by at least 1.5-fold using an online database for annotation, visualization and integrated named Discovery (DAVID) version 6.8.

GSEA was performed by using the annotated gene sets in the molecular signatures database version 7.1.

2.2.9 Synthesis and characterization of PLGA microparticles.

Acid-terminated PLGA (200 mg; 50:50 lactic acid-to-glycolic acid ratio) was dissolved and stirred in 5 mL dichloromethane (DCM) overnight for complete dissolution. QCA570 was dissolved in DMSO with the desired concentration. QCA570 solution was then added to PLGA solution at a volume ratio of 1:9, followed by 9-fold of the total volume of 1% polyvinyl alcohol (PVA) added right before homogenization at different speeds for 10 minutes. The homogenized solution was poured into 10-fold volume mL of 0.1% PVA and stirred for 4 hours in open air to evaporate organic solvents. Low-speed centrifugation (3000 rpm, 5 minutes) was performed twice to wash and precipitate the microparticles. PLGA microparticles were resuspended in Millipore water and stored in a refrigerator at 4°C before use.

2.2.10 Fabrication of microneedles.

To fabricate microneedles, PLGA microparticles were resuspended in 20% polyvinylpyrrolidone (PVP) solution and cast on negative microneedle molds (Micropoint Technologies). After centrifuging at 3000 rpm for 5 minutes to concentrate microparticles to needle tips, the microneedle patches were dried at room temperature for 24 hours. Then the solidified microneedle patches were peeled off from the molds and stored at 4°C until use.

2.2.11 Mechanical properties of microneedles.

The mechanical strength of the microneedles was assessed by a compression test using a low-force mechanical testing system. The microneedles were placed on a stainless-steel plate with their tips perpendicularly to the plate, and pressed by another stainless-steel plate moving at a

constant speed of 0.1 mm/minute. The relationship between the applied force and the deformation of the microneedles was recorded throughout the test until the microneedle tips were broken. Each test was conducted in triplicate to ensure consistency of results.

2.2.12 QCA570 release study.

In vitro release of QCA570 was studied by incubating a single patch in 20 mL PBS (pH 7.4; supplemented with 10 mM $CaCl_2$) at 37°C under constant gentle stirring. At different time intervals, stirring was stopped and 1 μL of the supernatant was taken from the sample. The concentration of released QCA570 was determined by measuring the absorbance at wavelength 270 nm using a UV-vis spectrophotometer.

2.2.13 Animal model setup and progression monitoring in vivo.

Animal research described in the study was approved by the University of California, Los Angeles' Chancellor's Animal Research Committee (Institutional Animal Care and Use Committee) and was conducted in accordance with guidelines for the housing and care of laboratory animals of the National Institutes of Health and Association for Assessment and Association for Assessment and Accreditation of Laboratory Animal Care International. Female NU/J and NSG mice were purchased from the Jackson Laboratory.

For the subcutaneous mouse model, SCC1R cells (2×10^6 cells/mouse) were resuspended in sterilized PBS and mixed with Matrigel at a volume ratio of 1:1. The mixture was injected subcutaneously into the flank of 6-week-old NU/J mice. One week after the injection, three doses of cisplatin in saline were intraperitoneally injected into mice every two days at a dosage of 1 mg/kg mouse body weight. The tumor growth was monitored every day and allowed to grow for another 2–3 weeks. After the average tumor size reached 150 mm^3, mice were randomly divided

into two groups and given 1) vehicle control, and 2) microneedle patches with 4 mg/kg QCA570 loaded PLGA microparticles. The body weight of mice and the tumor size were monitored twice a week. After the largest tumor dimension reached 1.5 cm, mice were sacrificed. Tumors were measured, weighed, and collected for histology analysis.

For the PDX model, human HNSCC primary tissues were obtained from Ronald Reagan UCLA Medical Center and the use of anonymized human remnant HNSCC samples for this study from the UCLA Translational Pathological Core Laboratory (TPCL) was approved by the UCLA Institutional Review Board (IRB #11-002504). Patients signed the informed consent under this IRB approval. The human HNSCC primary tissues were chopped into small fragments and subcutaneously transplanted into the flank area of 6-week-old female NSG mice using a 13 g cancer implant needle to generate the PDXs of HNSCC as described previously[58,86]. Mice were randomly divided into two groups and given the 1) vehicle control, and 2) microneedle patches with 4 mg/kg QCA570 loaded PLGA microparticles. Treatments started when the average tumor size reached 150 mm^3. The body weight of mice and the tumor size were monitored twice a week. After the largest tumor dimension reached 1.5 cm, mice were sacrificed. Tumors were measured, weighed, and collected for histology analysis. The equation used in this study to calculate the tumor size is as follows:

$$Tumor\ size = \frac{1}{2} \times length \times width \times width$$

2.2.14 Immunohistology staining (IHC).

HNSCC tumors were fixed with 4% paraformaldehyde overnight, then equilibrated in 70% ethanol as preparation. Paraffin-embedded sections were processed by the UCLA Translational Pathological Core. Then sections were deparaffinized with xylene and then rehydrated with

distilled water through an ethanol series of 100%, 90%, 70%, 50%, and 30%. After antigens retrieval (Agilent Dako, S1699) and endogenous peroxidase and alkaline phosphatase blocking (LSBio, LS-J1031), the slides were stained with polyclonal anti-BRD2 antibodies (1:500; Abcam, ab139690) or anti-Ki67 antibodies (1:100, Abcam, ab15580) at 4 °C overnight, respectively. After washing, the sections were incubated with secondary antibodies (Agilent Dako, K4001/K4003), and the signals were detected with liquid DAB+ substrate chromogen system (Agilent Dako, K3468), then counterstained with hematoxylin and mounted with aqueous permanent mounting medium (Agilent Dako, S196430-2). The intensity of immunohistology staining was scored as follows: 0, no staining; 1, weak staining; 2, moderate staining; 3, strong staining. The final IHC score was calculated using the following equation:

$$IHC\ Score = percentage\ of\ unstained\ cells\ \times 0 + percentage\ of\ weak\ stained\ cells\ \times 1 + percentage\ of\ moderate\ stained\ cells\ \times 2 + percentage\ of\ strong\ stained\ cells\ \times 3$$

2.2.15 Statistics.

Data are presented as means ± S.D. unless otherwise indicated. Statistical significance was calculated using GraphPad Prism. All the comparisons of significance between groups were calculated by two-tailed unpaired t-test.

2.3 Results.

2.3.1 QCA570 suppressed cell proliferation and invasion.

A murine HNSCC cell line MOC1 was used to validate the therapeutic efficacy of QCA570. MOC1 cells were seeded and treated with different QCA570 concentrations from 0.1 nM to 100

nM. It was found that QCA570 could significantly suppress MOC1 cell proliferation even at the low QCA570 concentration of 0.1nM (**Fig. 2-2 a)**. As the QCA570 concentration increased, the suppress efficacy also increased. With a QCA570 concentration of 1nM, cell growth was reduced to 50%. When the QCA570 concentration reached 100 nM, MOC1 cell growth was completely inhibited.

We further addressed the therapeutic efficacy of QCA570 on cisplatin-resistant cells using murine cell line MOC1R, which was selected from MOC1 cells by chronic culture in the gradually increased concentration of cisplatin. Like the results of MOC1, QCA570 could limit MOC1R cell growth at low concentrations **(Fig. 2-2 b)**. Meanwhile, QCA570 reduced MOC1R cell invasion **(Fig. 2-2 c)**. With a low QCA570 concentration of 0.1 nM, MOC1R cell invasion was significantly suppressed after 4-hour treatment. As QCA570 concentration increased, fewer MOC1R cells could migrate through Matrigel, an extracellular matrix (ECM) mimic. And a QCA570 concentration of 100 nm could completely inhibit MOC1R cell invasion **(Fig. 2-2 d)**.

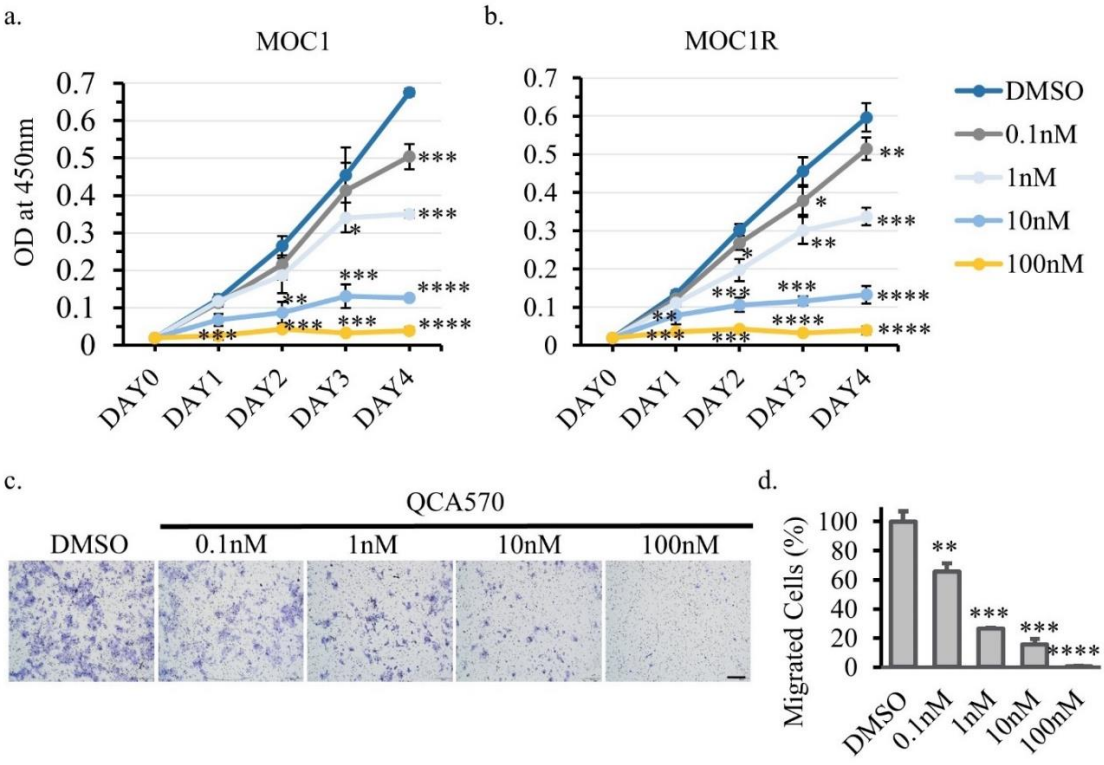

Fig. 2-2. QCA570 inhibited MOC1 and MOC1R cell growth and invasion. a-b, OD values at 450 nm reflecting MOC1 (a) and MOC1R (b) cell numbers under treatment with varying QCA570 concentrations at different time points. **c**, optical microscope images for MOC1R cell invasion with different QCA570 concentrations. Scale bar: 100μm. **d**, Statistic analysis of MOC1R cell invasion. * $p<0.1$, ** $p<0.05$, *** $p<0.01$, **** $p<0.001$.

The therapeutic efficacy of QCA570 was further assessed using human HNSCC cell line SCC1 and cisplatin-resistant SCC1R. Cells were seeded and treated with QCA570 at concentrations ranging from 0.1 nM to 100 nM. QCA570 significantly suppressed SCC1 **(Fig. 2-3 a)** and **SCC1R (Fig. 2-3 b)** cell proliferation, even at the low concentration of 0.1 nM. As the concentration increased, the inhibitory effect became more pronounced. At 1 nM, cell growth was reduced by 50%. 10 nM and 100 nM had similar effects, where cell growth was completely

inhibited. QCA570 was also effective in reducing SCC1R cell invasion **(Fig. 2-3 c)**. At a low concentration of 0.1 nM, it significantly suppressed SCC1R invasion after 4 hours of treatment. As the concentration increased, fewer SCC1R cells were able to migrate through the Matrigel. Complete inhibition of SCC1R cell invasion was achieved at 100 nM QCA570.

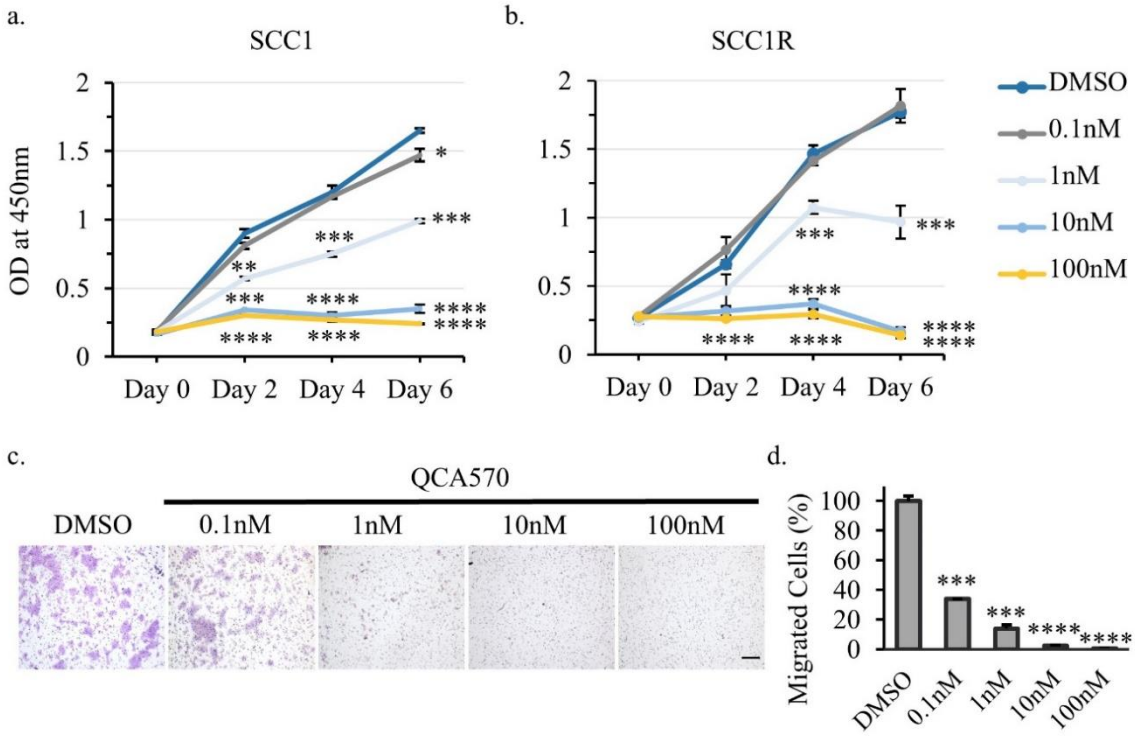

Fig. 2-3. QCA570 inhibited SCC1 and SCC1R cell growth and invasion. a-b, OD values at 450nm reflecting SCC1 (a) and SCC1R (b) cell numbers under treatment with varying QCA570 concentrations at different time points. **c**, optical microscope images for SCC1R cell invasion with different QCA570 concentrations. Scale bar: 100μm. **d**, statistical analysis of SCC1R cell invasion. * $p<0.1$, ** $p<0.05$, *** $p<0.01$, **** $p<0.001$.

Another human HNSCC cell line SCC23 and cisplatin-resistant SCC23R were also used to evaluate the therapeutic efficacy of QCA570. Cells were treated with varying concentrations of QCA570, ranging from 0.1 nM to 100 nM. QCA570 showed a significant inhibitory effect on both

SCC23 **(Fig. 2-4 a)** and SCC23R **(Fig. 2-4 b)** cell proliferation, even at a low concentration of 0.1 nM. When QCA570 concentration was higher than 10 nM, the SCC23 and SCC23R cells were fewer than seeded, indicating that QCA570 resulted in cell death after 4-day treatment.

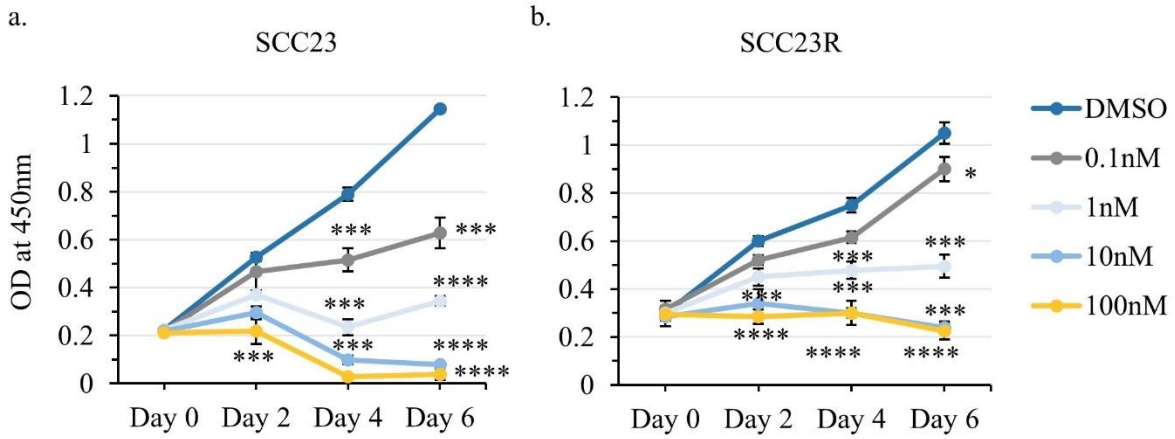

Fig. 2-4. QCA570 inhibited SCC23 and SCC23R cell growth and invasion. a-b, OD values at 450nm reflecting SCC23 (a) and SCC23R (b) cell numbers under treatment with varying QCA570 concentrations at different time points. * $p<0.1$, ** $p<0.05$, *** $p<0.01$, **** $p<0.001$.

2.3.2 QCA570 induced HNSCC cell apoptosis.

QCA570 has been shown to effectively induce apoptosis in cancer cells. Flow cytometry analysis of annexin V/PI-stained MOC1 cells confirmed that QCA570 treatment increased the percentage of apoptotic cells in a dose-dependent manner **(Fig. 2-5 a)**. At low concentrations (0.1 nM), QCA570 initiated early apoptosis in MOC1 cells, and as the concentration increased, a greater proportion of cells underwent apoptosis. Higher concentrations (up to 100 nM) resulted in more than 50% apoptosis of the cell population **(Fig. 2-5 b)**. Similarly, in MOC1R cells, which are typically resistant to conventional therapies, QCA570 induced significant levels of apoptosis, overcoming the resistance mechanisms that often limit treatment efficacy **(Fig. 2-6)**.

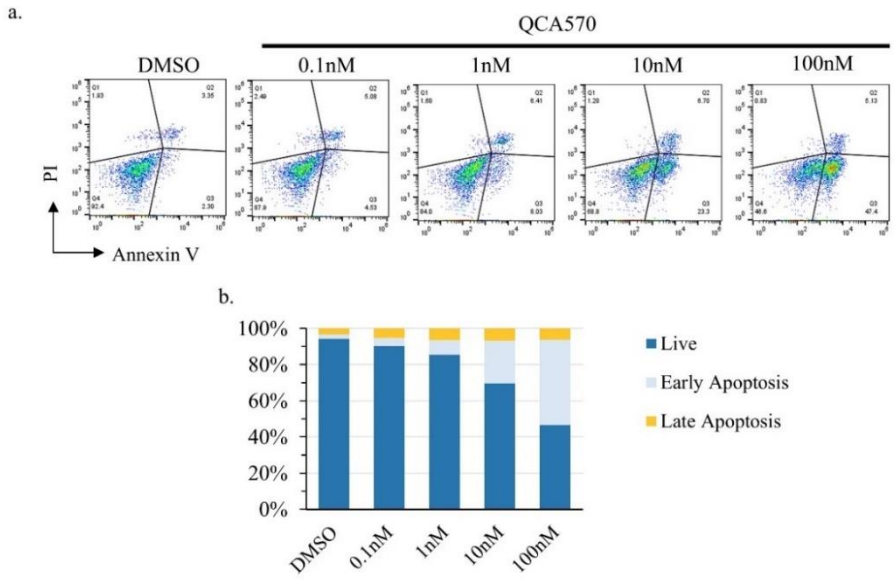

Fig. 2-5. QCA570 induced MOC1 cell apoptosis. a, gating method to separate live cells (Q4), early apoptotic cells (Q3), and late apoptotic cells (Q4). **b,** statistical analysis of cells under different conditions after 48-hour QCA570 treatment.

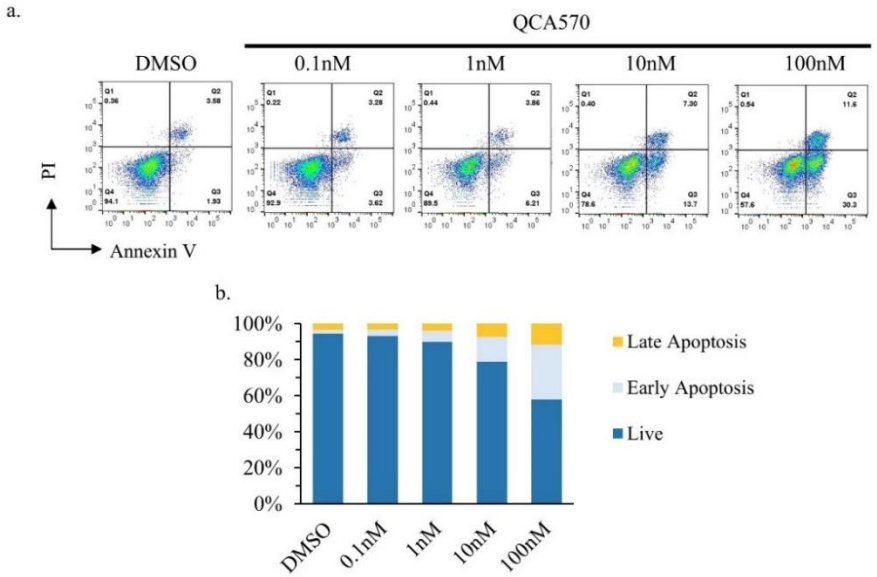

Fig. 2-6. QCA570 induced MOC1R cell apoptosis. a, gating method to separate live cells (Q4), early apoptotic cells (Q3), and late apoptotic cells (Q4). **b,** statistical analysis of cells under different conditions after 48h QCA570 treatment.

QCA570 also induced apoptosis in a concentration-dependent manner in SCC1 **(Fig. 2-7)** and SCC1R **(Fig. 2-8)** cells. Even at a low dose of 0.1 nM, QCA570 triggered apoptosis, and as the dosage increased, a higher percentage of cells progressed to apoptosis. At a concentration as high as 100 nM, over 50% of the cell population underwent apoptosis. These findings demonstrate that QCA570 is a potent inducer of apoptosis in HNSCC cell lines, even in cells with cisplatin resistance.

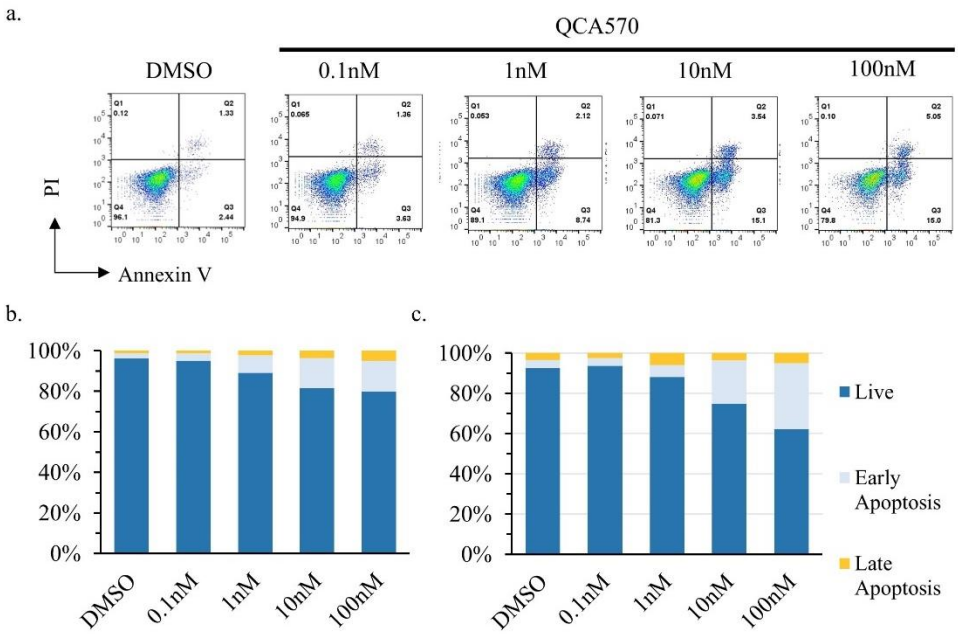

Fig. 2-7. QCA570 induced SCC1 cell apoptosis. a, gating method to separate live cells (Q4), early apoptotic cells (Q3), and late apoptotic cells (Q4). **b-c,** statistical analysis of cells under different conditions after 24-hour (b) or 48-hour (c) QCA570 treatment.

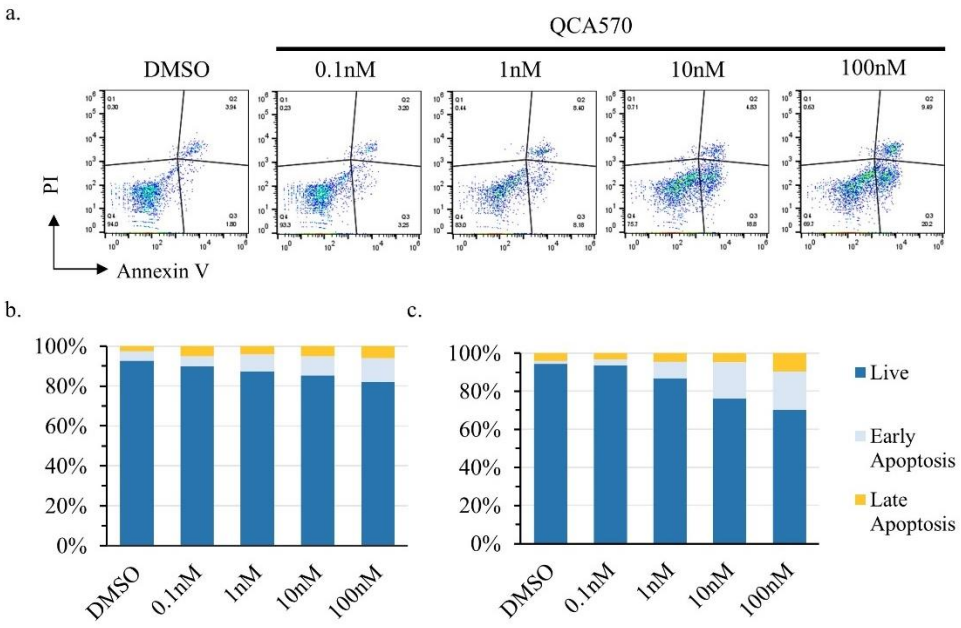

Fig. 2-8. QCA570 induced SCC1R cell apoptosis. a, gating method to separate live cells (Q4), early apoptotic cells (Q3), and late apoptotic cells (Q4). **b-c,** statistical analysis of cells under different conditions after 24-hour (b) or 48-hour (c) QCA570 treatment.

2.3.3 QCA570 suppressed HNSCC cell lines via degradation of BET family proteins.

Given that QCA570 was designed for degrading BET proteins[59], we next determined the effects of QCA570 on BET protein levels. In the two tested murine cell lines including MOC1 and cisplatin-resistant MOC1R, Western blot analysis confirmed that QCA570 effectively decreased the levels of BET family proteins, especially BRD2 and BRD4 **(Fig. 2-9)**. The reduction of these BET proteins occurred quickly after 4-hour treatment and could be achieved by QCA570 even at 1 nM. Hence, QCA570 indeed potently and rapidly decreased the levels of BET proteins in HNSCC cells.

c-Myc is a key regulator of cell proliferation[90]. In cancer, its abnormal activation plays a pivotal role in driving disease by orchestrating the upregulation of a transcriptional program that

promotes cell division, metabolic reprogramming, and survival[91,92]. MYC amplification is one of the most frequent genetic alterations found in cancer, highlighting its importance in tumor development[93]. c-Myc overexpression is responsible for poor tumor prognosis as well as the self-renewal of tumor stem cells in HNSCC[94–96]. Inhibition of BET family proteins using BET inhibitors has been shown to downregulate c-Myc expression in several cancer models[97,98]. In our study, QCA570 effectively decreased the levels of c-Myc in MOC1 **(Fig. 2-9 a)** and MOC1R **(Fig. 2-9 b)**, even at a low concentration of 1nM.

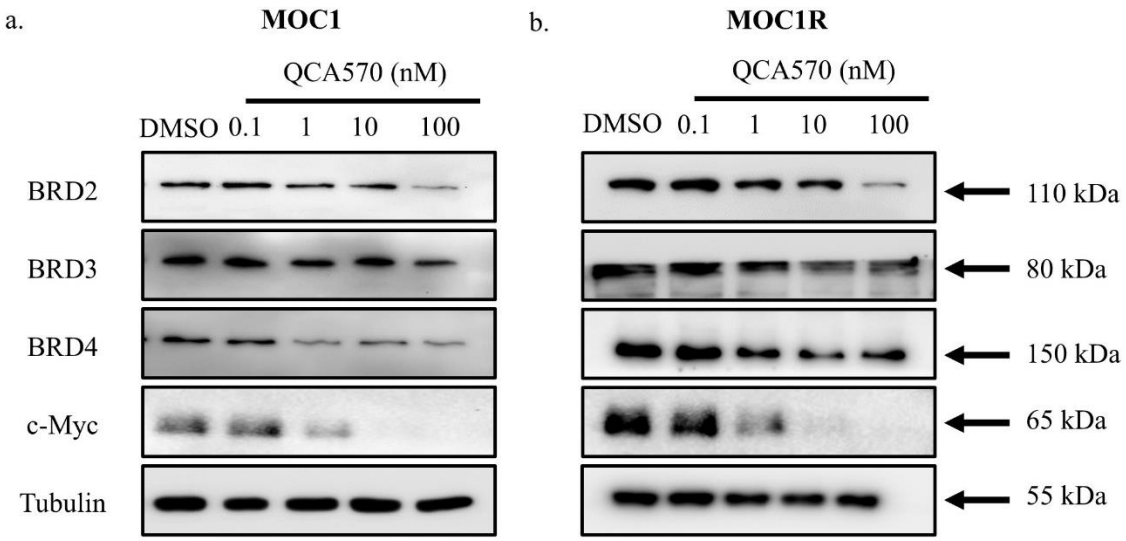

Fig. 2-9. QCA570 downregulated BET proteins and c-Myc expression in MOC1(a) and MOC1R (b) cells.

Treatment with QCA570 also led to a dose-dependent reduction in BET protein levels in both SCC1 **(Fig. 2-10 a)** and SCC1R **(Fig. 2-10 b)** cells. At lower concentrations (0.1 nM), a modest reduction in BRD protein expression was observed, while higher concentrations (up to 100 nM) led to a more pronounced suppression of BET proteins. In addition, QCA570 also disrupted c-Myc expression. Similar results were also found with SCC23 **(Fig. 2-11 a)** and SCC23R **(Fig. 2-11 b)** cells. These findings suggested that QCA570 not only reduced BET protein expression but

also interfered with its function, offering a potential therapeutic mechanism to target BET proteins in HNSCC.

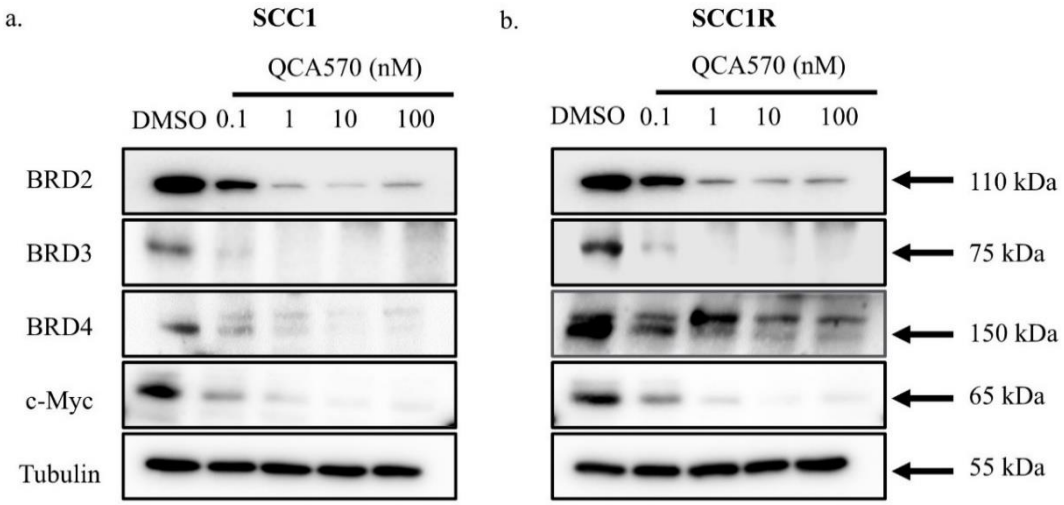

Fig. 2-10. QCA570 downregulated BET proteins and c-Myc expression in SCC1(a) and SCC1R (b) cells.

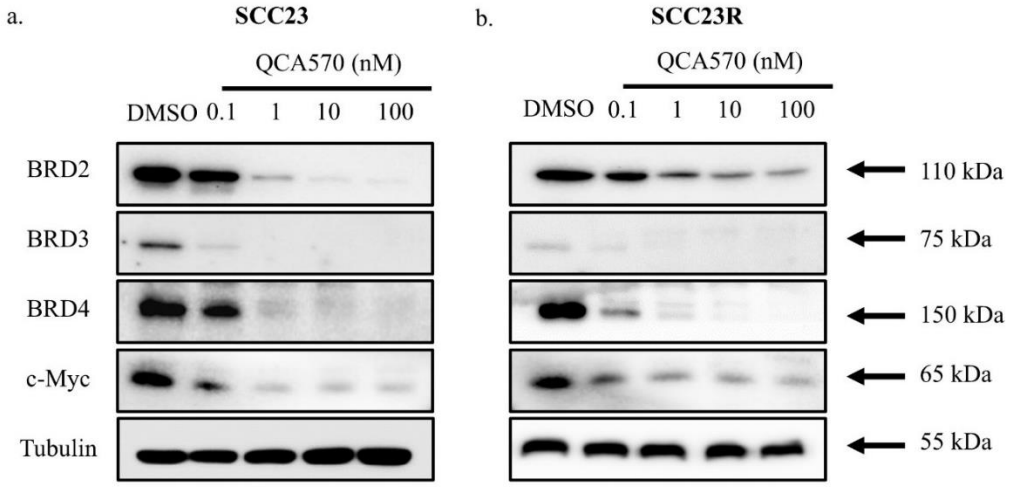

Fig. 2-11. QCA570 downregulated BET proteins and c-Myc expression in SCC23(a) and SCC23R (b) cells.

To further investigate the mechanisms by which QCA570 suppressed HNSCC, we performed RNA sequencing (RNA-seq) analysis of both SCC1 and SCC1R cells with or without

QCA570 treatment. Gene Ontology (GO) analysis was utilized to identify the function of QCA570 in HNSCC cells. Within this tool, genes and their products were categorized based on shared biological functions, cellular components, and molecular processes. By analyzing decreased genes after QCA570 treatment, results showed that multiple important cancer pathways were suppressed in SCC1 cells, including the MAPK signaling pathway, Wnt signaling Pathway, and TNF signaling pathway **(Fig. 2-12 a)**. Additionally, important cell functions like cell cycle and transcription were also interrupted by QCA570 treatment. And the pathways regulating the pluripotency of stem cells were downregulated, indicating possible anti-tumor effects through regulating cancer stem cells. Treatment with QCA570 on SCC1R cells presented similar results **(Fig. 2-12 b)**. Several pathways in cancer were suppressed by QCA570 treatment, including the MAPK signaling pathway, Wnt signaling pathway, TNF signaling pathway, and TGF-β signaling pathway. And the pathways regulating the pluripotency of stem cells were inhibited.

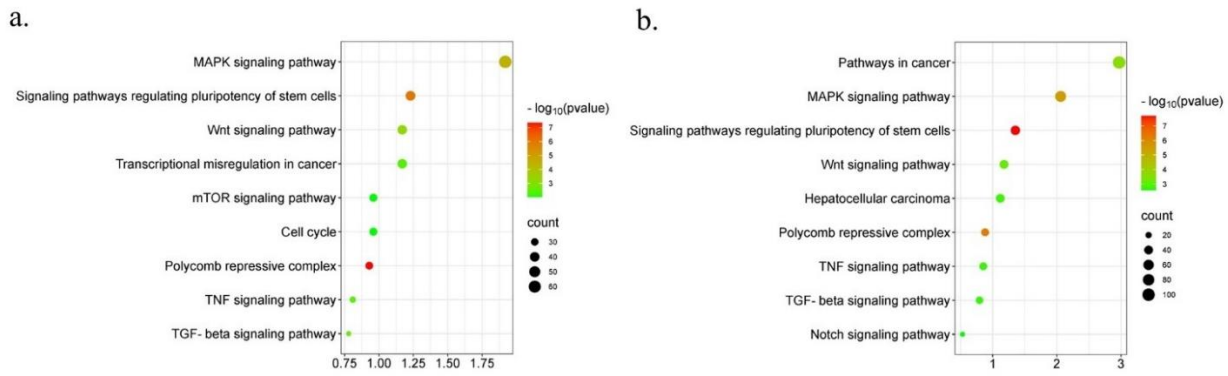

Fig. 2-12. Gene Ontology (GO) analysis of downregulated genes in SCC1 (a) and SCC1R (b) cells after QCA570 treatment.

Gene set enrichment analysis (GSEA) showed that several crucial cancer hallmark signatures were reduced after QCA570 treatment on SCC1 cells, including cell proliferation, Wnt/β-Catenin signaling, and MYC targets **(Fig. 2-13 a)**. Identical results were also found with

cisplatin-resistant SCC1R cells. After QCA570 treatment, the gene expression of cell proliferation, Wnt/β-Catenin signaling, and MYC targets was significantly decreased **(Fig. 2-13 b)**. Dysregulation of Wnt/β-catenin signaling is the most common alteration in cancers.[99] And c-Myc plays an important role in the Wnt/β-catenin pathway. The activation of c-myc gene expression is central to the signal transduction process in the Wnt/β-catenin pathway through the adenomatous polyposis coli (APC) tumor suppressor protein.[91,100] So it can be concluded from the GSEA results that QCA570 provided anti-cancer efficacy on both SCC1 and SCC1R cells via suppressing c-Myc expression followed by dysregulation of Wnt/β-catenin signaling and downregulation of c-Myc target genes.

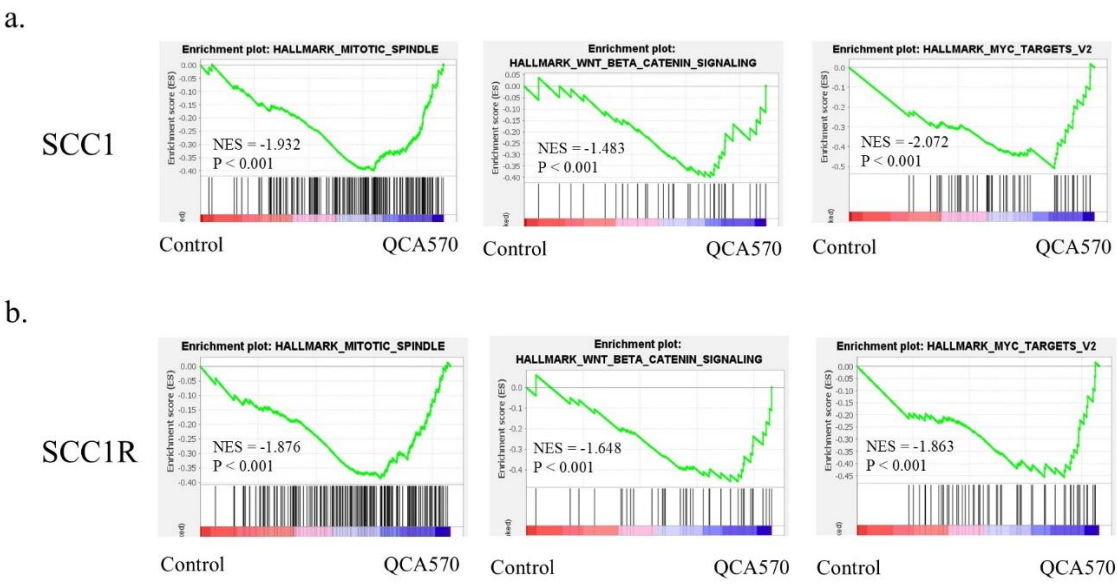

Fig. 2-13. Gene set enrichment analysis (GSEA) of downregulated genes in SCC1 (a) and SCC1R (b) cells after QCA570 treatment. NES: Normalized Enrichment Score.

2.3.4 Fabrication of microneedles with QCA570-loaded microparticles.

Although the efficacy of QCA570 to degrade BET proteins, reduce HNSCC cell proliferation and invasion, and induce apoptosis was proved in vitro, in vivo utilization of QCA570

is challenging, mainly because traditional intraperitoneal injection could lead to biosafety issues, and multiple doses were needed for intravenous injection to achieve tumor regression[59]. To overcome those, microneedle patches were fabricated to achieve a targeted and continuous release of QCA570.

The designed microneedle patches had two parts: a quickly dissolvable base part and needle tips loaded with drug-containing microparticles **(Fig. 2-14)**. The supporting membrane was made of polyvinylpyrrolidone (PVP), which not only provided physical support for the drug-loaded needle tips, but also dissolved within minutes in a humid environment to maximize the release of microparticles. Poly (lactic-co-glycolic acid) (PLGA) was chosen as the microparticle material due to its biodegradability and biocompatibility. PLGA's biodegradability results from ester linkages degraded by hydrolysis in aqueous environments. The degradation rate is influenced by the glycolide content, where fewer glycolide units in the structure extend degradation time[101]. This tunable biodegradability of PLGA allows the design of microparticles with programmable, time-controlled drug release[101–103]. PLGA is also evaluated as a biocompatible polymer for drug delivery[104–106]. The use of PLGA has been approved by the Food and Drug Administration (FDA).

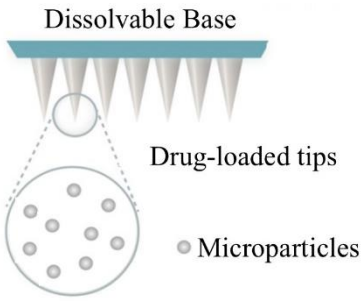

Fig. 2-14. Illustration of the microneedle patch design.

PLGA microparticles were synthesized using the single oil in water (O/W) emulsion technique, which is one of the most common procedures used to encapsulate hydrophobic drugs[107,108]. Briefly, PLGA and QCA570 were first dissolved together in appropriate organic solvents to form the oil phase. Then it was added by homogenization to the water phase, which is made up of water and polyvinyl alcohol (PVA) as an emulsifying agent. The microparticles are formed during the elimination of the solvent by evaporation. The speed of the homogenizer is the key factor to determine the particle size. **Fig. 2-15 a** showed the morphology of PLGA microparticles under different synthesis conditions. With a low speed of 3000 rpm, the average particle size was 55 μm. As the speed increased, particle size decreased. 5000 rpm led to a particle size of 10 μm, while 20,000 rpm produced particles with a diameter of 5 μm **(Fig. 2-15 b)**.

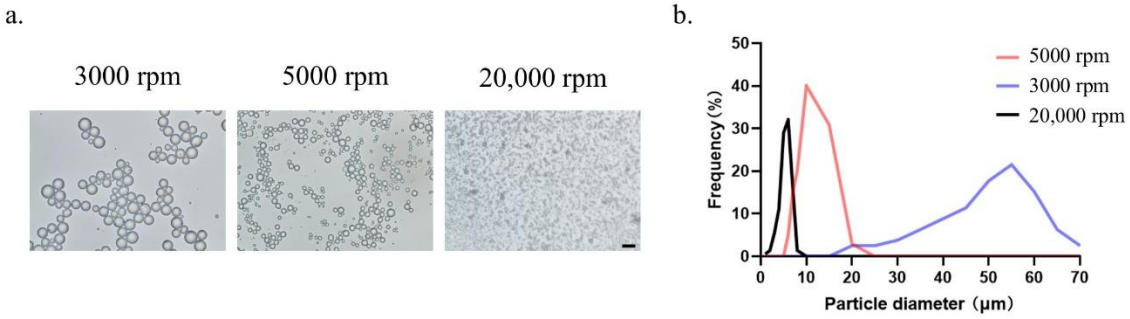

Fig. 2-15. Microparticle sizes with different homogenization speeds. a, optical microscope images of PLGA microparticles. Scale bar, 50 μm. **b,** statistical analysis of PLGA microparticles with different speeds for the homogenizer.

The fabrication process of the microneedle is illustrated in **Fig. 2-16 a.** 10% (w/v) PVP containing QCA570-loaded microparticles were cast on negative MN molds and centrifuged to fill the tip. The extra mixture was removed, and the needle tips were dried at room temperature. Then 20% PVP was added on top of the needle tips to fill the mold and create microneedle patches. After

drying at room temperature, the microneedle patches were peeled off from the molds. As shown in optical microscopy images, the resulting microneedles were conical, with a base diameter of 300 μm, a height of 800 μm, and a tip diameter of ~15 μm **(Fig. 2-16 b)**. The microparticles were successfully loaded into the microneedle patches, and the loading of microparticles didn't affect the microneedle structure. Compared with the microneedle patches without the centrifugation step, microparticles accumulated more at the tips of the needle instead of the base part after centrifugation because of the high density of PLGA microparticles **(Fig. 2-16 c)**.

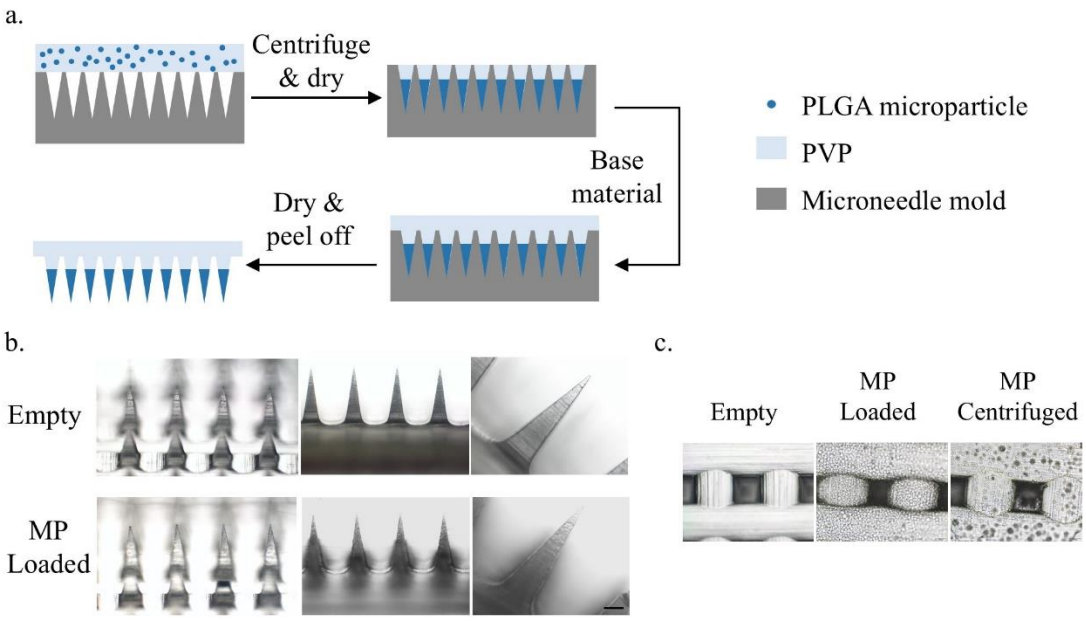

Fig. 2-16. Fabrication process and optical microscope images of microneedle patches. a, illustration of the synthesis process of microneedle patches loaded with PLGA microparticles. **b**, optical microscope images of microneedle patches with or without PLGA microparticles. Scale bar, 100 μm. **c**, optical microscope pictures of empty microneedle patches and microneedle patches loaded with PLGA microparticles with or without centrifuge step from the base view. MP: microparticles.

2.3.5 Characterization of microneedles with QCA570-loaded microparticles.

QCA570 drug release at pH 7.4 was characterized by analyzing the accumulative release in vitro. The Microneedle patches' PVP base dissolved quickly in the aqueous environment within 5 minutes. Drug release from the PLGA microparticles was further studied by monitoring the QCA570 concentration every two days. **Fig. 2-17** demonstrated that the size of the microparticles, determined mainly by the homogenization speed during the fabrication process, was the key factor in the QCA release profile. With a high homogenization speed of 20,000 rpm, all loaded QCA570 was released after 10 days. As the homogenization speed decreased, the microparticle size increased, while the drug release speed decreased. 5000 rpm microparticles released all the QCA570 inside within 18 days. The 3000 rpm microparticles released the QCA570 much slower than the other two groups at the beginning, and it took 24 days for those microparticles to finish releasing. Based on the release profile, microneedles loaded with the 5000 rpm PLGA-QCA570 particles with an average diameter of 10 μm were used in further in vitro characterizations and also in vivo studies.

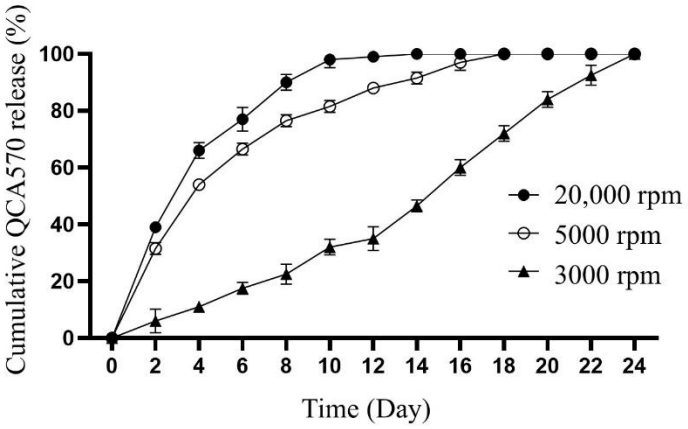

Fig. 2-17. Release profile of QCA570 from the microneedle patches

The mechanical properties of microneedle patches are critical for their effectiveness and safety. Compression test was performed on microneedle patches with and without microparticles **(Fig. 2-18)**. Each needle tip could afford up to 1.2 N pressure, indicating that these microneedles had sufficient mechanical strength to penetrate the skin or oral mucosa[109,110]. Adding microparticles did not significantly affect the mechanical properties of microneedles.

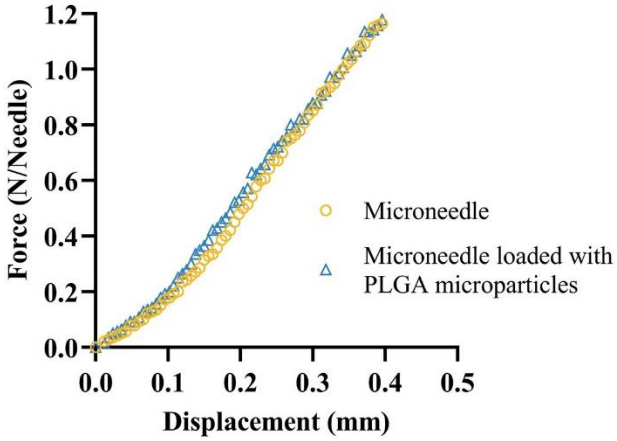

Fig. 2-18. Mechanical properties of microneedle patches with or without PLGA microparticles.

2.3.6 QCA570-loaded microneedle suppressed cisplatin-resistant tumor progression.

Cell line-derived xenografts, which are established by transplanting cancer cell lines into immunocompromised mice, could create microenvironments closer to the tumor's physiological and pathological conditions, providing a more advanced strategy to reflect the behaviors of the original cancer cells in patients compared to in vitro cell culture[111]. In this study, NU/J mouse cisplatin-resistant HNSCC model was used to measure the function of microneedle patches in vivo. SCC1R cells (2×10^6 cells/mouse) were injected subcutaneously into the flank of 6-week-old NU/J mice **(Fig. 2-19 a)**. Three doses of cisplatin were given to mice to ensure the treatment resistance

against cisplatin. After the average tumor size reached 150 mm^3, mice were randomly divided into two groups and given the 1) vehicle control, and 2) microneedle patches with QCA570-loaded PLGA microparticles. The tumor size was monitored twice a week **(Fig. 2-19 b)**. The microneedle patches reduced the tumor growth right after application. And the suppress effect became statistically significant 7 days after the treatment. Although only one dose of microneedle patches was applied, the tumors in the treatment group kept a much slower growth rate than the vehicle control group throughout the whole treatment window, indicating the success of continuous release of QCA570 for at least 14 days. **Fig. 2-19 c** showed pictures of dissected tumors. Tumors in the microneedle treatment group were smaller than those in the vehicle control group. The tumor weights were also measured. The microneedle patches reduced the tumor weight to one-third of the control group **(Fig. 2-19 d)**. The results proved that the QCA570 loaded in microneedle patches was effective in suppressing tumors that were resistant to cisplatin treatment. And the PLGA particles delivered by the microneedle patch continuously released QCA570 for at least 14 days to achieve treatment efficacy.

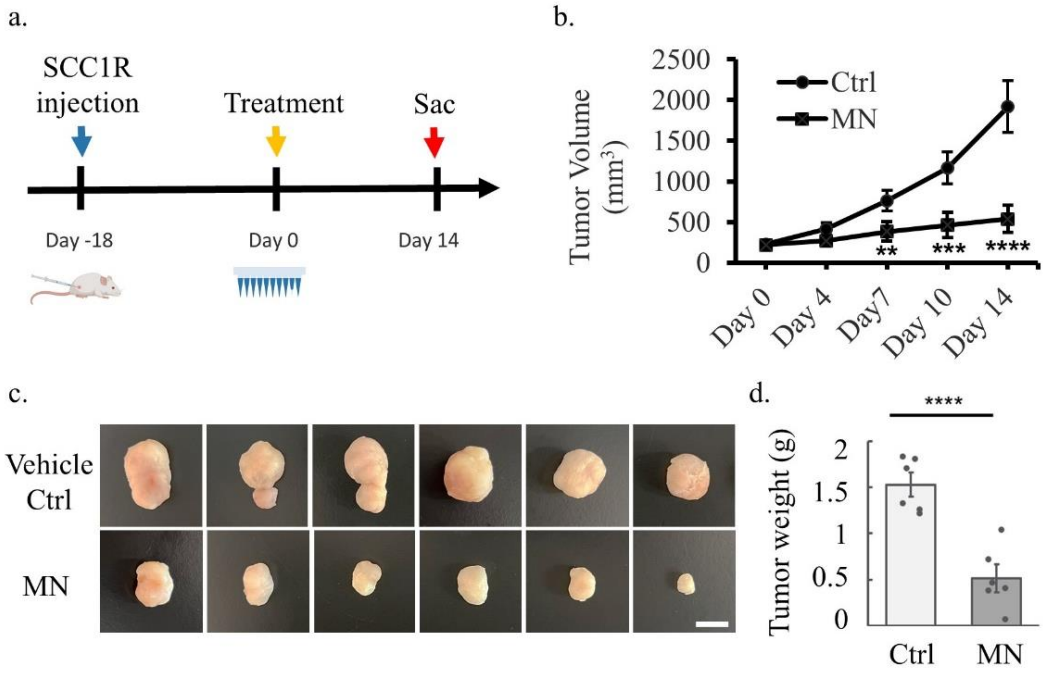

Fig. 2-19. Treatment efficacy of designed microneedle patches on cisplatin-resistant HNSCC mouse model. a, the timeline of the animal experiment. **b**, tumor growth in the vehicle control group (Ctrl) and the microneedle patch treatment group (MN). The tumor volume was monitored, measured, and calculated twice a week. **c**, pictures of tumors in the vehicle control group (Ctrl) and the microneedle patch treatment group (MN) 14 days after treatment. Scale bar, 1 cm. **d**, statistical analysis of the tumor weight in the vehicle control group (Ctrl) and the microneedle patch treatment group (MN) 14 days after treatment. * $p<0.1$, ** $p<0.05$, *** $p<0.01$, **** $p<0.001$.

Immunostaining was performed on tumors 14 days post microneedle patch application. QCA570 was released from the PLGA microparticles and continued to successfully degrade BET family proteins, for example, BRD2 **(Fig. 2-20 a)**. The IHC score for the vehicle control group is around 220, while the score is under 100 for the microneedle patches treated group **(Fig. 2-20 b)**. At the same time, staining of Ki-67, a cellular marker commonly used to assess cell

proliferation[112,113], revealed that the QCA570 delivered by the microneedle patches was able to reduce the number of proliferating tumor cells **(Fig. 2-20 c)**. The IHC score for the vehicle control group is above 200, but in the microneedle patches treatment group, the score is significantly reduced to under 100 **(Fig. 2-20 d)**.

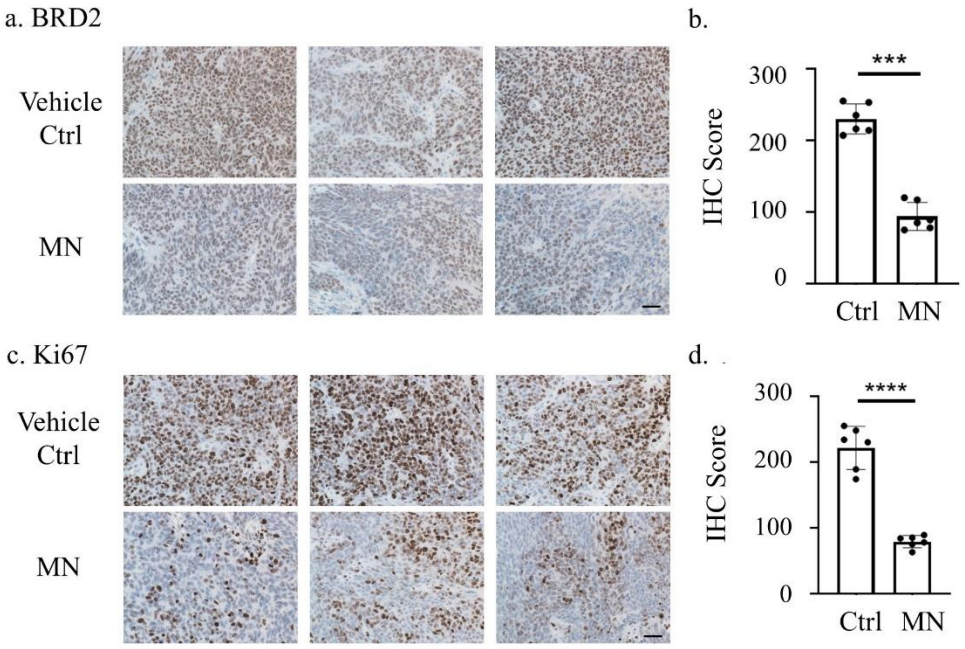

Fig. 2-20. Immunohistology staining of SCC1R tumors treated with vehicle control (Ctrl) or microneedle patches (MN). a-b, immunohistology staining (a) and calculated IHC score (b) of BRD2 in SCC1R tumors. **c-d**, immunohistology staining (c) and calculated IHC score (d) of Ki67 in SCC1R tumors. Scale bar, 100 μm. * $p<0.1$, ** $p<0.05$, *** $p<0.01$, **** $p<0.001$.

The systemic toxicity was also investigated. There is no significant change in the mouse body weight between the vehicle control group and the microneedle treatment group throughout the animal experiment **(Fig. 2-21)**. In addition, during the dissection, no significant pathophysiological changes were found in the major organs, including the heart, liver, spleen, lungs, kidneys, and brain, demonstrating a biosafety profile in vivo.

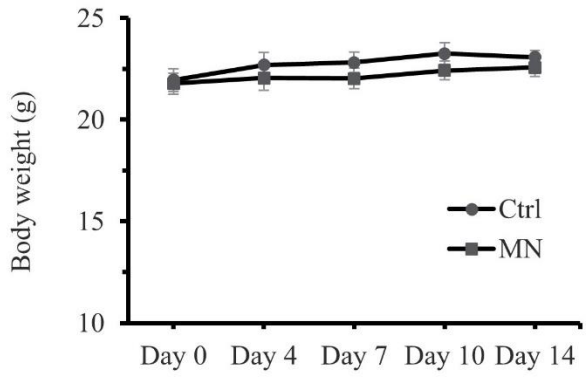

Fig. 2-21. Mouse body weight changes in vehicle control (Ctrl) and microneedle patch treatment (MN) groups during the experiment.

2.3.7 QCA570-loaded microneedle suppressed human PDX tumor progression.

Patient-derived xenograft (PDX) mouse models, which are established by direct engraftment of patient-derived tumor fragments into immunocompromised mice, have attracted attention and become potential tools for both basic and preclinical cancer research in recent years[114]. Since PDXs have been suggested to retain morphologies, architectures, and molecular signatures very close to those of the original tumors, they could overcome the disadvantage of cell line-derived xenograft, where the cancer cell line employed might have already lost some original characteristics through adaptations to in vitro growth[115].

To establish the PDX model, human HNSCC primary tissues were subcutaneously inoculated into the right flank of 6-week-old NSG mice. 20 days after the implantation, mice were randomly divided into two groups and given the 1) vehicle control, and 2) microneedle patches QCA570 loaded PLGA microparticles as treatment **(Fig.2-22 a)**. Tumor size was measured twice a week **(Fig. 2-22 b)**. The microneedle patches immediately slowed tumor growth after application, with the suppressive effect becoming statistically significant by day 4. Despite a single dose of microneedle patches, tumors in the treatment group grew at a significantly slower rate than those

in the vehicle control group, indicating sustained release of QCA570 for at least 14 days. Images of dissected tumors **(Fig. 2-22 c)** revealed that tumors in the treatment group were visibly smaller than those in the control group. Additionally, tumor weights were reduced to one-third of the control group **(Fig. 2-22 d)**. These findings demonstrate that with the PLGA particles continuously releasing QCA570 over a minimum of 14 days, QCA570-loaded microneedle patches effectively suppressed tumors in the PDX model.

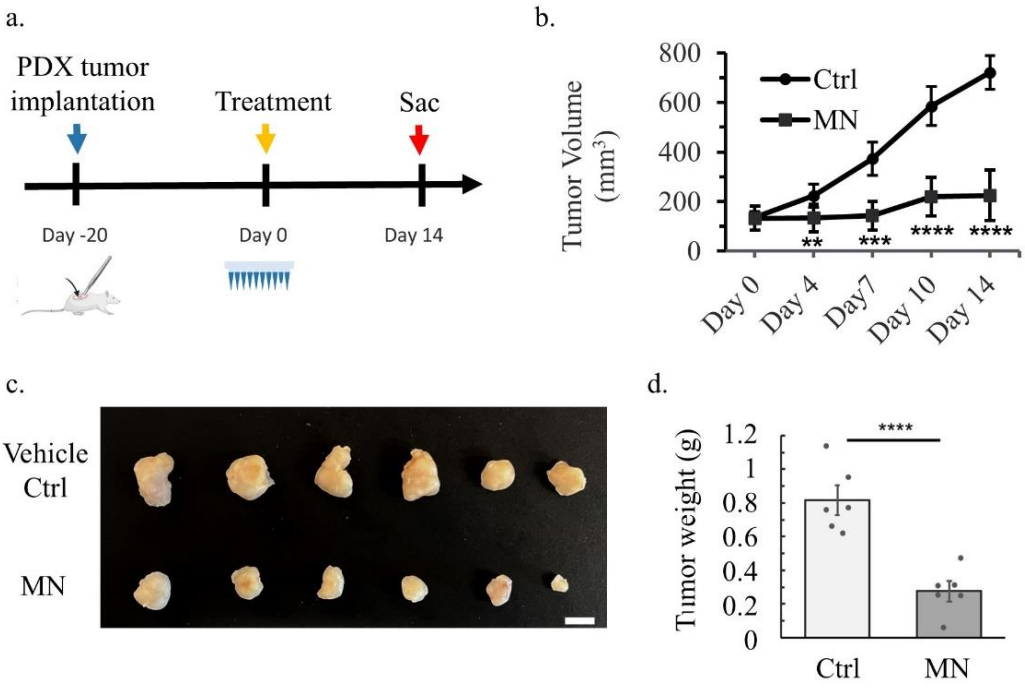

Fig. 2-22. Treatment efficacy of designed microneedle patches on HNSCC PDX model. a, the timeline of the animal experiment. **b**, tumor growth in the vehicle control group (Ctrl) and the microneedle patch treatment group (MN). The tumor volume was monitored, measured, and calculated twice a week. **c**, pictures of tumors in the vehicle control group (Ctrl) and the microneedle patch treatment group (MN) 14 days after treatment. Scale bar, 1 cm. **d**, statistical analysis of the tumor weight in the vehicle control group (Ctrl) and the microneedle patch treatment group (MN) 14 days after treatment. * $p<0.1$, ** $p<0.05$, *** $p<0.01$, **** $p<0.001$.

14 days after applying the microneedle patches, tumors were collected and immunohistology staining was conducted. QCA570 released from the PLGA microparticles effectively degraded BET family proteins, such as BRD2 **(Fig. 2-23 a)**. The IHC score for the vehicle control group was around 220, while it dropped below 100 in the microneedle-treated group **(Fig. 2-23 b)**. Additionally, staining for the cell proliferation marker Ki-67 showed that the QCA570 delivered by the microneedle patches significantly reduced tumor cell proliferation **(Fig. 2-23 c)**. In the control group, the IHC score exceeded 260, whereas in the microneedle treatment group, the score was notably reduced to below 100 **(Fig. 2-23 d)**.

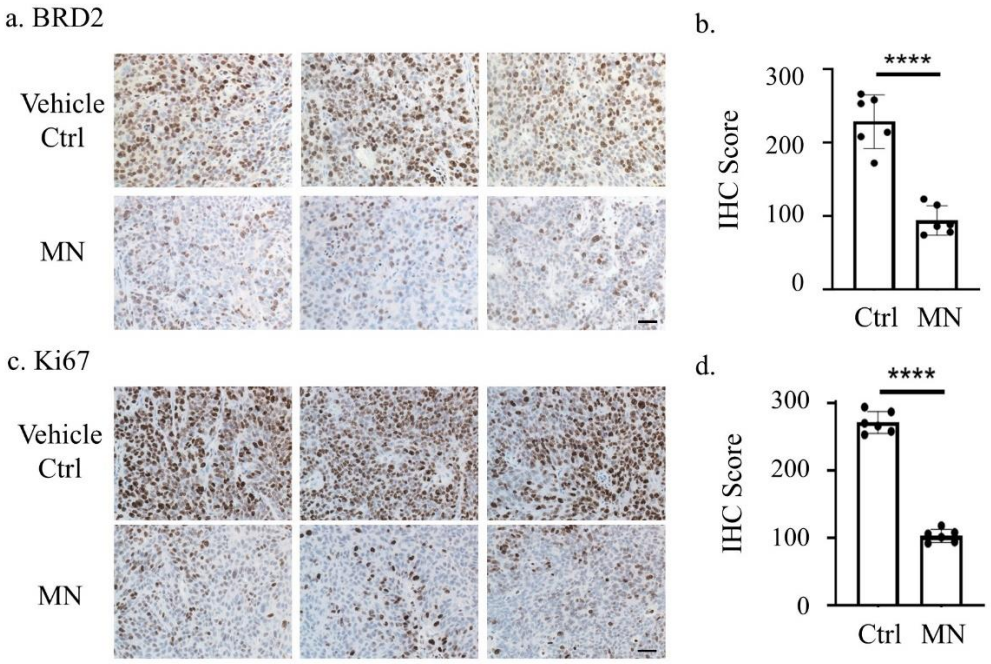

Fig. 2-23. Immunohistology staining of PDX tumors treated with vehicle control (Ctrl) or microneedle patches (MN). a-b, immunohistology staining (a) and calculated IHC score (b) of BRD2 in SCC1R tumors. **c-d**, immunohistology staining (c) and calculated IHC score (d) of Ki67 in SCC1R tumors. Scale bar, 100 μm. * $p<0.1$, ** $p<0.05$, *** $p<0.01$, **** $p<0.001$.

The body weight of mice was monitored to evaluate the systemic toxicity. No significant differences in body weight were observed between the vehicle control group and the microneedle-treated group throughout the study **(Fig. 2-24)**, indicating a favorable biosafety profile. Moreover, during the dissection, no notable pathophysiological abnormalities were detected in the major organs, such as the heart, liver, spleen, lungs, kidneys, and brain.

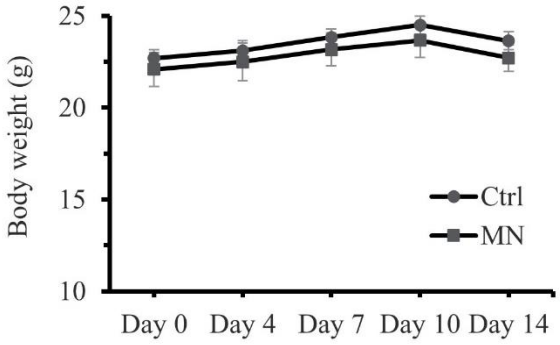

Fig. 2-24. Mouse body weight changes in vehicle control (Ctrl) and microneedle patch treatment (MN) groups during the experiment.

2.4 Conclusion and discussion.

2.4.1 Conclusions.

In this study, we evaluated the therapeutic potential of a novel small molecule drug, QCA570, on head and neck squamous cell carcinoma (HNSCC). Our results demonstrate that QCA570 effectively inhibits the proliferation and invasion while inducing apoptosis of both cisplatin-sensitive and resistant HNSCC cell lines in a dose-dependent manner. Additionally, QCA570 downregulated key proteins involved in cell survival, such as the BET family and c-Myc, and impacted related signaling pathways.

To translate our developments to cancer patients, microneedles were designed to achieve targeted and sustained released of QCA570 in vivo. QCA570 was successfully loaded in PLGA

microparticles by the oil in water emulsion. And the ideal release rate was achieved by controlling the size of the microparticles. Microneedles were successfully fabricated, with drug-loaded PLGA microparticles concentrated at the needle tips to achieve higher delivery efficiency. The designed microneedles efficiently delivered QCA570 to the tumor site, continuously released QCA570 for 14 days, and significantly reduced the growth of both cisplatin-resistant xenograft tumors and PDX tumors without causing any biosafety issues. These findings suggest that QCA570 could be a promising therapeutic agent for treating both cisplatin-sensitive and resistant HNSCC. The microneedle technology could be a promising tool for localized, minimally invasive treatment of HNSCC, offering a novel alternative to conventional systemic drug delivery routes.

2.4.2 Discussion.

Our findings highlight the effectiveness of QCA570 in targeting HNSCC cells, including those resistant to conventional chemotherapy like cisplatin. The small molecule's ability to induce apoptosis and suppress cancer cell proliferation through multiple mechanisms makes it a potential candidate for overcoming drug resistance, a major challenge in treating advanced HNSCC. The dose-dependent downregulation of BET proteins and c-Myc underscores the potential of QCA570 to disrupt key pathways, for example, the Wnt/β-catenin signaling pathway, to control tumor growth and progression. The wnt/β-catenin signaling pathway is associated with stem cell property or self-renewal. Recent studies suggested that tumorigenic cancer cells undergo processes that are analogous to the self-renewal and differentiation of normal stem cells[116]. Those so-called cancer stem cells (CSCs) play a critical role in the invasive growth and metastasis of HNSCC[58]. Investigating the role of QCA570 on cancer stem cells could be a possible direction to better understand the working mechanism of QCA570 on HNSCC.

Compared to traditional treatments like surgery, radiation, and chemotherapy, which often result in significant side effects and damage to surrounding healthy tissues, QCA570 delivered by microneedles offers a more precise and targeted therapeutic approach. The use of microneedles as a drug delivery system for HNSCC presents several advantages over traditional methods. First, the ability of microneedles to bypass the skin barrier makes them an ideal platform for transdermal delivery of cancer therapeutics, especially in regions like the head and neck where access is challenging with conventional treatments. Secondly, the localized delivery achieved by the PLGA particles allowed for a more concentrated dose at the tumor site, enhancing therapeutic efficacy while reducing systemic exposure and the risk of off-target toxicity. This precision is particularly beneficial in HNSCC, where preserving surrounding healthy tissues is crucial for maintaining essential functions like speech and swallowing. Secondly, compared to oral or intravenous administration where multiple doses were necessary, fewer doses were needed with microneedles due to the localized delivery and increased antitumor efficiency. Meantime, the most significant limitation of dissolvable microneedles is their low drug loading capacity, which is overcome by the high treatment efficacy of QCA570 compared to other traditional drugs and the decrease in therapeutic dosage accomplished by microneedle-mediated target delivery. Finally, combination therapies, potentially alongside immunotherapies or other molecular inhibitors, could enhance the efficacy of QCA570 and reduce the likelihood of tumor recurrence. Microneedles can also be easily modified for a combinatory approach with two or more different therapies at the same time, providing more possibilities for HNSCC treatment.

While the current study underscores the promise of QCA570-loaded microneedle technology as a minimally invasive, targeted, and patient-friendly treatment for HNSCC, additional research is needed for the pharmacokinetics, optimal dosage, and long-term effects of

QCA570 in vivo. Besides, orthotopic animal models, like 4-nitroquinoline 1-oxide (4NQO) - induced mouse HNSCC, are preferred to better mimic human HNSCC progressing gradually from dysplasia and papilloma (carcinoma in situ) to squamous cell carcinoma[88,98,117]. Optimizing the design of the microneedles is also needed to better fit the humid environment in the oral cavity. In addition, clinical trials will be essential to validate current findings and determine the scalability of this technology for broader cancer treatment applications.

Chapter 3: Advancing head and neck squamous cell cancer treatment with targeted delivery of therapeutic enzymes.

3.1 Introduction.

3.1.1 Tumor microenvironment.

Our understanding of cancer has transformed dramatically in recent decades. Attention has been predominately focused on cancer cells, given that genetic mutations are essential for cancer development. However, more and more research showed that cancer cells alone do not drive cancer initiation and progression[118,119]. In fact, only 5–10% of cancer cases can be attributed to genetic defects, with 90–95% of all cancer cases having their roots in the environment and lifestyle[120]. Cancer is now viewed not merely as a genetic disease driven by the accumulation of mutations in cancer cells, but as a complex ecosystem involving numerous non-cancerous cells, like stromal cells and immune cells, and their dynamic interactions within the tumor[121]. The development and maintenance of cancer hallmarks, such as continuous proliferative signaling, resistance of cell death, promotion of angiogenesis, activation of invasion and metastasis, induction of tumor-supportive inflammation, and immune evasion, are supported not only by cancer cells, but also by elements within the tumor microenvironment (TME) to various degrees. This dependence on the

TME opens new avenues for therapy by targeting TME components or their associated signaling pathways.

The tumor microenvironment (TME) is a highly organized network where cancer cells coexist with a variety of non-malignant cell types within a remodeled, vascularized extracellular matrix. The TME includes an array of immune cells, including T and B lymphocytes, tumor-associated macrophages (TAM), dendritic cells (DC), natural killer (NK) cells, neutrophils, and myeloid-derived suppressor cells (MDSC); stromal cells such as cancer-associated fibroblasts (CAFs), pericytes, and mesenchymal stromal cells; the extracellular matrix (ECM) and other secreted molecules, such as growth factors, cytokines, chemokines, and extracellular vesicles (EV); and the blood and lymphatic vascular networks, which are collectively enmeshed and in communication with each other and with the heterogeneous cancer cells themselves[122,123]. Initially, the surrounding host cells were believed to be passive participants in tumor development. However, mechanistic studies, especially those using preclinical tumor models, have revealed that cells within TME and the molecules they secrete play active roles in advancing cancer, making them potential targets for therapeutic intervention[124].

Among all components in TME, targeting immune checkpoints on tumor-infiltrating T-cells to booster anti-tumor immunity and the functions of those T-cells have been one of the most discussed directions of innovative cancer therapies[125–128]. $CD8^+$ T cells are key players in the immune system's response to tumors. These cells recognize cancer cells by binding their T cell receptors (TCRs) to the major histocompatibility complex (MHC) displayed on cancer cells. Once activated, $CD8^+$ T cells eliminate cancer cells either by inducing apoptosis via granzyme and perforin release or through cell death mediated by FASL-FAS[129]. Within tumors, $CD8^+$ T cells often show a dysfunctional or exhausted phenotype[130]. Activation of these $CD8^+$ T cells can

enhance their ability to target and destroy cancer cells effectively. $CD4^+$ helper T cells regulate various immune cells and are particularly important for enhancing $CD8^+$ T cell responses. In cancer, the Th1 subtype exhibits anti-tumor effects by supporting cytotoxic $CD8^+$ T cells and B cells, as well as by directly killing cancer cells through the release of interferon γ (IFN-γ) and TNF-α. Conversely, the Th2 subtype releases anti-inflammatory molecules that promote tumor growth. Increasing evidence suggests that $CD4^+$ T cells are also crucial to the success of immune therapies[131].

3.1.2 Cisplatin-resistance from tumor microenvironment.

Although cisplatin has shown significant clinical efficacy in cancer treatment, drug resistance has limited its therapeutic success for decades[36]. Cisplatin's primary cytotoxic effect involves its binding to DNA within tumor cells, leading to cell death. Consequently, traditional studies on cisplatin resistance have primarily examined internal cellular processes, including drug accumulation, DNA damage repair, and apoptosis pathways. However, tumor growth is a complex, dynamic process involving close interactions with the surrounding microenvironment, particularly under the stress of chemotherapy[132]. Increasing research highlights the role of TME in promoting chemotherapy resistance, thereby influencing the effectiveness of treatments like cisplatin in targeting cancer cells[133,134].

Generally, the TME factors affecting drug resistance can be categorized into two groups: physical and biological components **(Table 3-1)**. Physical components that interfere with the delivery and efficacy of cisplatin include high cell density as physical barriers to prevent peneration[135,136], fluidic shear stress[137], and the extracellular matrix (ECM)[138]. The biological component group consists of biochemical consequences of tumor growth, (e.g., hypoxia[139–143] and acidity[144,145]) and noncancerous cells (e.g., stromal cells, tumor-associated fibroblasts[146–151], and

immune cells[152,153]). And the cisplatin resistance mechanisms include limited drug delivery efficiency, cell death inhibition, drug inactivation, cell stemness promotion, or any combination of these factors.

Factor	Action mechanism	Experimental result
Physical		
Physical barriers	Limit penetration of cisplatin into tumors	Decreased cisplatin accumulation in tumor cells
Fluidic shear stress	Activation of PI3K/Akt signaling and ABC drug transporters	Cancer stemness progression and cisplatin resistance induced by fluidic shear stress
ECM	1. Limited cisplatin diffusion	Increased cancer cell sensitivity to cisplatin in collagen- and fibronectin-deficient ECMs
	2. The activation of survival signals through the interaction with tumor cells	
Biological		
Hypoxia	Increased cancer cell stemness and multidrug transporter expression	Increased cisplatin resistance in low oxygen levels
Acidity	Increased multidrug transporter expression	Increased cisplatin resistance in acidic conditions
CAF	1. CAF-secreted growth factors or cytokines affecting cell apoptosis or intrinsic drug resistance	1. Increased cisplatin resistance by CAF-secreted cytokines such as IL-6, IL-8, IL-11, insulin-like growth factor 1, and TGF-β
	2. Metabolism of CAFs regulated by effector T-cells	2. CAFs-mediated GSH metabolism and platinum resistance abrogated by cytotoxic T cells
TAM	Secretion of cytokines by TAM in an M2 polarization state	Increased cisplatin resistance by TAM-secreted cytokines such as IL-6 and type I interferon

Table 3-1. Tumor microenvironment factors reported with cisplatin resistance. PI3K: phosphatidylinositol 3-kinase, ABC: ATP-binding cassette transporter, ECM: extracellular matrix,

CAF: carcinoma-associated fibroblast, TAM: tumor-associated macrophage, IL: interleukin, TGF: transforming growth factor, GSH: glutathione.

3.1.3 Target the lactate in the tumor microenvironment for cancer treatment.

Cellular transformation including uncontrolled proliferation, resistance to apoptosis, evasion of the immune response, and the ability to circumvent growth inhibitory signals, all contribute to the development of cancer. As part of the tumor survival machinery, tumor cells have been found to adapt their metabolism to overcome the various challenges, which has been recognized as a hallmark of cancer[154,155]. In normal tissues, energy is primarily derived from aerobic respiration in the presence of oxygen, while glycolysis provides energy only in anaerobic conditions. On the contrary, known as the Warburg effect, tumor cells often favor a low adenosine triphosphate (ATP)-generating glycolytic pathway, even in oxygen-rich environments[156,157]. This metabolic choice allows tumor cells to better adapt to fluctuations in oxygen partial pressure. Besides supplying energy, the intermediates from glycolysis are necessary for synthesizing macromolecules such as proteins, nucleic acids, and lipids, which support rapid tumor cell growth and proliferation. Although glycolysis yields less ATP than aerobic respiration, it generates ATP at a faster rate, meeting the high energy demands of rapidly proliferating tumors. Furthermore, relying on glycolysis minimizes electron transport chain activity in mitochondria, and anaerobic glycolysis reduces reactive oxygen species (ROS) production, thereby decreasing toxicity to cancer cells[157].

Cancer cells consume significant amounts of glucose, resulting in elevated levels of extracellular lactate. Lactate, once deemed merely a waste product, is now recognized as playing a crucial role in various oncogenic processes, including tumor cell survival, oncogenic signaling [158], inflammation, metastasis[159], and tumor resistance[160]. Recent studies found that the elevated

lactate level also impacts immune cells[161] and plays an important role in immunosuppression[162,163]. In the early phases of tumor growth, immune cells recruited and activated by tumor cells may create an inflammatory microenvironment that suppresses tumor progression. However, as tumor cells proliferate and continuously activate the immune response, the TME experiences dynamic shifts: immune effector cells become exhausted or undergo remodeling, leading to impaired functionality. A significant factor driving these changes is the high lactate concentration associated with the Warburg effect, which impacts the differentiation, metabolism, and functionality of tumor-infiltrating immune cells through multiple pathways[164].

Currently, extensive trials that aim to regulate lactate levels mainly utilize multiple strategies to inhibit lactate dehydrogenase (LDH), the key enzyme responsible for converting lactate to pyruvate in the presence of nicotinamide adenine dinucleotide (NAD^+) and its reduced form (NADH)[165]. Recent studies showed that the expression of LDH is upregulated in some tumor clinical samples[166,167], while the downregulation of LDH can inhibit the growth and migration of cells in vitro and affect the occurrence of tumors in vivo[168]. However, the use of LDH inhibitors poses a risk of disrupting the metabolism of normal cells, leading to significant off-target toxicity. Therefore, alternative approaches are needed to lower lactate levels without affecting surrounding tissues.

The lactate oxidase (LOx), produced from bacteria (such as Aerococcus viridans), catalyzes the oxidation of lactate to pyruvate and hydrogen peroxide (H_2O_2) without additional coenzyme, which promotes the wide application of LOx in the biomedical field[169]. The use of LOx to catalyze the change of lactate present in large amounts in tumors not only provides a tumor microenvironment more suitable for immune cell filtration, but H_2O_2 can be converted to highly toxic hydroxyl radicals (•OH) catalyzed by other compounds, thus killing tumor cells and inhibit

tumor growth[170,171]. In addition, H_2O_2 was found to effectively increase the secretion of proinflammatory cytokines such as interferon-γ (IFN-γ) in immune cells, which activates T cells and directs their migration toward and within tumors[172,173]. Thus, the utilization of LOx to decrease tumoral lactate levels and increase H_2O_2 concentrations could be an effective strategy for cancer treatment.

3.1.4 Nanoencapsulation platform as a novel enzyme delivery route.

Proteins are macromolecules that participate in a wide range of biological processes and serve essential functions, such as catalyzing reactions, facilitating high-affinity molecular recognition, and modulating cellular pathways[174]. These functions make proteins highly attractive as therapeutic agents. Compared to small-molecule drugs, proteins offer a unique therapeutic potential with greater specificity and a broader spectrum of activity, which has led to extensive research on proteins for diverse medical applications: for example, ribonuclease A (RNAse A) has been explored in cancer treatment, growth factors are widely utilized in tissue engineering, and insulin remains the primary treatment for diabetes[175]. Another advantage of protein-based therapeutic agents is their endogenous nature, providing them with enhanced biocompatibility and biodegradability over other molecules[176]. Moreover, the breakdown products of proteins can be naturally metabolized or eliminated by the body, reducing the risk of toxicity associated with treatment.

However, proteins are delicate macromolecules, prone to unfolding and enzymatic degradation, and typically have a short half-life compared to other reagents. Additionally, their limited membrane permeability restricts cellular uptake, leading to low treatment efficiency and the requirement of frequent dosing[174,176]. To address these limitations, recent advances have focused on developing protein delivery systems that can protect, transport, and release therapeutic

proteins at targeted sites without compromising their bioactivity. Among them, nanotechnology has emerged as a promising approach for protein delivery, especially in cancer treatment. Nanoparticles, typically ranging from 20 - 100 nm in size, tend to accumulate effectively in tumor tissues due to the enhanced permeability and retention (EPR) effect. This property allows nanoparticles carrying therapeutic proteins to concentrate around tumor cells, improving treatment efficacy while reducing systemic toxicity. These systems are engineered in a range of materials and sizes, with customizable shapes and physicochemical properties, including microparticles[177,178], nanoparticles[179,180], hydrogels[174,181,182], fibers[183], films[184], patches[185], and macroporous scaffolds[186].

The protein nanocapsule technology has been innovatively developed to encapsulate an individual protein by a polymer shell formed via in situ polymerization of monomers and crosslinkers[187]. The nanocapsules have successfully encapsulated various proteins[188], also including enzymes[189,190] and monoclonal antibodies[191], exhibiting improved stability and prolonged circulation time. By adjusting monomers and crosslinkers, and applying needed surface modifications, nanocapsules can fulfill the requirement for enzyme delivery in multiple conditions. In this study, poly(ethylene glycol) methyl ether acrylate (PEGMA), 2-(Dimethylamino)ethyl methacrylate (DMAEMA) were used as monomers, and bisacrylamide (BIS) was selected to be the crosslinker to form LOx nanocapsules. PEGMA could prolong the systematic circulation time of nanocapsules[192]. It is highly hydrophilic and flexible owing to its chain of oxygen atoms connected by ethylene groups. And DMAEMA was chosen because of its pH-responsive property, which can be utilized to target the acidic environment around tumor sites. BIS worked as the crosslinker to form the nanocapsule structure and protect the LOx inside. It is a non-degradable crosslinker, providing higher stability to nanocapsules. Since LOx can work without releasing from

the nanocapsule, the treatment efficacy of LOx nanocapsules will not be impacted by the non-degradable crosslinker.

3.2 Materials and methods.

3.2.1 Materials.

LOx was purchased from Toyobo Inc. Poly(ethylene glycol) methyl ether acrylate (PEGMA, average Mn = 480), 2 - (Dimethylamino) ethyl methacrylate (DMAEMA), N, N'-methylenebisacrylamide (BIS), ammonium persulfate (APS), N, N, N', N'-tetramethylethylenediamine (TEMED), sodium L-lactate, catalase (CAT) from bovine liver, and agarose were purchased from Sigma Aldrich. Q-Sepharose Fast Flow resin was purchased from GE HealthCare. PBS (10×) and 20,70-dichlorodihydrofluorescein diacetate (H2DCFDA) were purchased from Fisher Scientific. Dulbecco's modified Eagle's medium (DMEM), fetal bovine serum (FBS), penicillin/streptomycin (P/S), and all the other cell culture reagents were obtained from Fisher Scientific unless otherwise specified.

3.2.2 Instruments.

Images of cells were obtained with an IX73 inverted microscope (Olympus Life Science). Dynamic light scattering (DLS) studies and zeta potential of native LOx and n(LOx) were obtained by Zetasizer Nano instrument (Malvern Instruments Ltd., Kingdom). UV/vis absorbance was measured by NanoDrop One spectrophotometer (Thermo Fisher Scientific). The absorbance was measured with an iMark Microplate Absorbance Reader (Bio-Rad Laboratories). The fluorescence intensity was measured using Modulus Microplate Multimode Reader (Turner BioSystems). Cell numbers were acquired by manual counting with trypan blue dye exclusion under the microscope.

3.2.3 RNA isolation and RNA-seq.

The total RNA of SCC1 and SCC1R cells was extracted using TRIzol reagents. cDNA was generated using the reverse transcription reaction with 1 μg RNA, Random Hexamers, dNTP mix, and M-MuLV Reverse Transcriptase. RNA quality control, library construction, and sequencing were all performed by the Technology Center for Genomics & Bioinformatics (TCGB) core at UCLA, and libraries were sequenced on Illumina HiSeq 3000. Analysis of RNA-seq data was done as described before.[88,89] Briefly, RNA-seq FASTQ sequences were mapped to the human genome hg38 (GRCh38) by Hisat2 (v2.2.0). For the uniquely mapped reads, FeatureCounts from Subread2 (v2.0.3) were utilized to count the reads mapped to each gene. The differentially expressed genes (DEGs) were identified by Deseq2 (v1.32.0). GO term analysis was carried out for gene transcripts both upregulated and downregulated by at least 1.5-fold using a database for annotation, visualization, and integrated Discovery (DAVID) version 6.8. The volcano plot was produced through the Bioinformatics cloud platform (https://www.bioinformatics.com.cn/, an online platform for data analysis and visualization).

3.2.4 Synthesis of n(LOx).

LOx was dissolved in 1× PBS at a concentration of about 10 mg/ml and dialyzed overnight at 4°C to remove the residual inorganic salts. Subsequently, PEGMA (13,600:1, n/n, PEGMA: LOx), DMAEMA (2400:1, n/n, DMAEMA: LOx), and BIS (1600:1, n/n, BIS: LOx) were added to the LOx solution. The in situ polymerization was initiated with APS (1600:1, n/n, APS: LOx) and TEMED (2:1, w/w, TEMED: APS). The reaction mixture was kept at 4°C for 2 hours and dialyzed in Hepes buffer (25 mM, pH 7.5) overnight to remove the unreacted molecules. n(LOx) was purified with an anion exchange column (Q-Sepharose) using Hepes buffer (25 mM, pH 7.5) as the elution buffer.

3.2.5 Determination of protein concentration.

The concentration of n(LOx) was determined by bicinchoninic acid (BCA) colorimetric protein assay kits (Thermo Fisher Scientific). Briefly, native LOx was diluted to a series concentration of 1, 0.5, 0.25, 0.125, 0.0625 mg/ml. BCA reagent mixture was made by mixing reagent A and B at the ratio of Reagent A: Reagent B = 50: 1. Then, each of the standards and samples were mixed with BCA mixture and incubated at room temperature for 30 minutes. The absorbance at 562 nm was determined with a plate reader.

3.2.6 Hydrodynamic size measurements.

Dynamic light scattering (DLS), also known as photon correlation spectroscopy[193] or quasi-elastic light scattering[194], has emerged as a simple tabletop technique executable under ordinary lab environments to investigate the hydrodynamic size of nanoparticles. In this study, the hydrodynamic sizes of LOx and n(LOx) were measured with Zetasizer Nano instrument. Native LOx and purified nanocapsules were diluted in deionized water to a final concentration of 1 mg/ml and measured.

3.2.7 Zeta-potential measurements.

Zeta-potential has evolved into a popular tool to measure the surface charges of nanoparticles within the pharmacy community, mainly because this integrated, compact, and affordable technique is non-invasive, requires minimal sample preparation, and no pre-experimental calibration[195]. Zeta-potential was measured with Zetasizer Nano instrument. Native LOx and purified nanocapsules were diluted in deionized water to a final concentration of 0.5 mg/ml and measured three times for each group.

3.2.8 Cell culture.

Human peripheral blood mononuclear cells (PBMCs) were purchased from the UCLA/CFAR Virology Core Laboratory and used on the same day of receiving. Human HNSCC cell line SCC1 was from the University of Michigan and maintained in DMEM containing 10% FBS and 1% penicillin-streptomycin. The mouse MOC1 cell line was kindly provided by Dr. Gutkind at The University of California, San Diego, and maintained in DMEM containing 10% FBS and 1% penicillin-streptomycin. The cisplatin-resistant MOC1R and SCC1R cell lines were established by chronic culture in the gradually increased concentration of cisplatin and maintained in the same medium with the addition of 5 μg/ml cisplatin. All these cells were maintained at 37 °C in 5% CO2 atmosphere.

3.2.9 Measurement of lactate removal by LOx samples in the cell culture media.

MOC1, MOC1R, SCC1, and SCC1R cells were seeded in 96-well plates at 5000 cells per well. The culture media of these cells were collected daily for 4 days. The concentration of lactate was determined using the Lactate Colorimetric/Fluorometric Assay Kit (BioVision, Cat#K607-100) following the user manual. Briefly, 5 μL culture medium from each sample was added to a 96-well plate and 45 μL/well Lactate Assay Buffer was added to get a final volume of 50 μL. Meantime, standard curve samples were prepared by diluting the Lactate Standard with Lactate Assay Buffer to generate 0, 2, 4, 6, 8 & 10 nmol/well lactate standard. Then 50 μL Reaction Mix containing 46 μL Lactate Assay Buffer 46 μL, 2 μL Lactate Enzyme Mix, and 2 μL Lactate Probe was added into each sample including standards. After 30 minutes of incubation at room temperature, protected from light, absorbance at 570 nm was read in a microplate reader. After subtracting the 0 standard reading from all readings, the lactate standard curve was plotted, and

the lactate concentration in each sample was calculated by reads from the standard curve timing the dilution factor 10.

To measure the lactate accumulation in the culture media of HNSCC cells, MOC1, MOC1R, SCC1, and SCC1R cells were seeded in 96-well plates at 5000 cells per well. Samples of the culture media were collected daily for 4 days, and the concentration of lactate was determined using the method described above. For detecting the removal by LOx samples, MOC1, MOC1R, SCC1, and SCC1R cells were seeded in 96-well plates at 5000 cells per well. After 3 days, LOx samples (10 μg/ml) were added to the media. Samples from the mixture were collected every 20 min for 1 hour, and the concentration of lactate was determined.

3.2.10 Detection of H_2O_2.

H_2O_2 generation in the cell culture media was detected by H2DCFDA, which can be converted to the highly fluorescent 20,70-dichlorofluorescein (DCF) upon oxidation by H_2O_2. MOC1, MOC1R, SCC1, and SCC1R cells were seeded at 5000 cells per well and cultured for 3 days. H2DCFDA (5 μM) was added to the culture media. After incubation with the cells for 30 minutes, LOx samples at different concentrations (0, 0.25, 0.5, 1, and 2 μg/ml) were added. The fluorescent signals of DCF (excitation, 485 nm; emission, 535 nm) at 30 minutes were measured with a plate reader.

3.2.11 Determination of the reactivity between nanocapsules and cells.

Bovine serum albumin (BSA) conjugated with PE fluorescent was used as a model protein. Using the same formulation and synthesis steps with n(LOx), n(BSA) was successfully encapsulated. Native BSA and n(BSA) were separately co-cultured with SCC1 cells in the presence of different lactate levels (0, 5 mM, 10 mM, and 15 mM). After a 4-hour co-culturing,

SCC1 cells were collected, washed to remove unreacted reagents, and tested with flow cytometry using the PE channel.

3.2.12 Cell viability.

The CCK8 assay (ApexBio, K1018) was used to assess cell viability following the product manual. Briefly, cells were seeded in 96-well plates at an appropriate density (10,000 cells/well for MOC1R, and 8,000 cells/well for SCC1R) and allowed to adhere overnight. The following day, various n(LOx) concentrations (0, 1, 2.5, 5, 10 ng/mL) were applied to the cells. After the designated incubation period, the original medium was removed and 100 µL 10x diluted CCK-8 reagent was added to each well. The absorbance of each well was measured at 450 nm using a microplate reader after another 2-hour incubation. The results were then analyzed to determine the effects of treatments on cell viability.

3.2.13 Cell migration.

Culture-Insert 4 well (ibidi, 80469) was used for cell migration essay. This insert could create physical gaps within a cell monolayer. By monitoring the process of the gap closure at different time points, we could get the information for cell migration. To begin with, the inserts were placed in 12-well plates. Cells were treated with PBS or 10 ng/mL n(LOx) + 5 µg/mL CAT for 24 hours before preparing the cell suspension with a concentration of 2×10^5 cells/well. 110 µl cell suspension was added into each insert well. The outer area was filled with 300 µl culture medium. Then the plates were incubated for 24 hours at 37°C and 5% CO2 as usual for appropriate cell attachment. After the Culture-Insert 4 Well was gently removed using sterile tweezers to create gaps, the wells were filled with 1 ml cell culture medium with PBS, n(LOx) + CAT. Pictures of the gaps were taken at 0 hours, 12 hours, and 24 hours to monitor the gap closure.

3.2.14 Cell invasion.

The transwell assay was used to assess cell invasion. BioCoat Matrigel® Invasion Chambers (Corning, 354480) were used following the product manual. Briefly, cells were first treated with PBS or 10 ng/mL n(LOx) + 5 μg/mL CAT for 8 hours. Then 1×10^5 cells in the culture medium without serum were placed in the upper chamber of each transwell insert. The lower chamber contains 15% serum to stimulate cell movement. After 48-hour incubation, cells that have invaded through the membrane are fixed with 70% ethanol for 30 minutes, stained with 2% crystal violet for 15 minutes, washed with DI water 3 times, dried overnight, and counted under the optical microscope.

3.2.15 PBMC studies.

To analyze the IFN-γ and IL-2 production by T cells, SCC1 and SCC1R cells were seeded in a six-well plate at 1×10^5 cells per well and cultured for 3 days, and then incubated with n(LOx) samples (2 μg/ml) for 24 hours. For the n(LOx)&CAT group, 5 μg/ml CAT was added to remove H_2O_2. 1×10^6 PBMCs were added in each well and incubated with the n(LOx)-treated SCC1 and SCC1R cells for 4 hours. The IFN-γ/IL-2 production was then analyzed with flow cytometry.

3.2.16 Animal model setup and progression monitoring in vivo.

All animals were treated in accordance with the Guide for Care and Use of Laboratory Animals under the protocol approved by the UCLA Chancellor's Animal Research Committee (Institutional Animal Care and Use Committee). Female NU/J mice were purchased from the Jackson Laboratory. All animals were maintained at a pathogen-free facility at UCLA.

SCC1R cells (2×10^6 cells/mouse) were resuspended in sterilized PBS and mixed with Matrigel at a volume ratio of 1:1. The mixture was injected subcutaneously into the flank of 6-

week-old NU/J mice to generate human xenograft mouse model. After the average tumor size increased to 150 mm^3, mice were randomly divided into three groups and intratumorally given the 1) PBS control, 2) native LOx at the dosages of 0.5mg/kg mouse body weight, and 3) n(LOx) at the dosage of 0.5mg/kg mouse body weight. The body weight of mice and the tumor size were monitored every three days. After the largest tumor dimension reached 1.5 cm, mice were sacrificed. Tumors were measured and weighed. The equation used in this study to calculate the tumor size is as follows:

$$Tumor\ size = \frac{1}{2} \times length \times width \times width$$

3.2.17 Statistics.

Data are presented as means ± S.D. unless otherwise indicated. Statistical significance was calculated using GraphPad Prism. All the comparisons of significance between groups were calculated by two-tailed unpaired t-test.

3.3 Results.

3.3.1 Cisplatin-resistant HNSCC cells had similar lactate levels with cisplatin-sensitive HNSCC cells.

To verify the availability of the design, we first investigated the lactate level of SCC1 and cisplatin-resistant SCC1R cells. RNA sequencing (RNA-seq) was conducted to compare the metabolic profiles of cisplatin-resistant (SCC1R) and cisplatin-sensitive (SCC1) HNSCC cells. The RNA-seq analysis revealed no significant differences in the expression level of glycolysis-related genes between the two cell types, including EDN1, SLC16A1, ALDH9A1, HK2, PDHB, ADH5, PDHA1, PGK1, ALDH1B1, GAPDH, TPI1, LDHB, PCK2, ALDH1A3, ALDH3A2, GPI,

and PFKL **(Fig. 3-1)**. Gene Ontology (GO) analysis was employed to explore the role of cisplatin resistance in HNSCC cells. Examination of the upregulated genes in SCC1R cells showed the activation of several key cancer-related pathways, including the PI3K-Akt signaling pathway, MAPK signaling pathway, and Rap1 signaling pathway, all of which are crucial in cancer progression. However, glycolysis is not one of them, indicating that the metabolic activity is similar in SCC1R cells compared with SCC1 cells **(Fig. 3-2)**.

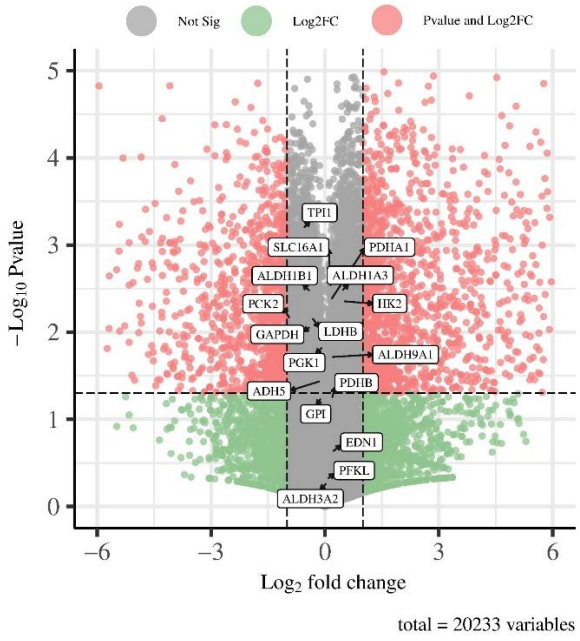

Fig. 3-1. Volcano plot of glycolysis-related genes in SCC1R cells compared with SCC1 cells.

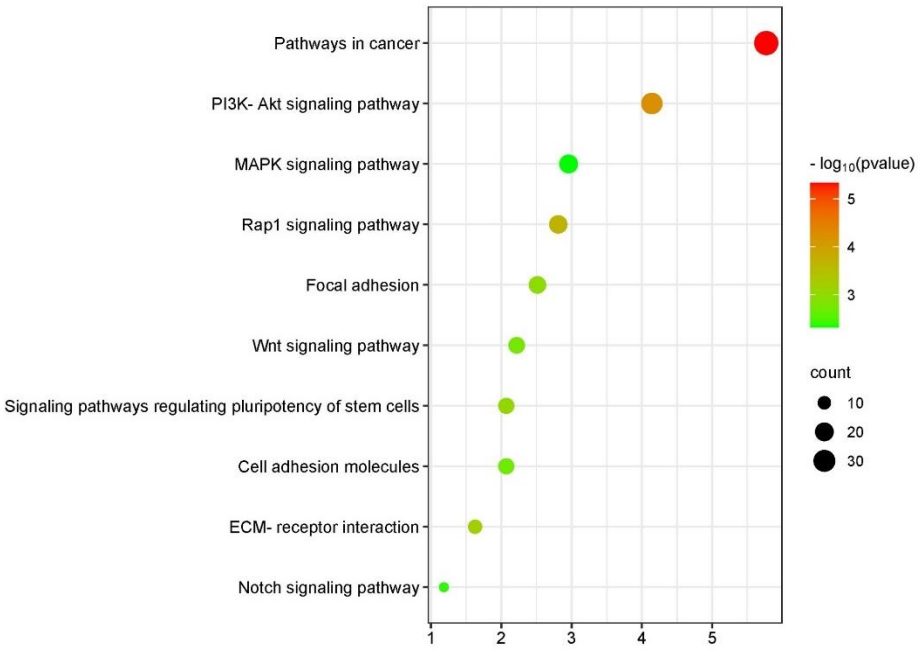

Fig. 3-2. Gene Ontology (GO) analysis of upregulated genes in SCC1R cells compared with SCC1 cells.

Consistent with the RNA-seq findings, the lactate production assay demonstrated comparable lactate production in both SCC1R and SCC1 cells **(Fig 3-3 a)**. After a 4-day culture, the lactate concentration in the culture medium was around 20mM. Similar results were also found in MOC1R and MOC1 cells **(Fig 3-3 b)**. 30 mM of lactate was detected in the culture medium of both cell types after a 4-day culture. These results indicate that despite their resistance to cisplatin, the metabolic characteristics, particularly lactate production, remain largely unchanged in cisplatin-resistant HNSCC cells, thus the higher lactate level within TME remained a potential treatment target with cisplatin-resistant HNSCC.

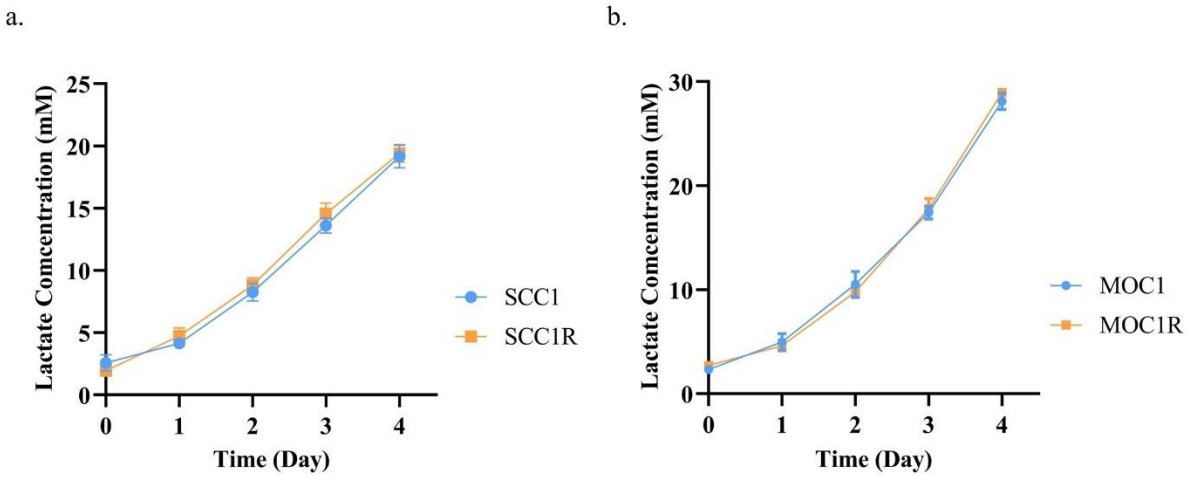

Fig. 3-3. Lactate accumulation of different cancer cell lines. The concentrations of lactate in the cell media of SCC1, SCC1R (a), MOC1, and MOC1R (b) were measured daily for four days (n=5).

3.3.2 Nanoencapsulation of lactate oxidase retained its enzymatic activity and promoted its interaction with cells in acidic environments.

Recombinant LOx from microorganisms has a short half-life and potential immunogenicity, inhibiting its application in clinical use. To circumvent this limitation, native LOx was encapsulated using the single-enzyme encapsulating platform, where individual proteins can be encapsulated within a thin polymer shell via in situ polymerization of monomers together with stimuli-responsive crosslinkers[196–198]. The encapsulation of LOx involves the enrichment of poly(ethylene glycol) methyl ether acrylate (PEGMA; monomer), 2-(Dimethylamino)ethyl methacrylate (DMAEMA; monomer), and bisacrylamide (BIS; cross-linker) around LOx molecules through noncovalent interactions and subsequent growth of a thin polymer shell around each LOx molecule by in situ polymerization initiated by ammonium persulfate (APS) and N, N, N', N'-Tetramethyl ethylenediamine (TEMED) **(Fig. 3-4)**. The encapsulation process leads to the

formation of LOx nanocapsules, denoted hereinafter as n(LOx). For the monomer selection, PEGMA was used to prolong the systematic circulation time of nanocapsules[192]. Its chain of oxygen atoms connected by ethylene groups makes it highly hydrophilic and flexible. And DMAEMA was chosen because of its pH-responsive property, which can be utilized to target the acidic environment around tumor sites.

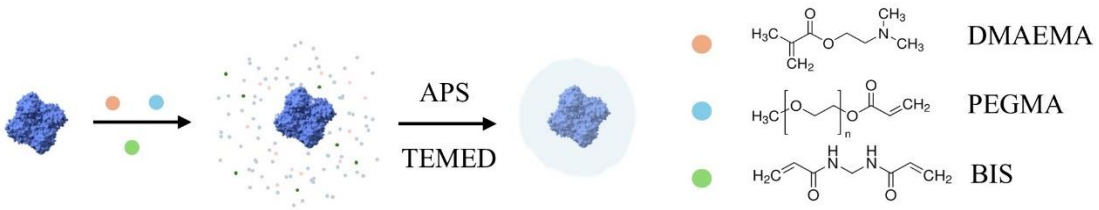

Fig. 3-4. Encapsulation process of n(LOx) for HNSCC therapy. Lactate oxidase (LOx) was encapsulated to form nanocapsules using a two-step reaction: enrichment of monomers and crosslinkers around LOx molecules, and in situ polymerization to form a polymer shell that encapsulated the LOx and formed n(LOx).

Using the dynamic light scattering, the hydrodynamic sizes of native LOx and encapsulated n(LOx). Compared with native LOx with an average size of about 8 nm, n(LOx) showed a spherical morphology with an average size of roughly 18 nm, indicating the successful encapsulation of LOx **(Fig. 3-5 a)**. Zeta potential measurement further confirmed the encapsulation of LOx **(Fig. 3-5 b)**. The encapsulation changed the negative charge of native LOx (−8 mV) to a near-neutral zeta potential for n(LOx) (+1 mV).

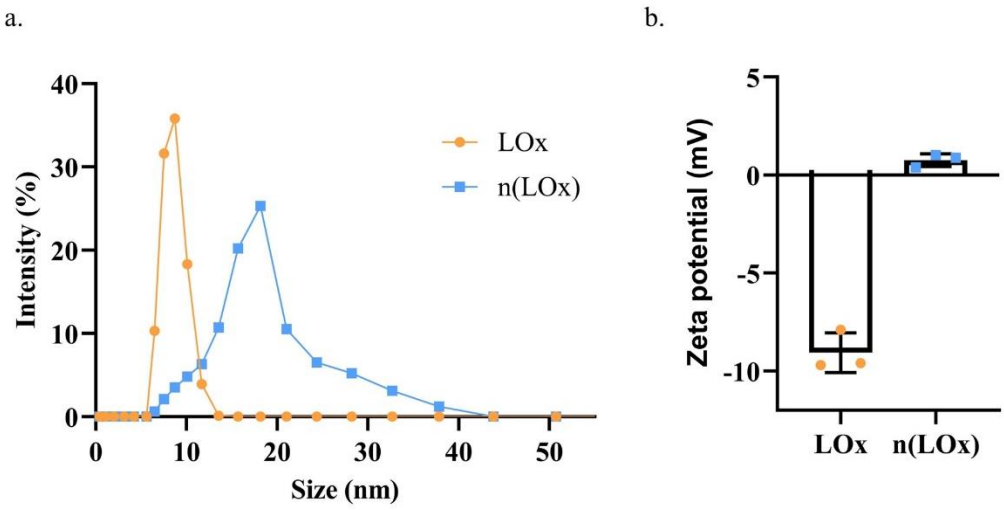

Fig. 3-5. Characterizations of n(LOx). a, Dynamic light scattering showing the particle size distribution of native LOx and the encapsulated n(LOx). **b**, Zeta potential of native LOx and n(LOx).

The ability of n(LOx) to reduce lactate concentrations was first examined using both cisplatin-sensitive and cisplatin-resistant cell lines, including SCC1 and SCC1R, which abundantly produced lactate in the culture media **(Fig. 3-6 a)**. Specifically, adding native LOx or n(LOx) (10 μg/ml) to SCC1 cell cultures reduced the lactate concentration in the culture media from 15 to 7mM in 1 hour, while lactate concentration in the culture medium with phosphate-buffered saline (PBS) stayed unchanged. And there was no significant difference between the LOx and n(LOx) groups, suggesting that the encapsulation of LOx didn't have an impact on its enzyme activity. Meanwhile, in the presence of H2DCFDA (a fluorescent probe for H_2O_2), the cancer cells treated with native LOx or n(LOx) exhibited substantially higher fluorescent signals than PBS controls, indicating increased concentrations of H_2O_2 **(Fig. 3-6 b)**. Consistent results were also obtained in cisplatin-resistant SCC1R cells **(Fig. 3-7)**, confirming the ability of n(LOx) to reduce lactate and generate H_2O_2 in cisplatin-resistant HNSCC cells.

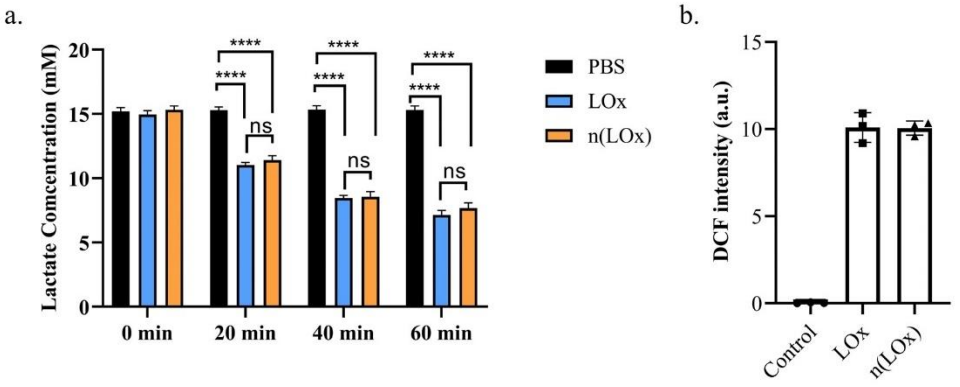

Fig. 3-6. n(LOx) retains the enzyme activity of LOx in SCC1 cells. a, Lactate concentration in the culture medium of SCC1 cells after incubating with PBS control, native LOx or n(LOx) (n = 3). **b**, H_2O_2 generation in the culture medium of SCC1 cells after incubating with PBS, native LOx or n(LOx) (0.25 μg/ml) for 30 min (n = 3). a.u., arbitrary units. H2DCFDA is used as an indicator of H_2O_2, which can be oxidized by H_2O_2 to produce highly fluorescent 20,70-dichlorofluorescein (DCF). The fluorescence intensity of oxidized H2DCFDA (DCF) was used to evaluate the generation of H_2O_2. **** $p < 0.001$, ns: not significant.

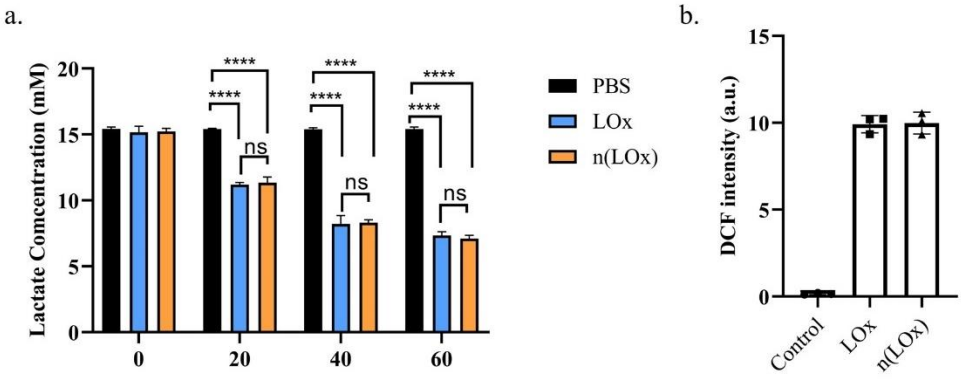

Fig. 3-7. n(LOx) retains the enzyme activity of LOx in SCC1R cells. a, Lactate concentration in the culture medium of SCC1R cells after incubating with PBS control, native LOx or n(LOx) (n = 3). **b**, H2O2 generation in the culture medium of SCC1R cells after incubating with PBS,

native LOx or n(LOx) (0.25 μg/ml) for 30 min (n = 3). a.u., arbitrary units. **** $p < 0.001$, ns: not significant.

The addition of DMAEMA as a monomer was aimed to provide the targeting ability of the nanocapsules and increase the accumulation of nanocapsules at the tumor site, where the lactate level was higher than normal tissues termed the Warburg effect. After polymerization, poly(2-dimethylamino)ethyl methacrylate (PDMAEMA) becomes a weak poly-base with a pKa value between 6.5 and 7[199]. Compared to the physiological pH of 7.4, in the tumor environment where the pH is around 6.4 to 7[200,201], nanocapsules containing DMEAME will be more positively charged, thus they will have a stronger interaction with the negatively charged tumor cells. In vitro experiments with SCC1 cells showed that encapsulation of LOx significantly promoted the material-cell interaction **(Fig. 3-8)**. As the lactate level in the environment increased, more nanocapsules were attached to the cells, indicating a more intensive interaction with cells.

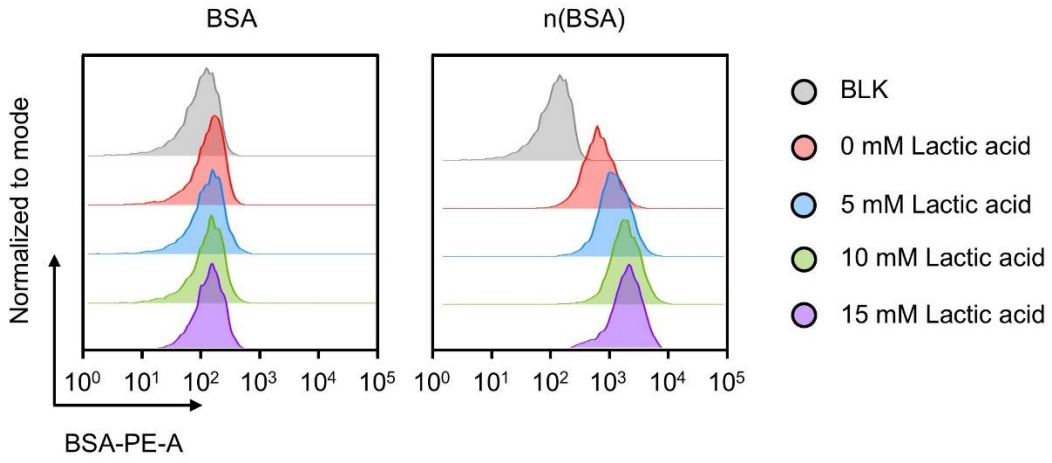

Fig. 3-8. n(BSA) presented high reactivity with the cell surface in acidic environment. Bovine serum albumin (BSA) was conjugated with phycoerythrin (PE) for flow cytometry. No BSA or n(BSA) samples were added to the blank control group (BLK).

3.3.3 Lactate oxidase nanocapsules reduced cell viability, migration, and invasion.

Cisplatin-resistant cell lines MOC1R and SCC1R were utilized to investigate the anti-cancer efficacy of n(LOx). MOC1 cells were seeded and treated with different n(LOx) concentrations from 1 ng/mL to 100 ng/mL. It was found that n(LOx) could significantly reduce MOC1R cell numbers **(Fig. 3-9 a)**. Although a low n(LOx) concentration of 1 ng/mL only led to about 18% of cell death after 24 hours, a moderate concentration of 2.5 ng/mL caused the death of 50% of MOC1R cells after just 4 hours. With higher n(LOx) concentration, the cell viability decreased to only 10% 4 hours after the treatment. And after 8 hours, no live cells were detected in those high n(LOx) groups. One thing to notice was that the high concentration groups, specifically 5 ng/mL, 10 ng/mL, and 100 ng/mL, had comparable impacts on cell viability, showing that n(LOx) could have reached its maximum therapeutic efficiency on MOC1R cells at the concentration of 5 ng/mL. Similar results were also found with SCC1R cells **(Fig. 3-9 b)**, indicating that the ROS produced by n(LOx) could lead to a drop in cell viability. One day after the co-culture, 1 ng/mL n(LOx) decreased cell viability to 90% while cell viability reduced to 60% with 2.5 ng/mL n(LOx). With a n(LOx) concentration higher than 5 ng/mL, the cell viability was close to zero.

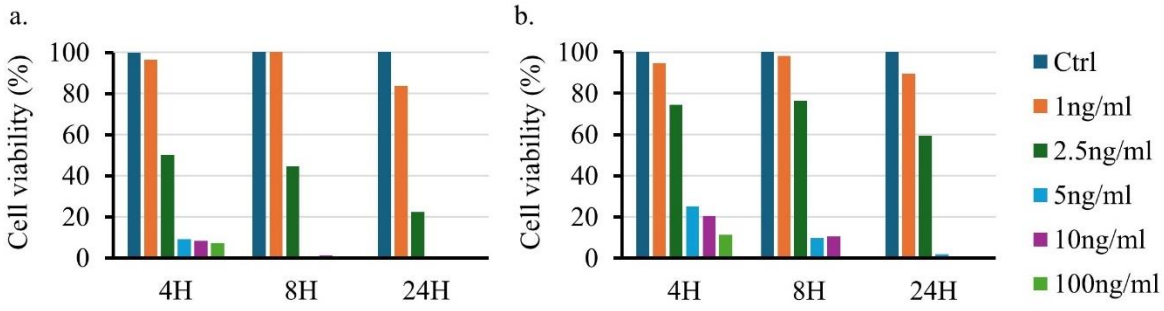

Fig. 3-9. Cell viability changes of MOC1R (a) and SCC1R (b) under various n(LOx) treatments. The viability was tested 4 hours, 8 hours, and 24 hours after treatment. The concentration of n(LOx) indicated the final concentration in the culture media.

We further addressed the therapeutic efficacy of n(LOx) on cisplatin-resistant cells through the scratch experiment and the transwell experiment. To exclude the impact of cell death on those experiments, catalase (CAT), an enzyme that effectively decomposes H_2O_2 into H_2O and O_2, was used alongside n(LOx) as n(LOx)/CAT to only retain lactate reduction by removing H_2O_2 produced by n(LOx). **Fig. 3-10 a** showed that the removal of lactate from the culture medium by n(LOx) reduced MOC1R cell migration. The recovery rate after 8h was significantly decreased from 80% in the control group to 50% in the n(LOx) + CAT treatment group **(Fig. 3-10 b)**. n(LOx) displayed a similar impact on the migration of SCC1R cells **(Fig. 3-11 a)**. The treatment of n(LOx) significantly inhibited the recovery of the scratch from 75% to 40% **(Fig. 3-11 b)**.

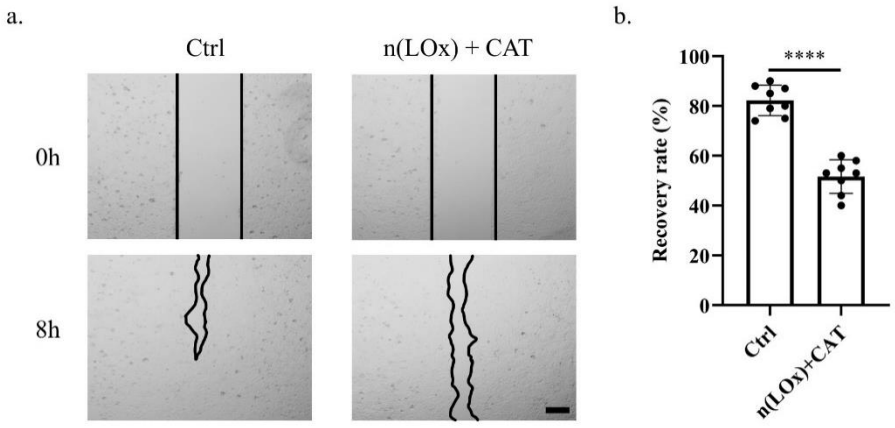

Fig. 3-10. n(LOx) inhibited MOC1R cell migration. a, optical microscope images for MOC1R cell 8h migration with n(LOx) + CAT. Scale bar: 100μm. **b**, statistical analysis of MOC1R cell migration. **** $p<0.001$.

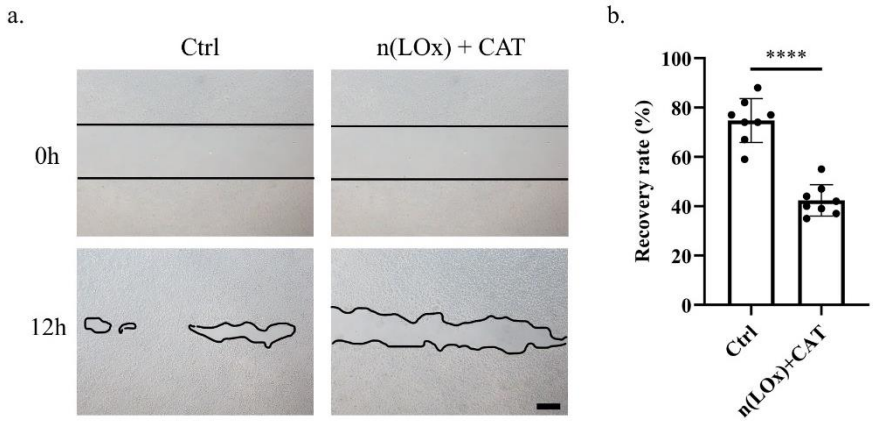

Fig. 3-11. n(LOx) inhibited SCC1R cell migration. a, optical microscope images for SCC1R cell 12h migration with n(LOx) + CAT. Scale bar: 100μm. **b**, statistical analysis of SCC1R cell migration. **** $p<0.001$.

Fig. 3-12 a illustrated that lactate removal from the culture medium by n(LOx) led to a reduction in MOC1R cell invasion. In the n(LOx) + CAT treatment group, the cells migrating through the ECM mimic Matrigel significantly decreased to about 40% of the control group after 4 hours of treatment **(Fig. 3-12 b)**. A similar effect of n(LOx) was observed on SCC1R cell migration **(Fig. 3-13 a)**, where treatment with n(LOx) reduced the invasion cells to 30% **(Fig. 3-13 b)**. Since the H_2O_2 produced by n(LOx) was decomposed into H_2O and O_2 with CAT, the decrease in the cisplatin-resistant HNSCC cell migration and invasion was only caused by reducing the lactate level in the culture media.

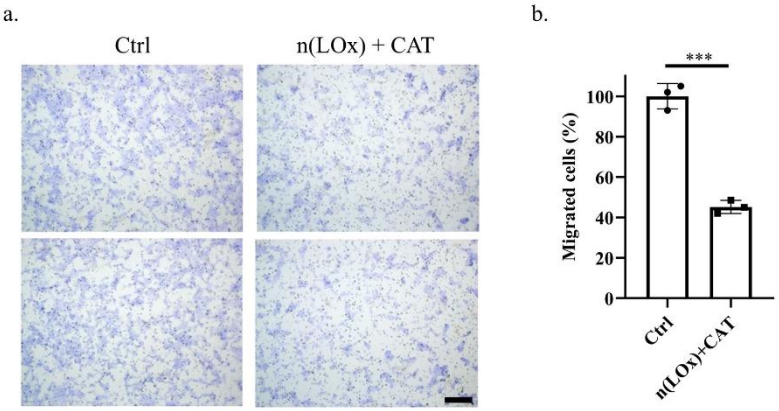

Fig. 3-12. n(LOx) inhibited MOC1R cell invasion. a, optical microscope images for MOC1R cell invasion with n(LOx) + CAT. Scale bar: 100μm. **b**, statistical analysis of MOC1R cell invasion. *** $p<0.01$.

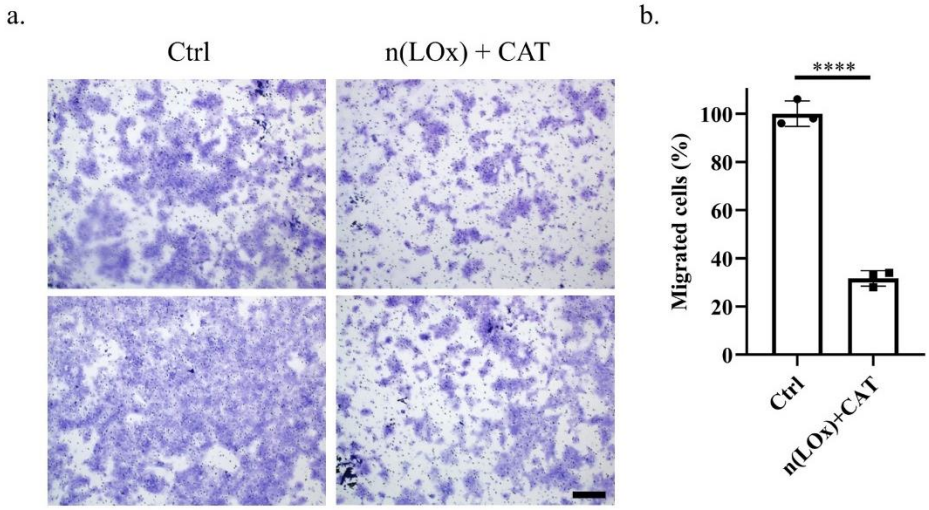

Fig. 3-13. n(LOx) inhibited SCC1R cell invasion. a, optical microscope images for SCC1R cell invasion with n(LOx) + CAT. Scale bar: 100μm. **b**, statistical analysis of SCC1R cell invasion. **** $p<0.001$.

3.3.4 Lactate oxidase nanocapsules activated T cells for cytokine production.

The ability of n(LOx) to increase the population of cytokine-producing T cells was examined in PBMC/SCC1 cocultures, where SCC1 cells were first treated with n(LOx) or n(LOx)/CAT for 24 hours followed by coculturing with PBMC for 4 hours. The culture medium with n(LOx) showed higher populations of IFN-γ-producing $CD4^+$ T cells (about 17.6%), IFN-γ-producing $CD8^+$ T cells (about 9.2%), interleukin-2 (IL-2)–producing $CD4^+$ T cells (about 12.7%), and IL-2-producing $CD8^+$ T cells (about 4.7%), whereas their populations in the n(LOx)/CAT group were similar to those of the controls with about 2.5% IFN-γ-producing $CD4^+$ T cells, 1.1% IFN-γ-producing $CD8^+$ T cells, 2.1% interleukin-2 (IL-2)–producing $CD4^+$ T cells, and 0.9% IL-2-producing $CD8^+$ T cells **(Fig. 3-14)**. Similar results were found with SCC1R cells. Both IFN-γ and interleukin-2 (IL-2)–producing $CD4^+$ and $CD8^+$ T cells were comparable in the n(LOx)/CAT and control groups, in contrast the n(LOx) group showed markedly higher populations of those cells **(Fig.3-15)**.

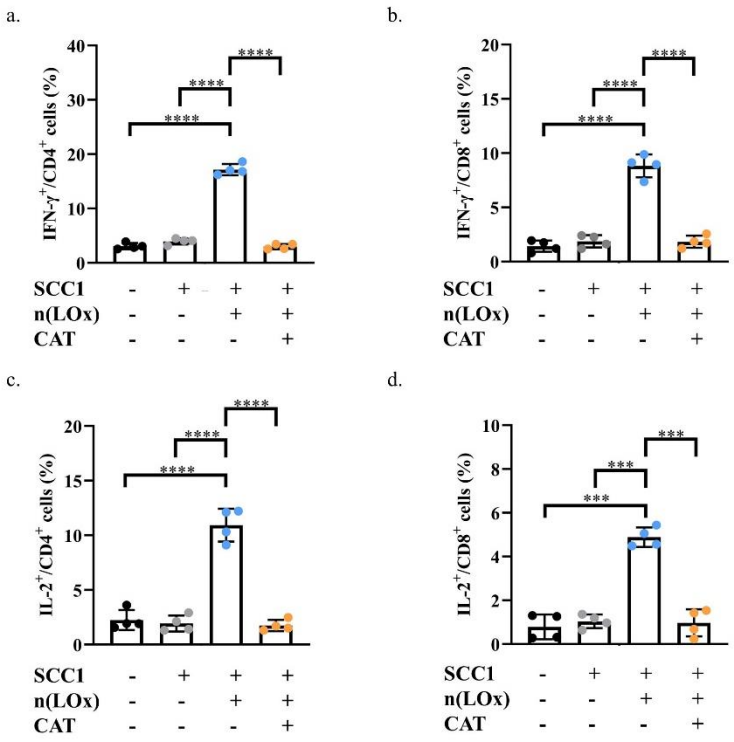

Fig. 3-14. n(LOx) promoted cytokine production by T cells co-cultured with SCC1 cells. a-b, Percentages of IFN-γ–producing $CD4^+$ (a) and $CD8^+$ (b) T cells after incubating with SCC1 cells treated with n(LOx) in the presence or absence of CAT (n = 4). **c-d**, Percentages of IL-2–producing $CD4^+$ (c) and $CD8^+$ (d) T cells after incubating with SCC1 cells treated with n(LOx) in the presence or absence of CAT (n = 4). ***$p < 0.01$ and **** $p<0.001$.

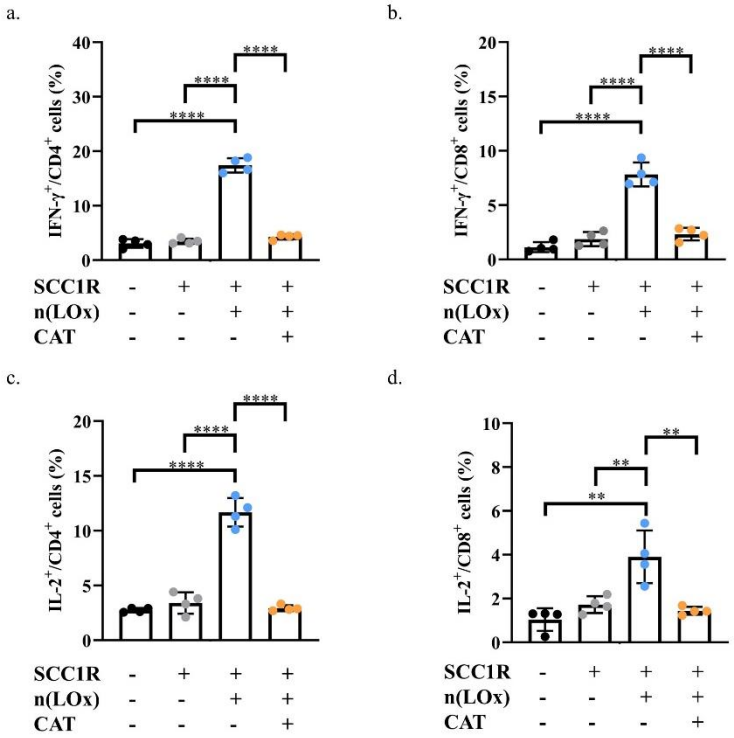

Fig. 3-15. n(LOx) promoted cytokine production by T cells co-cultured with SCC1R cells. a-b, Percentages of IFN-γ–producing $CD4^+$ (a) and $CD8^+$ (b) T cells after incubating with SCC1R cells treated with n(LOx) in the presence or absence of CAT (n = 4). **c-d**, Percentages of IL-2–producing $CD4^+$ (c) and $CD8^+$ (d) T cells after incubating with SCC1R cells treated with n(LOx) in the presence or absence of CAT (n = 4). **p < 0.05 and **** p<0.001.

3.3.5 Lactate oxidase nanocapsules suppress cisplatin-resistant tumor progression.

Cell line-derived xenograft models, created by implanting cancer cell lines into immunocompromised mice, offer a tumor microenvironment that more closely mimics the physiological and pathological conditions of human cancers. In this study, a cisplatin-resistant HNSCC model was developed in NU/J mice to assess the effectiveness of n(LOx) in vivo. SCC1R cells (2 million cells per mouse) were injected subcutaneously into the flanks of 6-week-old NU/J mice and the tumor growth was monitored **(Fig. 3-16 a)**. Once tumors reached an average volume

of 100 mm^3, the mice were randomly assigned to three treatment groups and given different treatments: (1) PBS control, (2) native LOx, and (3) n(LOx) at the dosage of 0.5mg/kg. Tumor size was monitored twice a week **(Fig. 3-16 b)**. The application of n(LOx) led to a reduction in tumor growth rate and tumor size, whereas there was no significant difference observed between the PBS control group and the native LOx treatment group. Images of dissected tumors **(Fig. 3-16 c)** revealed visibly smaller tumors in the n(LOx) treatment group compared to both the PBS control group and the native LOx treatment group. Tumor weights were also recorded, with n(LOx) reducing tumor weight to approximately half of the control group **(Fig. 3-16 d)**, demonstrating that n(LOx) effectively suppressed cisplatin-resistant tumors. The systemic toxicity was addressed by monitoring the body weight change in three groups. No significant change was observed in the mouse body weight among the PBS group, native LOx group, and n(LOx) treatment group throughout the animal experiment **(Fig. 3-17)**. In addition, during the dissection, no significant pathophysiological changes were found in the major organs, including the heart, liver, spleen, lungs, kidneys, and brain.

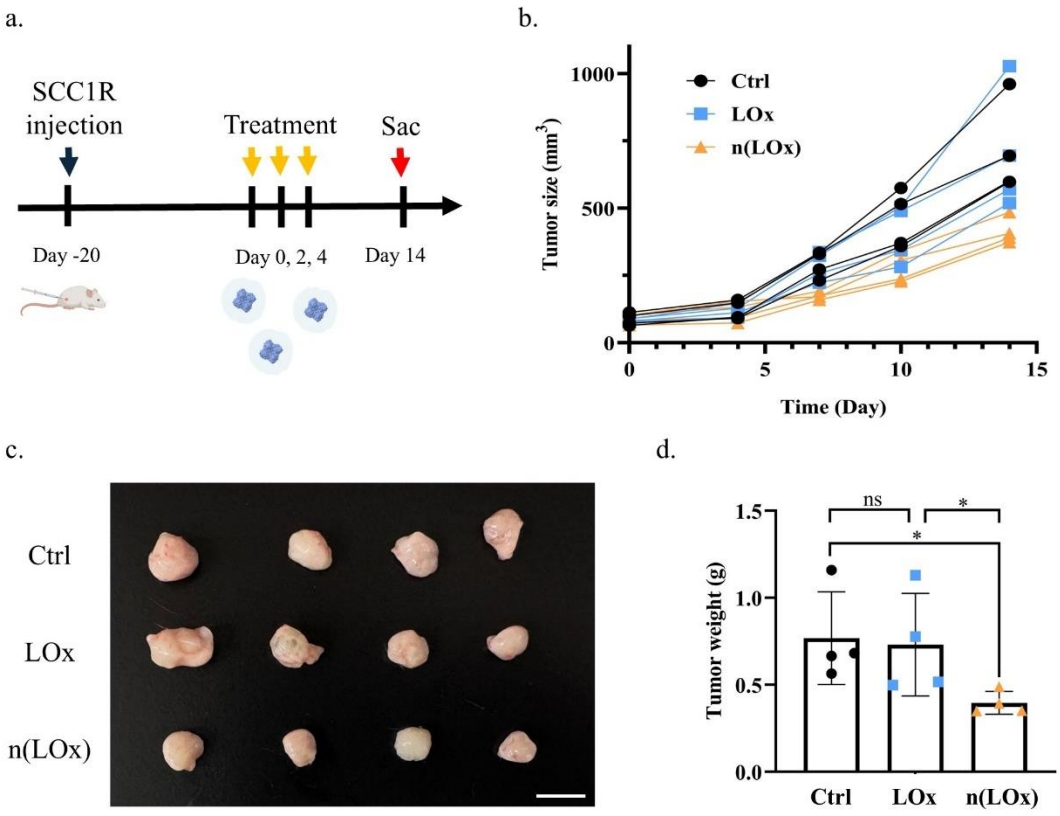

Fig. 3-16. Treatment efficacy of n(LOx) on cisplatin-resistant HNSCC model. a, the timeline of the animal experiment. **b**, tumor growth in PBS control group (Ctrl), native LOx group (LOx), and n(LOx) treatment group (n(LOx)). The tumor volume was monitored, measured, and calculated twice a week. **c**, pictures of tumors in the PBS control group (Ctrl), native LOx group (LOx), and n(LOx) treatment group (n(LOx)) 14 days after treatment. Scale bar, 1 cm. **d**, statistical analysis of the tumor weight in the PBS control group (Ctrl), native LOx group (LOx), and n(LOx) treatment group (n(LOx)) 14 days after treatment. * $p<0.01$, ns: not significant.

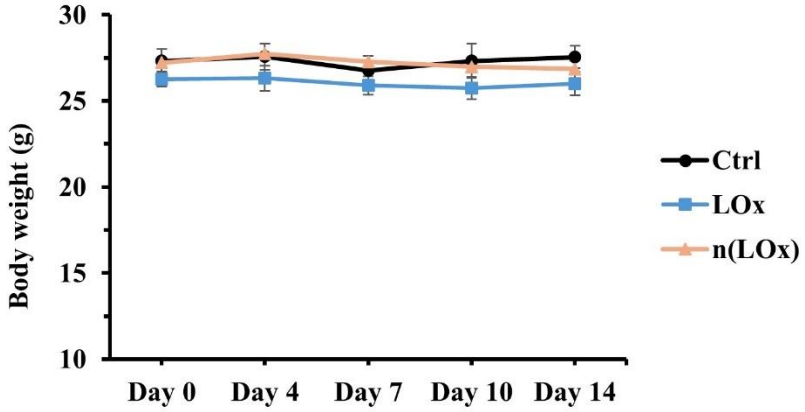

Fig. 3-17. Mouse body weight changes in the PBS control group (Ctrl), native LOx group, and n(LOx) treatment group during the experiment.

3.4 Conclusion and discussion.

The present study demonstrates that lactate oxidase encapsulated in nanoparticles, n(LOx), effectively targets the upregulated lactate level of HNSCC. When n(LOx) is introduced into cancer cells, it could convert excess lactate into pyruvate and H_2O_2, leading to a dual effect: reducing lactate accumulation and generating H_2O_2, which induces oxidative stress. The encapsulation didn't influence the structure and function of LOx. In vitro experiments proved that adding n(LOx) could convert the lactate in culture media into H_2O_2, leading to cell death, with a similar efficiency to native LOx. Besides, the use of the pH-responsive monomer DMAEMA equipped n(LOx) with stronger interaction with cells at lower pH, demonstrating the potential to target tumor sites, where the pH is lower due to the lactate accumulation.

In addition to affecting cell viability, n(LOx) also inhibited cancer cell migration and invasion. Metastasis describes the spread of cancer cells from the primary tumor to distant sites in the body. It remains a leading cause of cancer-related deaths and a major contributor to poor prognosis in HNSCC. Migration and invasion of cancer cells are critical for metastasis, and lactate

plays a key role in promoting cell migration and invasion by activating signaling pathways that drive epithelial-to-mesenchymal transition (EMT). By reducing lactate levels, n(LOx) decreased the migratory and invasive capabilities of both cisplatin-sensitive and cisplatin-resistant HNSCC cells, overcoming the challenge where traditional therapies often fall short.

Cytokines such as IFN-γ and IL-2 have been studied for their potential to promote T cell infiltration and activation within tumors. However, current approaches are limited by their ability to avert the immunosuppressive effects associated with excessive lactate production in the tumors. In contrast, our enzyme-based approach employs LOx not only removed lactate, but also released immunostimulatory agents.

Furthermore, the sustained reduction in tumor growth observed with n(LOx) treatment supports its potential for long-term therapeutic applications. Given the cytotoxic role of H_2O_2 generated through lactate oxidation, n(LOx) created an unfavorable environment for cancer cells that are otherwise well-adapted to hypoxic, lactate-rich conditions. This approach of leveraging lactate metabolism for therapeutic gains aligns with the growing interest in targeting metabolic pathways as an adjunct or alternative to conventional therapies. Additionally, as LOx works as the catalyst in the reaction, the nanocapsule system protects LOx from degradation and prolongs its half-life, offering a promising platform for sustained therapeutic efficacy, reduced need for frequent dosing, and potentially improved patient compliance and outcomes.

In conclusion, we have developed multifunctional LOx nanocapsules for cisplatin-sensitive and cisplatin-resistant HNSCC treatment, decreasing lactate concentrations while releasing immunostimulatory H_2O_2 in tumors. This dual-action approach reduced tumor cell viability, inhibited tumor cell migration and invasion, promoted the activation of effector T cells, and suppressed cisplatin-resistant HNSCC tumor growth in the mouse model. Future research should

further explore the biodistribution, optimal dosing, and combination potential of n(LOx) with existing chemotherapy or immunotherapy agents to expand its applicability and effectiveness in clinical settings. Besides, n(LOx) was intratumorally injected in this study. Due to its local recurrence pattern and frequent superficial extension, HNSCC presents an ideal scenario for intratumoral therapies[202]. However, considering the benefits of n(LOx) in activating antitumor T cell immunity, the therapeutic efficacy of n(LOx) should be demonstrated through systematic injection. In this case, controlling the H_2O_2 concentrations upon systematic injection of n(LOx) will be an essential issue, since excessively elevated concentrations of H_2O_2 in the blood may result in oxidative injuries. To address this problem, coadministration of CAT may be applied[203]. It is noted that nude mice used for the xenograft model had an inhibited immune system, which may reduce the treatment efficacy of n(LOx) because part of its function relied on the involvement of immune cells. Humanized mice with tumor xenograft, such as the PBMC humanized model can be a potential candidate to study immune cell activation and antitumor responses of immune cells with n(LOx)[204–206].

Chapter 4: Summarization and perspective.

Head and neck squamous cell carcinoma (HNSCC) ranked as the sixth most common cancer worldwide, representing a significant global health challenge, affecting countries at various levels of development. HNSCC constitutes a diverse category of cancer sites, encompassing the oral cavity, pharynx, larynx, nasal cavity, and paranasal sinuses. Over 60 % of HNSCC patients are initially diagnosed with advanced-stage disease, and the recurrence or metastasis rate is higher than 50%. Metastasis usually happens around the primary site, tumor bed, or regional lymph node, leading to oligometastatic disease. These features not only limit the feasibility of traditional

therapeutic methods including surgery, radiotherapy, and chemotherapy, but also lead to high mortality rates of HNSCC patients, with a 5-year overall survival of approximately one-third of the affected population.

The high incidence of chemoresistance, especially against cisplatin, makes the treatment of HNSCC even more challenging. Among the three most widely used therapeutic methods, surgery is commonly used for early-stage or primary tumor treatment where clear margins can be achieved and function is preserved. Radiation Therapy is usually employed for the treatment of locally advanced diseases. Platinum-based chemoradiation, mostly through cisplatin, remains the first option, or in some cases the only option for most HNSCC patients with locally advanced disease. Thus more and more studies have focused on conquering the cisplatin resistance in HNSCC.

To overcome the cisplatin resistance, we developed two novel strategies for HNSCC treatment. The first one utilized the extremely potent small molecule drug QCA570. Our findings showed that QCA570 significantly suppressed cell proliferation and invasion while promoting apoptosis in both cisplatin-sensitive and -resistant HNSCC cell lines in a dose-dependent manner. Moreover, QCA570 reduced the expression of critical cell survival proteins, including those in the BET family and c-Myc, affecting associated signaling pathways in cisplatin-resistant HNSCC. Combined with microneedle technology, the developed QCA570-based treatment could achieve effective, sustained, localized, and minimally invasive treatment of HNSCC with reduced systematic toxicity, significantly reducing the tumor growth in both the cisplatin-resistant xenograft mouse model and PDX mouse model.

Instead of focusing on the tumor cells, the second strategy paid attention to the tumor microenvironment, a highly organized network that plays active roles in tumor initial and

progression. Utilizing the high lactate level in TME caused by the Warburg effect, LOx nanocapsules were designed to achieve targeted and effective treatment for cisplatin-resistant HNSCC. By decreasing lactate levels and inducing oxidative stress through H_2O_2 production, n(LOx) effectively impaired cisplatin-resistant HNSCC cell viability, migration, and invasion. Intratumoral injection of n(LOx) efficiently suppressed cisplatin-resistant HNSCC tumor growth in a xenograft animal model, suggesting that n(LOx) could offer an innovative approach for overcoming cisplatin resistance in HNSCC.

Looking forward, both the QCA570 loaded microneedles and LOx nanocapsules have great potential for wider application with improved treatment efficacy. To begin with, although the working mechanisms to overcome cisplatin resistance are different, both strategies not only effectively reduced cisplatin-resistant HNSCC tumor growth, but also had therapeutic efficacy on cisplatin-sensitive HNSCC tumors, making them promising candidates for the treatment of both HNSCC types. Although intratumoral administration may limit their application, they can still be utilized for multiple cancer types including breast cancers, melanoma, and lymphoma, where intratumoral injection is routinely used for the clinical treatments[207]. Furthermore, cisplatin-induced DNA damage and cell death are linked to mitochondrial outer membrane permeabilization (MOMP) through several signaling pathways. BET inhibitors were reported to downregulate TP53, whose downstream gene products could facilitate MOMP[208,209], and ROS can directly trigger MOMP thus exacerbating cisplatin-induced DNA damage. Accordingly, both strategies developed in this study may help to restore cisplatin-sensitivity to a therapeutic useful level. And co-treatment with cisplatin is worth further exploring for possible synergistic effects. Finally, BET inhibitors could cooperate with PD-1 antibodies to facilitate antitumor response[210]. And it was found that removal of lactate from the TME increased the production of proinflammatory cytokines, and H_2O_2

could increase the infiltration and activation of effector T cells, providing the possibility of n(LOx)/PD-L1antibody co-therapy[190]. Therefore, we anticipate those developed strategies could be combined with other cancer immunotherapies to improve therapeutic efficacy and reduce therapeutic resistance.

Reference.

1. Siegel Mph, R. L. *et al.* Cancer statistics, 2023. *CA. Cancer J. Clin.* **73**, 17–48 (2023).
2. Johnson, D. E. *et al.* Head and neck squamous cell carcinoma. *Nat. Rev. Dis. Prim.* **6**, 1–22 (2020).
3. Marur, S. & Forastiere, A.A. Head and neck cancer: changing epidemiology, diagnosis, and treatment. *Mayo Clin. Proceedings* **83**,489-501 (2008).
4. Bray, F. *et al.* Global cancer statistics 2018: GLOBOCAN estimates of incidence and mortality worldwide for 36 cancers in 185 countries. *CA. Cancer J. Clin.* **68**, 394–424 (2018).
5. Ferlay, J. *et al.* Estimating the global cancer incidence and mortality in 2018: GLOBOCAN sources and methods. *Int. J. Cancer* **144**, 1941–1953 (2019).
6. Hashibe, M. *et al.* Alcohol drinking in never users of tobacco, cigarette smoking in never drinkers, and the risk of head and neck cancer: Pooled analysis in the International Head and Neck Cancer Epidemiology Consortium. *Journal of the National Cancer Institute* **99**, 777-789 (2007).
7. Jiang, H. *et al.* Can public health policies on alcohol and tobacco reduce a cancer epidemic? Australia's experience. *BMC Med.* **17**, (2019).
8. Mehanna, H. *et al.* Prevalence of human papillomavirus in oropharyngeal and

nonoropharyngeal head and neck cancer - Systematic review and meta-analysis of trends by time and region. *Head Neck* **35**, 747–755 (2013).

9. Marur, S. *et al*. HPV-associated head and neck cancer: A virus-related cancer epidemic. *The Lancet Oncology* **11**, 781–789 (2010).
10. Fakhry, C. *et al.* Improved survival of patients with human papillomavirus-positive head and neck squamous cell carcinoma in a prospective clinical trial. *J. Natl. Cancer Inst.* **100**, 261–269 (2008).
11. Windon, M. J. *et al.* Increasing prevalence of human papillomavirus–positive oropharyngeal cancers among older adults. *Cancer* **124**, 2993–2999 (2018).
12. Fung, S. Y. H. *et al.* Clinical utility of circulating Epstein-Barr virus DNA analysis for the management of nasopharyngeal carcinoma. *Chinese Clinical Oncology* 5, 18-18 (2016).
13. Marur, S. & Forastiere, A. A. Head and Neck Squamous Cell Carcinoma: Update on Epidemiology, Diagnosis, and Treatment. *Mayo Clin. Proc.* **91**, 386–396 (2016).
14. Pulte, D. & Brenner, H. Changes in Survival in Head and Neck Cancers in the Late 20th and Early 21st Century: A Period Analysis. *Oncologist* **15**, 994–1001 (2010).
15. Chaturvedi, A. K. *et al.* Human papillomavirus and rising oropharyngeal cancer incidence in the United States. *J. Clin. Oncol.* **29**, 4294–4301 (2011).
16. Osazuwa-Peters, N. *et al.* Suicide risk among cancer survivors: Head and neck versus other cancers. *Cancer* **124**, 4072–4079 (2018).
17. Pfister, D. *et al.* Head and neck cancers, version 2.2013. *Journal Natl. Compr. Cancer Network* **11**, 917-923 (2013)
18. Lee, N. C. J. *et al.* Patterns of failure in high-metastatic node number human papillomavirus-positive oropharyngeal carcinoma. *Oral Oncol.* **85**, 35–39 (2018).

19. Cohen, M. A., Weinstein, G. S., O'Malley, B. W., Feldman, M. & Quon, H. Transoral robotic surgery and human papillomavirus status: Oncologic results. *Head Neck* **33**, 573–580 (2011).

20. Weinstein, G. S. *et al.* Transoral robotic surgery: A multicenter study to assess feasibility, safety, and surgical margins. *Laryngoscope* **122**, 1701–1707 (2012).

21. Kofler, B. *et al.* New treatment strategies for HPV-positive head and neck cancer. *European Archives of Oto-Rhino-Laryngology* **271**, 1861–1867 (2014).

22. Forastiere, A. A. *et al.* Use of larynx-preservation strategies in the treatment of laryngeal cancer: American society of clinical oncology clinical practice guideline update. *Journal of Clinical Oncology* **36**, 1143–1169 (2018).

23. Langendijk, J. A. *et al.* Impact of late treatment-related toxicity on quality of life among patients with head and neck cancer treated with radiotherapy. *J. Clin. Oncol.* **26**, 3770–3776 (2008).

24. Lyhne, N. M. *et al.* The DAHANCA 6 randomized trial: Effect of 6 vs 5 weekly fractions of radiotherapy in patients with glottic squamous cell carcinoma. *Radiother. Oncol.* **117**, 91–98 (2015).

25. Bledsoe, T. J. *et al.* Hypofractionated Radiotherapy for Patients with Early-Stage Glottic Cancer: Patterns of Care and Survival. *J. Natl. Cancer Inst.* **109**, (2017).

26. Vlacich, G. *et al.* Dose to the inferior pharyngeal constrictor predicts prolonged gastrostomy tube dependence with concurrent intensity-modulated radiation therapy and chemotherapy for locally-advanced head and neck cancer. *Radiother. Oncol.* **110**, 435–440 (2014).

27. Bernier, J. *et al.* Postoperative Irradiation with or without Concomitant Chemotherapy for Locally Advanced Head and Neck Cancer. *N. Engl. J. Med.* **350**, 1945–1952 (2004).

28. Cooper, J. S. *et al.* Postoperative Concurrent Radiotherapy and Chemotherapy for High-Risk Squamous-Cell Carcinoma of the Head and Neck. *N. Engl. J. Med.* **350**, 1937–1944 (2004).

29. Galluzzi, L. *et al.* Molecular mechanisms of cisplatin resistance. *Oncogene* **31**, 1869–1883 (2012).

30. Peyrone, M. Ueber die Einwirkung des Ammoniaks auf Platinchlorür. *Justus Liebigs Ann. Chem.* **51**, 1–29 (1844).

31. Burchenal, J. H. *et al*. Rationale for development of platinum analogs. *Cancer Treat. Rep.* **63**, 1493–1498 (1979).

32. Kelland, L. The resurgence of platinum-based cancer chemotherapy. *Nature Reviews Cancer* **7**, 573–584 (2007).

33. Prestayko, A. *et al*. Cisplatin (cis-diamminedichloroplatinum II). *Cancer Treat. Rev.* **6**, 17-39 (1979).

34. Lebwohl, D. & Canetta, R. Clinical development of platinum complexes in cancer therapy: An historical perspective and an update. *European Journal of Cancer* **34**, 1522–1534 (1998).

35. Adelstein, D. J. *et al.* An intergroup phase III comparison of standard radiation therapy and two schedules of concurrent chemoradiotherapy in patients with unresectable squamous cell head and neck cancer. *J. Clin. Oncol.* **21**, 92–98 (2003).

36. Amable, L. Cisplatin resistance and opportunities for precision medicine. *Pharmacological Research* **106**, 27–36 (2016).

37. Cvitkovic, E. *et al*. Improvement of Cis-dichlorodiammineplatinum (NSC 119875): Therapeutic index in an animal model. *Cancer* **39**, 1357–1361 (1977).

38. Kelland, L. The resurgence of platinum-based cancer chemotherapy. *Nature Reviews Cancer* **7**, 573–584 (2007).

39. Giaccone, G. Clinical perspectives on platinum resistance. *Drugs* **59**, 9–17 (2000).

40. Köberle, B. *et al*. Cisplatin resistance: Preclinical findings and clinical implications. *Biochimica et Biophysica Acta - Reviews on Cancer* **1806**, 172–182 (2010).

41. Larsen, A. K., Escargueil, A. E. & Skladanowski, A. Resistance mechanisms associated with altered intracellular distribution of anticancer agents. in *Pharmacology and Therapeutics* **85**, 217–229 (2000).

42. Yamano, Y. *et al.* Identification of cisplatin-resistance related genes in head and neck squamous cell carcinoma. *Int. J. Cancer* **126**, 437–449 (2010).

43. Gottesman, M. M. Mechanisms of cancer drug resistance. *Annu. Rev. Med.* **53**, 615–627 (2002).

44. Harrap, K. R. Preclinical studies identifying carboplatin as a viable cisplatin alternative. *Cancer Treat. Rev.* **12**, 21–33 (1985).

45. Kidani, Y., Inagaki, K., Iigo, M., Hoshi, A. & Kuretani, K. Antitumor Activity of 1,2-Diaminocyclohexane-Platinum Complexes against Sarcoma-180 Ascites Form. *J. Med. Chem.* **21**, 1315–1318 (1978).

46. Raez, L. E., Kobina, S. & Santos, E. S. Oxaliplatin in first-line therapy for advanced non-small-cell lung cancer. *Clinical Lung Cancer* **11**, 18–24 (2010).

47. Choy, H. Satraplatin: An orally available platinum analog for the treatment of cancer. *Expert Rev. Anticancer Ther.* **6**, 973–982 (2006).

48. Eckardt, J. R. *et al.* Phase II study of picoplatin as second-line therapy for patients with small-cell lung cancer. *Clin. Oncol.* **27**, 2046–2051 (2009).

49. Armstrong, D. K. *et al.* Intraperitoneal Cisplatin and Paclitaxel in Ovarian Cancer. *N. Engl. J. Med.* **354**, 34–43 (2006).

50. Stordal, B., Pavlakis, N. & Davey, R. Oxaliplatin for the treatment of cisplatin-resistant cancer: A systematic review. *Cancer Treatment Reviews* **33**, 347–357 (2007).

51. French, C. A. Small-Molecule Targeting of BET Proteins in Cancer. *Advances in Cancer Research* **131**, 21–58 (2016).

52. Belkina, A. C. & Denis, G. V. BET domain co-regulators in obesity, inflammation and cancer. *Nature Reviews Cancer* **12**, 465–477 (2012).

53. Dawson, M. A., Kouzarides, T. & Huntly, B. J. P. Targeting Epigenetic Readers in Cancer. *N. Engl. J. Med.* **367**, 647–657 (2012).

54. Shi, J. & Vakoc, C. R. The mechanisms behind the therapeutic activity of BET bromodomain inhibition. *Mol. Cell* **54**, 728–736 (2014).

55. Shi, J. *et al.* Disrupting the Interaction of BRD4 with Diacetylated Twist Suppresses Tumorigenesis in Basal-like Breast Cancer. *Cancer Cell* **25**, 210–225 (2014).

56. Stathis, A. & Bertoni, F. BET proteins as targets for anticancer treatment. *Cancer Discov.* **8**, 24–36 (2018).

57. Liu, Z. *et al.* Drug Discovery Targeting Bromodomain-Containing Protein 4. *Journal of Medicinal Chemistry* **60**, 4533–4558 (2017).

58. Dong, J. *et al.* Transcriptional super-enhancers control cancer stemness and metastasis genes in squamous cell carcinoma. *Nat. Commun.* **12**, 1–14 (2021).

59. Qin, C. *et al.* Discovery of QCA570 as an Exceptionally Potent and Efficacious Proteolysis Targeting Chimera (PROTAC) Degrader of the Bromodomain and Extra-Terminal (BET) Proteins Capable of Inducing Complete and Durable Tumor Regression. *J. Med. Chem.* **61**,

6685–6704 (2018).

60. Sakamoto, K. M. *et al.* Protacs: Chimeric molecules that target proteins to the Skp1-Cullin-F box complex for ubiquitination and degradation. *Proc. Natl. Acad. Sci. U. S. A.* **98**, 8554–8559 (2001).

61. Liu, C. *et al.* The novel BET degrader, QCA570, is highly active against the growth of human NSCLC cells and synergizes with osimertinib in suppressing osimertinib-resistant EGFR-mutant NSCLC cells. *Am. J. Cancer Res.* **12**, 779 (2022).

62. Wang, Q. *et al.* Lethal activity of BRD4 PROTAC degrader QCA570 against bladder cancer cells. *Front. Chem.* **11**, 1121724 (2023).

63. Ganeson, K. *et al.* Microneedles for Efficient and Precise Drug Delivery in Cancer Therapy. *Pharmaceutics* **15**, 744 (2023).

64. McGuire, A. L. *et al.* Ethical Challenges Arising in the COVID-19 Pandemic: An Overview from the Association of Bioethics Program Directors (ABPD) Task Force. *Am. J. Bioeth.* **20**, 15–27 (2020).

65. Patt, D. *et al.* Impact of COVID-19 on Cancer Care: How the Pandemic Is Delaying Cancer Diagnosis and Treatment for American Seniors. *JCO Clin. Cancer Informatics* **4**, 1059–1071 (2020)

66. Riera, R. *et al.* Delays and Disruptions in Cancer Health Care Due to COVID-19 Pandemic: Systematic Review. *JCO Glob. Oncol.* **7**, 311–323 (2021)

67. Prausnitz, M. R. Engineering microneedle patches for vaccination and drug delivery to skin. *Annu. Rev. Chem. Biomol. Eng.* **8**, 177–200 (2017).

68. Nazary Abrbekoh, F. *et al.* Application of microneedle patches for drug delivery; doorstep to novel therapies. *Journal of Tissue Engineering* **13**, 20417314221085390 (2022).

69. Rajput, A. *et al.* A key role by polymers in microneedle technology: a new era. *Drug Dev. Ind. Pharm.* **47**, 1713–1732 (2021).

70. Yang, J., Liu, X., Fu, Y. & Song, Y. Recent advances of microneedles for biomedical applications: drug delivery and beyond. *Acta Pharm. Sin. B* **9**, 469–483 (2019).

71. Singh, V. & Kesharwani, P. Recent advances in microneedles-based drug delivery device in the diagnosis and treatment of cancer. *J. Control. Release* **338**, 394–409 (2021).

72. Bilal, M. *et al.* Microneedles in Smart Drug Delivery. *Adv. Wound Care* **10**, 204–219 (2021).

73. Jung, J. H. & Jin, S. G. Microneedle for transdermal drug delivery: current trends and fabrication. *Journal of Pharmaceutical Investigation* **51**, 503–517 (2021).

74. Aldawood, F. K., Andar, A. & Desai, S. A comprehensive review of microneedles: Types, materials, processes, characterizations and applications. *Polymers* **13**, 13162815 (2021).

75. Nandini, D. B. *et al.* Novel therapies in the management of oral cancer: An update. *Disease-a-Month* **66**, 101036 (2020).

76. D'Cruz, A. K., Vaish, R. & Dhar, H. Oral cancers: Current status. *Oral Oncol.* **87**, 64–69 (2018).

77. Ranganath, K. *et al*. Comparing outcomes of radial forearm free flaps and anterolateral thigh free flaps in oral cavity reconstruction: A systematic review and meta-analysis. *Oral Oncol.* **135**, 106214 (2022).

78. Deng, H., Sambrook, P. J. & Logan, R. M. The treatment of oral cancer: an overview for dental professionals. *Aust. Dent. J.* **56**, 244–252 (2011).

79. Li, X., *et al*. Microneedles: structure, classification, and application in oral cancer theranostics. *Drug Delivery and Translational Research* **13**, 2195–2212 (2023).

80. Adepu, S. & Ramakrishna, S. Controlled drug delivery systems: Current status and future

directions. *Molecules* **26**, 5905 (2021).

81. Lorscheider, M. *et al.* Challenges and Opportunities in the Delivery of Cancer Therapeutics: Update on Recent Progress. *Ther. Deliv.* **12**, 55–76 (2021).

82. Lu, Z. R. & Qiao, P. Drug Delivery in Cancer Therapy, Quo Vadis? *Mol. Pharm.* **15**, 3603–3616 (2018).

83. Ma, Y. *et al*. Drug coated microneedles for minimally-invasive treatment of oral carcinomas: development and in vitro evaluation. *Biomed. Microdevices* **17**, 1–14 (2015).

84. Liang, X. *et al.* RNAi-mediated downregulation of urokinase plasminogen activator receptor inhibits proliferation, adhesion, migration and invasion in oral cancer cells. *Oral Oncol.* **44**, 1172–1180 (2008).

85. Chan, K. K. W. *et al.* Interventions for the treatment of oral and oropharyngeal cancers: Targeted therapy and immunotherapy. *Cochrane Database of Systematic Reviews* **12** (2015).

86. Chen, D. *et al.* Targeting BMI1+ Cancer Stem Cells Overcomes Chemoresistance and Inhibits Metastases in Squamous Cell Carcinoma. *Cell Stem Cell* **20**, 621-634 (2017).

87. Ozsolak, F. & Milos, P. M. RNA sequencing: Advances, challenges and opportunities. *Nature Reviews Genetics* **12**, 87–98 (2011).

88. Liu, W. *et al.* Histone-methyltransferase KMT2D deficiency impairs the Fanconi anemia/BRCA pathway upon glycolytic inhibition in squamous cell carcinoma. *Nat. Commun.* **15**, 1–18 (2024).

89. Zhang, W. *et al.* Targeting KDM4A epigenetically activates tumor-cell-intrinsic immunity by inducing DNA replication stress. *Mol. Cell* **81**, 2148-2165 (2021).

90. Dang, C. V., Le, A. & Gao, P. MYC-induced cancer cell energy metabolism and therapeutic opportunities. *Clin. Cancer Res.* **15**, 6479–6483 (2009).

91. Kim, J. *et al*. An Extended Transcriptional Network for Pluripotency of Embryonic Stem Cells. *Cell* **132**, 1049–1061 (2008).

92. Dang, C. V. MYC, microRNAs and glutamine addiction in cancers. *Cell Cycle* **8**, 3243–3245 (2009).

93. S, M. *et al.* The landscape of somatic copy-number alteration across human cancers. *Nature* **463**, 899–905 (2010).

94. Field, J. K. *et al.* Elevated expression of the c-myc oncoprotein correlates with poor prognosis in head and neck squamous cell carcinoma. *Oncogene* **4**, 1463–1468 (1989).

95. Nakagawa, M. *et al*. Promotion of direct reprogramming by transformation-deficient Myc. *Proc. Natl. Acad. Sci. U. S. A.* **107**, 14152–14157 (2010).

96. Marconi, G. D. *et al.* C-Myc Expression in Oral Squamous Cell Carcinoma: Molecular Mechanisms in Cell Survival and Cancer Progression. *Pharmaceuticals* **15**, 890 (2022).

97. Delmore, J. E. *et al.* BET bromodomain inhibition as a therapeutic strategy to target c-Myc. *Cell* **146**, 904–917 (2011).

98. Dong, J. *et al.* Transcriptional super-enhancers control cancer stemness and metastasis genes in squamous cell carcinoma. *Nat. Commun.* **12**, 1–14 (2021).

99. Hayes, M. J. *et al*. Genetic changes of Wnt pathway genes are common events in metaplastic carcinomas of the breast. *Clin. Cancer Res.* **14**, 4038–4044 (2008).

100. He, T. C. *et al.* Identification of c-MYC as a target of the APC pathway. *Science* **281**, 1509–1512 (1998).

101. Cutright, D. E., Beasley, J. D. & Perez, B. Histologic comparison of polylactic and polyglycolic acid sutures. *Oral Surgery, Oral Med. Oral Pathol.* **32**, 165–173 (1971).

102. Brady, J. M. *et al*. Resorption rate, route of elimination, and ultrastructure of the implant

site of polylactic acid in the abdominal wall of the rat. *J. Biomed. Mater. Res.* **7**, 155–166 (1973).

103. Tojo, K., Aoyagi, H. & Kurita, T. Degradable Polymers for Sustained Drug Release. *Drug Deliv. Syst.* **31**, 84–111 (1980).

104. Yoon, S.-D., Kwon, Y.-S. & Lee, K.-S. Biodegradation and Biocompatibility of Poly L-lactic Acid Implantable Mesh. *Int. Neurourol. J.* **21**, S48 (2017).

105. Anderson, J. M. & Shive, M. S. Biodegradation and biocompatibility of PLA and PLGA microspheres. *Adv. Drug Deliv. Rev.* **28**, 5–24 (1997).

106. Ignatius, A. A. & Claes, L. E. In vitro biocompatibility of bioresorbable polymers: poly(L, DL-lactide) and poly(L-lactide-co-glycolide). *Biomaterials* **17**, 831–839 (1996).

107. Lagreca, E. *et al.* Recent advances in the formulation of PLGA microparticles for controlled drug delivery. *Prog. Biomater. 2020 94* **9**, 153–174 (2020).

108. Wischke, C. & Schwendeman, S. P. Principles of encapsulating hydrophobic drugs in PLA/PLGA microparticles. *International Journal of Pharmaceutics* **364**, 298–327 (2008).

109. Zhang, X. *et al.* Immunomodulatory microneedle patch for periodontal tissue regeneration. *Matter* **5**, 666–682 (2022).

110. Li, X. J. *et al.* Composite dissolvable microneedle patch for therapy of oral mucosal diseases. *Biomater. Adv.* **139**, 213001 (2022).

111. Sausville, E. A. & Burger, A. M. Contributions of human tumor xenografts to anticancer drug development. *Cancer Research* **66**, 3351–3354 (2006).

112. Fischer, C. A. *et al.* Co-overexpression of p21 and Ki-67 in head and neck squamous cell carcinoma relative to a significantly poor prognosis. *Head Neck* **33**, 267–273 (2011).

113. Yerushalmi, R. *et al*. Ki67 in breast cancer: prognostic and predictive potential. *Lancet*

Oncol. **11**, 174–183 (2010).

114. Yada, E. *et al*. Use of Patient-Derived Xenograft Mouse Models in Cancer Research and Treatment. *Futur. Sci. OA* **4**, 271 (2018).

115. Cho, S. Y. *et al.* An Integrative Approach to Precision Cancer Medicine Using Patient-Derived Xenografts. *Mol. Cells* **39**, 77–86 (2016).

116. Reya, T. *et al*. Stem cells, cancer, and cancer stem cells. *Nature* **414**, 105–111 (2001).

117. Wang, C. *et al.* CD276 expression enables squamous cell carcinoma stem cells to evade immune surveillance. *Cell Stem Cell* **28**, 1597-1613.e7 (2021).

118. de Visser, K. E. & Joyce, J. A. The evolving tumor microenvironment: From cancer initiation to metastatic outgrowth. *Cancer Cell* **41**, 374–403 (2023).

119. Xiao, Y. & Yu, D. Tumor microenvironment as a therapeutic target in cancer. *Pharmacology and Therapeutics* **221**, 107753 (2021).

120. Anand, P. *et al.* Cancer is a preventable disease that requires major lifestyle changes. *Pharmaceutical Research* **25**, 2097–2116 (2008).

121. Merlo, L. M. F., Pepper, J. W., Reid, B. J. & Maley, C. C. Cancer as an evolutionary and ecological process. *Nature Reviews Cancer* **6**, 924–935 (2006).

122. Junttila, M. R. & De Sauvage, F. J. Influence of tumour micro-environment heterogeneity on therapeutic response. *Nature* **501**, 346–354 (2013).

123. Quail, D. F. & Joyce, J. A. Microenvironmental regulation of tumor progression and metastasis. *Nature Medicine* **19**, 1423–1437 (2013).

124. Bejarano, L., Jordão, M. J. C. & Joyce, J. A. Therapeutic targeting of the tumor microenvironment. *Cancer Discovery* **11**, 933–959 (2021).

125. Ribas, A. & Wolchok, J. D. Cancer immunotherapy using checkpoint blockade. *Science*

359, 1350–1355 (2018).

126. Postow, M. A., Callahan, M. K. & Wolchok, J. D. Immune checkpoint blockade in cancer therapy. *Journal of Clinical Oncology* **33**, 1974–1982 (2015).

127. Pardoll, D. M. The blockade of immune checkpoints in cancer immunotherapy. *Nature Reviews Cancer* **12**, 252–264 (2012).

128. Gentles, A. J. *et al.* The prognostic landscape of genes and infiltrating immune cells across human cancers. *Nat. Med.* **21**, 938–945 (2015).

129. van der Leun, A. M., Thommen, D. S. & Schumacher, T. N. CD8+ T cell states in human cancer: insights from single-cell analysis. *Nature Reviews Cancer* **20**, 218–232 (2020).

130. Philip, M. & Schietinger, A. CD8+ T cell differentiation and dysfunction in cancer. *Nature Reviews Immunology* **22**, 209–223 (2022).

131. Borst, J. *et al*. CD4+ T cell help in cancer immunology and immunotherapy. *Nature Reviews Immunology* **18**, 635–647 (2018).

132. Hanahan, D. Rethinking the war on cancer. *The Lancet* **383**, 558–563 (2014).

133. Correia, A. L. & Bissell, M. J. The tumor microenvironment is a dominant force in multidrug resistance. *Drug Resist. Updat.* **15**, 39–49 (2012).

134. Jo, Y. *et al.* Chemoresistance of cancer cells: Requirements of tumor microenvironment-mimicking in vitro models in anti-cancer drug development. *Theranostics* **8**, 5259–5275 (2018).

135. Minchinton, A. I. & Tannock, I. F. Drug penetration in solid tumours. *Nature Reviews Cancer* **6**, 583–592 (2006).

136. Tannock, I. F. *et al*. Limited penetration of anticancer drugs through tumor tissue: A potential cause of resistance of solid tumors to chemotherapy. *Clin. Cancer Res.* **8**, 878–

884 (2002).

137. Ip, C. K. M. *et al.* Stemness and chemoresistance in epithelial ovarian carcinoma cells under shear stress. *Sci. Rep.* **6**, (2016).

138. Senthebane, D. A. *et al.* The role of tumor microenvironment in chemoresistance: 3D extracellular matrices as accomplices. *Int. J. Mol. Sci.* **19**, 2861 (2018).

139. Vaupel, P. & Mayer, A. Hypoxia in cancer: Significance and impact on clinical outcome. *Cancer and Metastasis Reviews* **26**, 225–239 (2007).

140. Zhao, W. *et al.* Hypoxia-induced resistance to cisplatin-mediated apoptosis in osteosarcoma cells is reversed by gambogic acid independently of HIF-1α. *Mol. Cell. Biochem.* **420**, 1–8 (2016).

141. Jalota, A. *et al.* A drug combination targeting hypoxia induced chemoresistance and stemness in glioma cells. *Oncotarget* **9**, 18351–18366 (2018).

142. Kim, M. C. *et al.* Hypoxia promotes acquisition of aggressive phenotypes in human malignant mesothelioma. *BMC Cancer* **18**, 1–11 (2018).

143. Soleymani Abyaneh, H. *et al.* Hypoxia Induces the Acquisition of Cancer Stem-like Phenotype Via Upregulation and Activation of Signal Transducer and Activator of Transcription-3 (STAT3) in MDA-MB-231, a Triple Negative Breast Cancer Cell Line. *Cancer Microenviron.* **11**, 141–152 (2018).

144. Raghunand, N. & Gillies, R. J. pH and drug resistance in tumors. *Drug Resist. Updat.* **3**, 39–47 (2000).

145. Gerweck, L. E., Vijayappa, S. & Kozin, S. Tumor pH controls the in vivo efficacy of weak acid and base chemotherapeutics. *Mol. Cancer Ther.* **5**, 1275–1279 (2006).

146. Tao, L. *et al.* Cancer-associated fibroblasts treated with cisplatin facilitates chemoresistance

of lung adenocarcinoma through IL-11/IL-11R/STAT3 signaling pathway. *Sci. Rep.* **6**, (2016).

147. Zhang, H. *et al.* Cancer-associated fibroblasts mediated chemoresistance by a FOXO1/TGFβ1 signaling loop in esophageal squamous cell carcinoma. *Mol. Carcinog.* **56**, 1150–1163 (2017).

148. Qiao, Y. *et al.* IL6 derived from cancer-associated fibroblasts promotes chemoresistance via CXCR7 in esophageal squamous cell carcinoma. *Oncogene* **37**, 873–883 (2018).

149. Wang, L. *et al.* Cancer-associated fibroblasts contribute to cisplatin resistance by modulating ANXA3 in lung cancer cells. *Cancer Sci.* **110**, 1609–1620 (2019).

150. Long, X. *et al.* Cancer-associated fibroblasts promote cisplatin resistance in bladder cancer cells by increasing IGF-1/ERβ/Bcl-2 signalling. *Cell Death Dis.* **10**, 375 (2019).

151. Zhai, J. *et al.* Cancer-associated fibroblasts-derived IL-8 mediates resistance to cisplatin in human gastric cancer. *Cancer Lett.* **454**, 37–43 (2019).

152. Salvagno, C. *et al.* Therapeutic targeting of macrophages enhances chemotherapy efficacy by unleashing type I interferon response. *Nat. Cell Biol.* **21**, 511–521 (2019).

153. Pass, H. I. *et al.* Inhibition of the colony-stimulating-factor-1 receptor affects the resistance of lung cancer cells to cisplatin. *Oncotarget* **7**, 56408–56421 (2016).

154. Hanahan, D. & Weinberg, R. A. Hallmarks of cancer: The next generation. *Cell* **144**, 646–674 (2011).

155. Hanahan, D. Hallmarks of Cancer: New Dimensions. *Cancer Discovery* **12**, 31–46 (2022).

156. Warburg, O., Wind, F. & Negelein, E. The metabolism of tumors in the body. *J. Gen. Physiol.* **8**, 519–530 (1927).

157. Heiden, M. G. V., Cantley, L. C. & Thompson, C. B. Understanding the warburg effect:

The metabolic requirements of cell proliferation. *Science* **324**, 1029–1033 (2009).

158. Faubert, B. et al. Lactate Metabolism in Human Lung Cancer. *Cell* **171**, 358-371 (2017).

159. Dhup, S. *et al*. Multiple Biological Activities of Lactic Acid in Cancer: Influences on Tumor Growth, Angiogenesis and Metastasis. *Curr. Pharm. Des.* **18**, 1319–1330 (2012).

160. San-Millán, I. & Brooks, G. A. Reexamining cancer metabolism: Lactate production for carcinogenesis could be the purpose and explanation of the Warburg Effect. *Carcinogenesis* **38**, 119–133 (2017).

161. Lyssiotis, C. A. & Kimmelman, A. C. Metabolic Interactions in the Tumor Microenvironment. *Trends in Cell Biology* **27**, 863–875 (2017).

162. Elia, I. *et al.* Tumor cells dictate anti-tumor immune responses by altering pyruvate utilization and succinate signaling in CD8+ T cells. *Cell Metab.* **34**, 1137-1150 (2022).

163. Zou, Y. *et al.* The Single-Cell Landscape of Intratumoral Heterogeneity and The Immunosuppressive Microenvironment in Liver and Brain Metastases of Breast Cancer. *Adv. Sci.* **10**, 2203699 (2023).

164. Certo, M. *et al*. Lactate modulation of immune responses in inflammatory versus tumour microenvironments. *Nature Reviews Immunology* **21**, 151–161 (2021).

165. Feng, Y. *et al.* Lactate dehydrogenase A: A key player in carcinogenesis and potential target in cancer therapy. *Cancer Med.* **7**, 6124–6136 (2018).

166. Shi, M. *et al.* A novel KLF4/LDHA signaling pathway regulates aerobic glycolysis in and progression of pancreatic cancer. *Clin. Cancer Res.* **20**, 4370–4380 (2014).

167. Huang, X. *et al.* High expressions of LDHA and AMPK as prognostic biomarkers for breast cancer. *Breast* **30**, 39–46 (2016).

168. Oshima, N. *et al.* Dynamic Imaging of LDH Inhibition in Tumors Reveals Rapid In Vivo

Metabolic Rewiring and Vulnerability to Combination Therapy. *Cell Rep.* **30**, 1798-1810 (2020).

169. Tian, Z. *et al.* Catalytically Selective Chemotherapy from Tumor-Metabolic Generated Lactic Acid. *Small* **15**, 1903746 (2019).

170. Zhou, X. *et al.* Dual-Modal Therapeutic Role of the Lactate Oxidase-Embedded Hierarchical Porous Zeolitic Imidazolate Framework as a Nanocatalyst for Effective Tumor Suppression. *ACS Appl. Mater. Interfaces* **12**, 32278–32288 (2020).

171. Tang, J. *et al.* Openwork@Dendritic Mesoporous Silica Nanoparticles for Lactate Depletion and Tumor Microenvironment Regulation. *Angew. Chemie* **132**, 22238–22246 (2020).

172. Los, M., Dröge, W., Stricker, K., Baeuerle, P. A. & Schulze-Osthoff, K. Hydrogen peroxide as a potent activator of T lymphocyte functions. *Eur. J. Immunol.* **25**, 159–165 (1995).

173. Reth, M. Hydrogen peroxide as second messenger in lymphocyte activation. *Nature Immunology* **3**, 1129–1134 (2002).

174. Vermonden, T., Censi, R. & Hennink, W. E. Hydrogels for protein delivery. *Chemical Reviews* **112**, 2853–2888 (2012).

175. Yu, M. *et al*. Nanotechnology for protein delivery: Overview and perspectives. *J. Control. Release* **240**, 24–37 (2016).

176. Bizeau, J. & Mertz, D. Design and applications of protein delivery systems in nanomedicine and tissue engineering. *Advances in Colloid and Interface Science* **287**, 102334 (2021).

177. Yu, L. *et al.* Microfluidic formation of core-shell alginate microparticles for protein encapsulation and controlled release. *J. Colloid Interface Sci.* **539**, 497–503 (2019).

178. Cho, E. *et al.* Comparison of exosomes and ferritin protein nanocages for the delivery of membrane protein therapeutics. *J. Control. Release* **279**, 326–335 (2018).

179. Yang, X. *et al.* Nanoscale ATP-Responsive Zeolitic Imidazole Framework-90 as a General Platform for Cytosolic Protein Delivery and Genome Editing. *J. Am. Chem. Soc.* **141**, 3782–3786 (2019).

180. Song, M. *et al.* Carboxymethyl-β-cyclodextrin grafted chitosan nanoparticles as oral delivery carrier of protein drugs. *React. Funct. Polym.* **117**, 10–15 (2017).

181. Koshy, S. T. *et al*. Injectable nanocomposite cryogels for versatile protein drug delivery. *Acta Biomater.* **65**, 36–43 (2018).

182. Wei, W. *et al.* Synthesis and characterization of a multi-sensitive polysaccharide hydrogel for drug delivery. *Carbohydr. Polym.* **177**, 275–283 (2017).

183. Mohammadi, M. *et al.* Fabrication of hybrid scaffold based on hydroxyapatite-biodegradable nanofibers incorporated with liposomal formulation of BMP-2 peptide for bone tissue engineering. *Nanomedicine Nanotechnology, Biol. Med.* **14**, 1987–1997 (2018).

184. Zhao, Y. N. *et al.* A Drug Carrier for Sustained Zero-Order Release of Peptide Therapeutics. *Sci. Rep.* **7**, 5524 (2017).

185. Seong, K. Y. *et al.* A self-adherent, bullet-shaped microneedle patch for controlled transdermal delivery of insulin. *J. Control. Release* **265**, 48–56 (2017).

186. Yao, Q. *et al*. Mesoporous silicate nanoparticles/3D nanofibrous scaffold-mediated dual-drug delivery for bone tissue engineering. *J. Control. Release* **279**, 69–78 (2018).

187. Yan, M. *et al.* A novel intracellular protein delivery platform based on single-protein nanocapsules. *Nat. Nanotechnol.* **5**, 48–53 (2010).

188. Xu, D. *et al.* Efficient Delivery of Nerve Growth Factors to the Central Nervous System for Neural Regeneration. *Adv. Mater.* **31**, 1900727 (2019).

189. Qin, M. *et al.* An Antioxidant Enzyme Therapeutic for COVID-19. *Adv. Mater.* **32**, 2004901

(2020).

190. Cao, Z. *et al.* Lactate oxidase nanocapsules boost T cell immunity and efficacy of cancer immunotherapy. *Sci. Transl. Med.* **15**, (2023).

191. Wen, J. *et al.* Sustained delivery and molecular targeting of a therapeutic monoclonal antibody to metastases in the central nervous system of mice. *Nat. Biomed. Eng.* **3**, 706–716 (2019).

192. Yue, H. *et al*. Ethylene glycol: properties, synthesis, and applications. *Chem. Soc. Rev.* **41**, 4218–4244 (2012).

193. Digman, M. A. & Gratton, E. Lessons in fluctuation correlation spectroscopy. *Annu. Rev. Phys. Chem.* **62**, 645–668 (2011).

194. Dzakpasu, R. & Axelrod, D. Dynamic light scattering microscopy. A novel optical technique to image submicroscopic motions. I: Theory. *Biophys. J.* **87**, 1279–1287 (2004).

195. Bhattacharjee, S. DLS and zeta potential – What they are and what they are not? *J. Control. Release* **235**, 337–351 (2016).

196. Yang, L. *et al.* Biomimetic enzyme nanocomplexes and their use as antidotes and preventive measures for alcohol intoxication. *Nat. Nanotechnol.* **8**, 187–192 (2013).

197. Li, J. *et al.* Development of Novel Therapeutics Targeting the Blood–Brain Barrier: From Barrier to Carrier. *Adv. Sci.* **8**, 2101090 (2021).

198. Xu, D. *et al.* Efficient Delivery of Nerve Growth Factors to the Central Nervous System for Neural Regeneration. *Adv. Mater.* **31**, (2019).

199. Bütün, V., Armes, S. P. & Billingham, N. C. Synthesis and aqueous solution properties of near-monodisperse tertiary amine methacrylate homopolymers and diblock copolymers. *Polymer (Guildf).* **42**, 5993–6008 (2001).

200. Griffiths, J. R. Are cancer cells acidic? *British Journal of Cancer* **64**, 425–427 (1991).

201. Vaupel, P., Kallinowski, F. & Okunieff, P. Blood Flow, Oxygen and Nutrient Supply, and Metabolic Microenvironment of Human Tumors: A Review. *Cancer Res.* **49**, 6449–6465 (1989).

202. Jiménez-Labaig, P. *et al.* Intratumoral therapies in head and neck squamous cell carcinoma: A systematic review and future perspectives. *Cancer Treatment Reviews* **127**, 102746 (2024).

203. Patgiri, A. *et al.* An engineered enzyme that targets circulating lactate to alleviate intracellular NADH:NAD+ imbalance. *Nat. Biotechnology* **38**, 309–313 (2020).

204. Chang, D. K. *et al.* Human anti-CAIX antibodies mediate immune cell inhibition of renal cell carcinoma in vitro and in a humanized mouse model in vivo. *Mol. Cancer* **14**, (2015).

205. Fisher, T. S. *et al.* Targeting of 4-1BB by monoclonal antibody PF-05082566 enhances T-cell function and promotes anti-tumor activity. *Cancer Immunol. Immunother.* **61**, 1721–1733 (2012).

206. Maurice Morillon, Y., Sabzevari, A., Schlom, J. & Greiner, J. W. The development of next-generation PBMC humanized mice for preclinical investigation of cancer immunotherapeutic agents. *Anticancer Research* **40**, 5329–5341 (2020).

207. Cunningham, C. C. *et al.* Clinical and local biological effects of an intratumoral injection of mda-7 (IL24; INGN 241) in patients with advanced carcinoma: A phase I study. *Mol. Ther.* **11**, 149–159 (2005).

208. Adams, P. D. *et al.* BET Inhibitors Potentiate Activation of p53 and Killing of AML By MDM2 Inhibitors — a Candidate Combination Therapy. *Blood* **132**, 3912–3912 (2018).

209. Deng, M. *et al.* Aggressive B-cell lymphoma with MYC/TP53 dual alterations displays

distinct clinicopathobiological features and response to novel targeted agents. *Mol. Cancer Res.* **19**, 249–260 (2021).

210. Adeegbe, D. O. *et al.* BET bromodomain inhibition cooperates with PD-1 blockade to facilitate antitumor response in kras-mutant non-small cell lung cancer. *Cancer Immunol. Res.* **6**, 1234–1245 (2018).